



**UNIVERSITÀ DEGLI STUDI DI MESSINA**

**Dipartimento di Scienze Matematiche e Informatiche,**

**Scienze Fisiche e Scienze della Terra**

**Dottorato di Ricerca in Fisica**

**XXXI Ciclo (FIS/01)**

---

**Laser ablation synthesis of noble metal  
and metal oxide nanoparticles for  
sensing and drug delivery applications**

Candidate:

**Marco SANTORO**

Supervisor:

**Ch.mo Prof. Fortunato NERI**

Coordinator:

**Ch.mo Prof. Lorenzo Torrisi**

---

2015-2018



# Contents

<b>Abstract</b>	<b>i</b>
<b>1 Introduction to Nanoparticles</b>	<b>1</b>
1.1 Nanoparticles properties . . . . .	2
1.2 Nanoparticles synthesis approaches . . . . .	5
<b>2 Laser-generated Nanoparticles</b>	<b>8</b>
2.1 Pulsed Laser Deposition . . . . .	13
2.1.1 Plasma expansions . . . . .	15
2.2 Pulsed Laser Ablation in Liquid . . . . .	18
2.2.1 Cavitation bubble formation . . . . .	20
2.3 Laser post-processing of colloids . . . . .	22
2.3.1 Laser Melting in Liquid . . . . .	24
2.3.2 Laser Fragmentation in Liquid . . . . .	24
<b>3 Cavitation Bubbles on a re-irradiated target</b>	<b>27</b>
3.1 Shadowgraphy setup for cavitation bubble imaging . . . . .	28
3.2 Cavitation bubble by changing the number of laser pulses . . . . .	31
3.3 Correlation between cavitation bubble and ablated mass . . . . .	35
3.4 Nanostructures synthesis and characterization . . . . .	38
<b>4 Noble metal nanoparticles for SERS applications</b>	<b>44</b>
4.1 Surface Enhanced Raman Spectroscopy substrates for therapeutic drug monitoring . . . . .	44

4.2	Ag and Au nanoparticles: synthesis and characterization . . . . .	47
4.3	SERS sensing of perampanel with nanostructured arrays of Au particles . . . . .	54
4.3.1	Ag-Au alloy nanoclusters: synthesis and characterization . . . . .	62
4.4	Ultraviolet plasmonic response of Rhodium nanoparticles . . . . .	64
4.4.1	Rhodium oxide nanoparticles: synthesis and characterization . . . . .	66
<b>5</b>	<b>Plasmonic Noble Metal Nanoparticles for drug delivery</b>	<b>72</b>
5.1	Silver nanoparticles embedded in a PEG-PLA matrix . . . . .	74
5.1.1	Ag NPs synthesis . . . . .	74
5.1.2	PEG-PLA copolymer synthesis . . . . .	77
5.1.3	PEG-PLA@Ag-PVA composite synthesis . . . . .	79
5.1.4	PEG-PLA@Ag-PVA/SLB composite preparation . . . . .	80
5.1.5	Light-activated drug release . . . . .	81
5.1.6	In vitro biocompatibility . . . . .	84
5.2	PEG-PLGA electrospun nanofibrous membranes loaded with silibinin and $Ag/Au@Fe_2O_3$ nanoparticles . . . . .	86
5.2.1	$Fe_2O_3$ antimicrobial activity . . . . .	90
5.2.2	Silibinin release in response to light source and magnetic field . . . . .	93
<b>6</b>	<b>Rhodium oxide nanostructures for hydrogen gas sensors</b>	<b>98</b>
6.0.1	Rhodium-Rhodium oxide: synthesis and characterization . . . . .	101
6.0.2	Electrical and hydrogen sensing properties . . . . .	103
	<b>Appendix</b>	<b>115</b>
	<b>Bibliography</b>	<b>116</b>
	<b>Acknowledgement</b>	<b>140</b>
	<b>Curriculum Vitae</b>	<b>141</b>

# Abstract

After more than 20 years of basic nanoscience research and more than fifteen years of focused development, the entire society can benefit of both expected and unexpected applications of nanotechnology. In particular, the use of nanoparticles are considerably improving many technologies and industrial sectors: information technology, homeland security, medicine, transportation, energy, environmental science, and many others. The properties of many conventional materials change when made up of nanoparticles. This is typical, because nanoparticles have a greater surface area per weight than larger particles which causes them to be more reactive to other molecules. Many benefits of nanoparticles depend on the possibility to tailor the surface/volume ratio which allows to achieve specific properties. In fact, materials can effectively be made stronger, lighter, more durable, more reactive, or better electrical conductors. Many everyday commercial products currently on the market rely on nanoscale materials and processes, such as:

- The use of polymeric micelle nanoparticles to deliver drugs to tumors;
- The use of polymer coated iron oxide nanoparticles to break up clusters of bacteria, possibly allowing more effective treatment of chronic bacterial infections;
- Metal oxide nanoparticles act as an antioxidant to remove oxygen free radicals that are present in a patient's bloodstream following a traumatic injury. The nanoparticles absorb the oxygen free radicals and then release the oxygen in a less dangerous state, freeing up the nanoparticle to absorb more free radicals;

- Iron nanoparticles are being used to clean up carbon tetrachloride pollution in ground water;
- Noble metal nanoparticles such as silver (Ag) and gold (Au) have unique plasmonic properties that give rise to surface enhanced Raman scattering (SERS). SERS enhancement depends on the chemical composition and structure of these nanoparticles. Research activities are focused in optimizing the design of Ag/Au hybrid nanoparticles for SERS-based detection methods. Recent years have witnessed great interest in the development of SERS nanoprobcs for Raman imaging. Rationally designed SERS nanoprobcs have greatly enhanced Raman signals by several orders of magnitude, thus showing great potential for biosensing applications;
- Nanoparticles can be incorporated into solar panels to convert sunlight to electricity more efficiently, promising inexpensive solar power in the future. Nanostructured solar cells could be cheaper to manufacture and easier to install, since they can use print-like manufacturing processes and can be made in flexible rolls rather than discrete panels. Newer research suggests that future solar converters might even be "paintable".

To open up new opportunities for producing high-performance nanomaterials, useful for different technological applications, the outcomes of this PhD thesis are:

1. defining strategies to force pulsed laser ablation method (mainly in a liquid environment) to grow metal based nanoparticles with fine control on compositional and morphological properties, appropriate for a specific surface functionalization;
2. providing a systematic study of the mechanisms involved during the ablation process such as the cavitation bubbles formation and their effects on nanoparticles properties; in particular it was evaluated the impact on the nanoparticles size of cavitation bubbles shape and of dynamics changes due to the re-irradiation of the target;
3. demonstrating the transversal empowering of the synthesized material through its application for:

- SERS activity of Au nanoparticles produced by picosecond ablation to obtain the first SERS spectrum of the new generation antiepileptic drug perampanel, whose clinical interest is relevant. A controlled synthesis of Au nanoparticles by both nanosecond and picosecond pulsed laser ablation in water (PLAL), with no stabilizing agent, was carried out obtaining a narrow size distribution and a remarkable long-term stability. Then, Au nanoparticles efficiency was tested by collecting the first FT-Raman and SERS spectra of perampanel;
- a controlled drug release at a specific target site in response to external stimuli (laser light sources and magnetic field). Specifically, the synthesis and characterization of a new type of external- activated drug delivery carrier made of silver, gold and iron oxide nanoparticles embedded in PEG-PLA or PEG-PLGA polymeric nanoplatfoms were carried out. These systems allow to encapsulate (89%) and to release with a high efficiency (about 10%) of silibinin, working as drug delivery triggered by external stimuli, applicable to the biomedical field;
- a new generation of a resistive hydrogen sensor based on rhodium oxide nanoparticles which shows high response to low concentration of the target gas in air and at low operating temperature. It has been developed a simple approach providing a general way to prepare new hydrogen sensing materials based on colloidal rhodium oxides nanoparticles while eliminating the nanofabrication obstacles of previous ones. We also demonstrated, for the first time, the sensing properties of these nanostructures toward low concentration of hydrogen in air, fabricating a simple and promising conductometric platform for novel  $H_2$  sensors that can be applied for environmental monitoring, biomedical as well as industrial safety applications.

The thesis is organized in five chapters. Chapter 1 is a short overview on the basic nanoparticles properties and on the synthesis approach. Chapter 2 is focussed on the Pulsed Laser Ablation synthesis process carried out in a liquid environment. In this chapter a brief overview of some phenomena involved during the ablation process is reported. In Chapter 3 are described some results

on cavitation bubbles and the influence of the re-irradiation of the target on bubble shape and dynamics. Moreover, the impact on nanoparticles properties has been evaluated. These results were acquired during my internship in the laboratory of Technical Chemistry in Essen. Chapter 4 deals on the synthesis and characterization of plasmonic nanoparticles: Silver, Gold, and Rhodium. In this chapter is reported initially a study on ablation parameters tuning, in order to optimize NPs size distribution in view of SERS sensing applications. In chapter 5 is reported about the synthesis and characterization of plasmonic noble metal nanoparticles for drug delivery. Finally, chapter 6 deals on the synthesis of Rhodium-Rhodium oxide nanoparticles for hydrogen gas sensor devices.



# Chapter 1

## Introduction to Nanoparticles

Nanomaterial (NMs) science and technology became an important part of technological advancement in modern society. It represents an active area of research and a techno-economic sector with full expansion in many application domains [1, 2]. It is a multidisciplinary field that involves physics, chemistry, biology, and engineering and is running all over the world [3]. Engineered nanomaterials applications can be found in everyday life such as cerium oxide contained in diesel fuel to reduce emissions, silver nanoparticles that kill bacteria making clothing odor-resistant, titanium dioxide contained in certain sunscreens and fullerenes in face cream [4, 5]. NMs have gained prominence in technological advancements due to their tunable physico-chemical characteristics such as a higher melting point, wettability, enhanced electrical and thermal conductivity, and interesting optical properties respect to their bulk counterparts. Research on nanotechnology involves different application areas ranging from energy and electronics to the environment, health and medical sector [6, 7, 8, 9].

In the huge field of nanomaterial science, a still evolving topic is nanoparticle-based materials, which involves fabricating, evaluating, and processing objects that are up to three orders of magnitude smaller than micron sized particles. This kind of materials exhibits exciting properties, and the corresponding dimensions bridges the gap between atoms/molecules and bulk materials. It is possible to define the term "nanoparticle" as any microscopic object with every dimensions smaller than 100 nanometers (nm) in size. It behaves as a whole

unit in terms of its structural and functional properties and its interaction with other species and with the environment [10]. Nanoparticles are not just an artificial creation since they are around us in our ordinary life, because they are naturally present in the atmosphere, in the sea and in the space. They have a great importance for the formation of clouds, rains and other natural phenomena governing earth life [11]. However artificial nanoparticles are synthesized with a large variety of methods for different technological applications with the aim of improve environment and quality of life.

## 1.1 Nanoparticles properties

Nanoparticles are an interesting and unique materials category thanks to their size that is smaller than the critical dimensions that characterize many physical phenomena, such as thermal diffusion length, light wavelength, and electron mean free path. When a dimension is less than these critical lengths (few nanometers), new physics or chemistry is likely to occur, that are not detectable in the bulk counterpart [12]. This behaviour is explained considering that a large percentage of atoms in a NP has an uncompensated bond structure because of their localization on the surface. Fig. 1.1 shows the fraction of atoms on surface and on bulk versus particles diameter. It is evident that the fraction of surface atoms decreases upon increasing nanoparticles size. In particular, for nanoparticles smaller than 5 nm more than 50% of atoms belong to the surface. In fact, if we consider a cube of iron of  $1 \text{ cm}^3$ , the percentage of surface atoms would be 0.00001%, instead in a cube of iron of  $1 \text{ nm}^3$ , every atom would be a surface atom. Such a dramatic increase in the ratio of surface atoms leads to great changes in the physical and chemical properties of the materials [13]. If we consider the total energy of a particles it can always be written:  $E_{tot} = E_{bulk} + E_{surf}$ . For macroscopic particles the surface term is negligible respect to the bulk one, instead, if we consider nanoparticles of few nanometers, the surface energy term becomes dominant. This factor have strong impact in all the phenomena that occur on nanoparticles surface such as:

- Electrostatic forces play a major role in nanoparticle formation and also have an important effect on nanomaterial properties [14]. Nanomaterials,

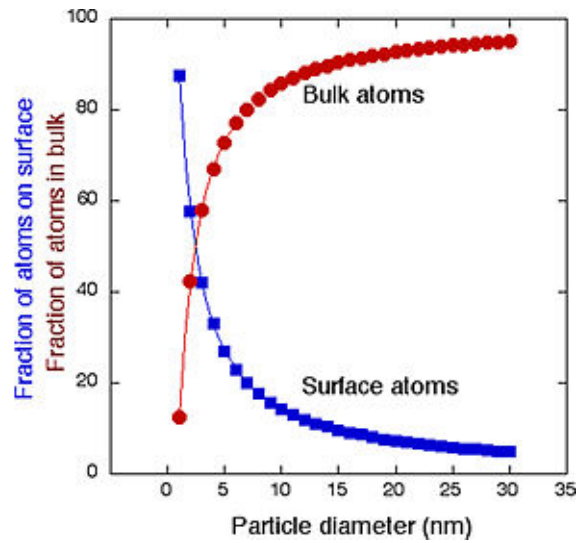


Figure 1.1: Fraction of atoms on surface and bulk vs. nanoparticle diameter. Image retrieved from: <https://chem.libretexts.org/>

conduct electrical current differently compared with bulk conductors. The limited size in the direction perpendicular to the axis and the organized structure result in weak phonon-charge carrier interaction and ballistic transport. In the ballistic regime of electrical conduction, the resistance depends on the number of conductance channels used and not on the length of the conductor, following the Landauer's law [15].

- bond length contraction occurring when the surface to volume atom ratio increases. The bond contraction of nanomaterials is between 4% and 30% respect to their bulk counterpart. For this reasons nanostructured materials have an higher elastic module, that increase their melting temperature and rigidity [16];
- the magnetic behaviour of nanoparticles having a smaller size respect to Weiss domain allows them to follow better external magnetic field. In fact their magnetic susceptibility is higher respect to bulk materials [17];
- the band structure of bulk materials comes back to the discrete distribution of electronic levels typical of atoms and molecules. In Fig. 1.2 are shown the differences between the bandstructure of metals and insulators

nanostructured materials respect to the bulk one. Quantum effects starts

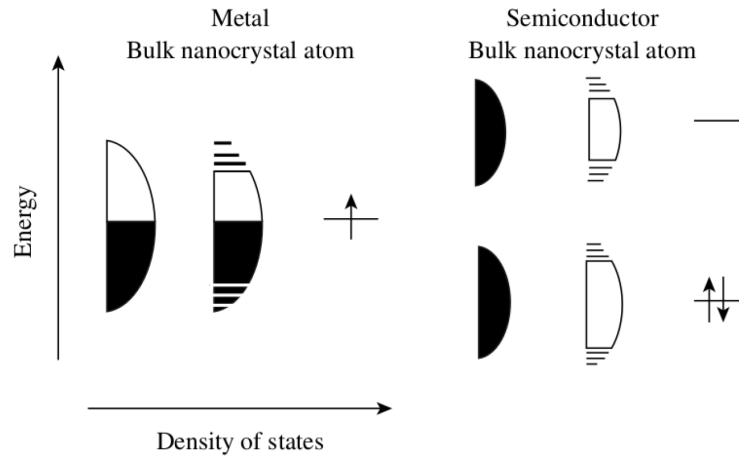


Figure 1.2: Density of states differences between bulk and nanostructured metals (left) and insulators (right).

at the edges of electronic bands. This behavior makes some differences between metals and insulator nanoparticles because the energetic exchange phenomena in a metal involves mainly electrons with energy close to the Fermi level instead, in insulator materials, the energetic exchange is mainly due to band edges and it occurs at sizes relatively higher.

- Optical properties are governed by quantum confinement effects. In particular, the lower dimensionality results in a larger difference between discrete energy levels, resulting in higher excitation energy [18]. The interaction with photons can be interpreted by introducing a quasi-particle known as the surface plasmon (SP) that represents electrons oscillations in the confined space [19]. The Surface Plasmon Resonance (SPR) for different nanomaterials depends on their size, their shape and the material composition. Nanoparticles and their coupling is a powerful way to confine intense electromagnetic field [20, 21], as will be described in more detail in chapter 4. For example, noble metal nanoparticles, thanks to this behaviour, are widely used for as imaging and detections of molecules, drug delivery and photo-thermal therapy as well as for environmental sensing and catalysis.

Nanoparticles ability to catalyze reactions by interacting with substrates and reagents derives from the large percentage of coordinatively unsaturated atoms located at the surface, edges and corners of the NPs compared to the total number of atoms. Particularly those atoms located at steps, corners and edges of NPs exhibit the highest catalytic activity due to their low coordination number and their high tendency to increase this number by coordinating with substrates and other species in the surroundings [22].

NPs can be prepared by different procedures, their main drawback is their tendency to agglomerate when they increase in size. A way to avoid this problem is by adsorbing some stabilizers on NPs surface. In addition to this role, supports can also play an additional role in the catalysis providing acidity/basicity or by tuning the electronic density of the NPs. Then, the synthesis method is of fundamental importance for the NPs generation to optimize both their stability and properties.

## 1.2 Nanoparticles synthesis approaches

Synthesis of nanomaterials is an important step in the development of particles that shows quantum behaviour. Materials scientists and engineers improved significantly the synthesis methods of nanomaterial solids [23]. Generally it is possible to distinguish two different synthesis approaches: the *bottom-up* assembly and the *top-down* fabrication [24] that are schematically shown in Fig. 1.3.

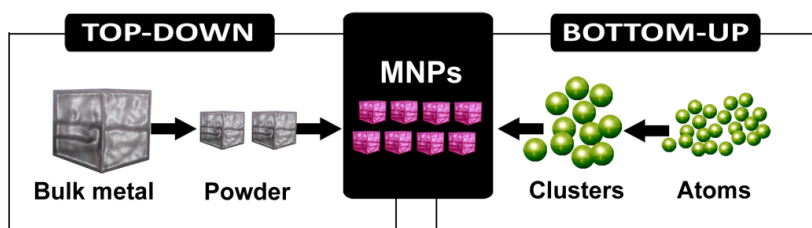


Figure 1.3: Scheme of two typical approaches used for metal nanoparticles synthesis. Image retrieved from: <http://nanotechnologyjd.weebly.com/>

The *bottom up* process builds-up a material from the bottom: atom-by-atom, molecule-by-molecule allows to control the chemistry of nanoparticles, improving their uniformity and reducing structural defects. It is also possible to have a strong control on NPs dimensions, while the drawback of these techniques is the unavoidable presence of impurities on synthesized nanoparticles due to the use of chemicals. This, in turn, makes necessary post synthesis purification processes which can reduce final product quality. Moreover, the use of chemicals and purification steps increases synthesis costs making these processes not convenient for industrial applications. Bottom-up approach includes, but are not limited to, colloidal methods, coprecipitation, electrochemical deposition, direct precipitation, sol-gel processing, microemulsions method, reverse micelle synthesis, hydrothermal synthesis, template methods and polyol method [25].

In the *top down* approach bulk materials are etched for producing NPs or nanostructures. This approach contains mostly physical synthesis technique that are of major interest in this thesis. The biggest problem with this approach is the imperfection of surface structure. Such imperfections can have a significant impact on physical properties and surface chemistry of nanostructures and nanomaterials, since the surface over volume ratio in nanostructures and nanomaterials is very large. See for example the synthesis of nanocrystalline  $\alpha - \text{Al}_2\text{O}_3$  (surface area up to  $100 \text{ m}^2/\text{g}$ ) by high-energy ball milling or the synthesis of nanosize yttrium zirconia ( $\text{Y} - \text{ZrO}_2$ ) by selective leaching of bulky yttrium-doped  $\text{BaZrO}_3$ . The different synthesis and processing approaches often result in appreciable differences in chemical composition, crystallinity, and microstructure of the material due to kinetic reasons. Consequently, the nanomaterial exhibits different physical properties[26].

All the existing top-down production techniques work following the same sequence of processes: *vaporization*, *nucleation*, *growth* and *coalescence*. Starting from a solid, it is possible to vaporize it exploiting a particular physical phenomenon [27]. Depending on the physical phenomenon exploited it is possible to distinguish several NP sources: the evaporation process exploits the heating of a solid that can be accomplished, for example, by thermal heating, electron bombardment and laser ablation where particles ejection from the target follows the laser pulse sequence. This technique enables even the evaporation of refrac-

tory metals and ceramics, thanks to the high energy density obtained at the laser spot. The resulting plasma expansion depends on many parameters, such as laser pulse fluence, target material, laser frequency so on [28]. Recently, it has been demonstrated that even the irradiated spot area, and thus the ablated mass per pulse, have to be kept into account because even the resulting plasma dynamics is strongly influenced by the plume mass [29, 30]. After the evaporation process, electrons recombine with ions and condensation occur in the vapor. The condensation proceeds in two stages: nucleation of critical clusters and nuclei growth [31].

The focus of this thesis will be on nanoparticles synthesis by means of an high-power laser pulse. Laser-generated nanoparticles are promising in several fields such as sensing, optics, biomedicine or catalysis due to the possibility of receiving nanoparticles without any ligands. In particular laser ablation in liquids allows to obtain a colloidal solution of nanoparticles in a variety of liquids, starting from numerous target materials.

## Chapter 2

# Laser-generated

# Nanoparticles

Laser ablation (LA) of solids is universally considered to be a physico-chemical combined top-down (macroscopic solid targets) and bottom-up (initially formed plasma, atoms, and clusters) method with initial processes governed by laser plasma and cavitation physics [32, 33].

It has attracted much interest ever since the invention of ruby laser and, because of the high power density near the focus of a pulsed laser ( $> 10^9 \text{ W/cm}^2$ ), it can be applied to nearly all classes of materials [34]. In recent years the interest in laser ablation is growing due to its versatility, low cost and convenience of execution. Moreover, it is a physico-chemical synthesis method that produces ligand-free, high purity NPs with superior conjugation efficiency, grafting density, electroaffinity toward charged biomolecules [35]. Typical laser beam parameter requirements for LA are wavelengths from ultraviolet to near-infrared, a typical laser energy density (fluence) between 0.1 and 100  $\text{J/cm}^2$ , and pulse durations from femtosecond (fs) up to microsecond ( $\mu\text{s}$ ), and millisecond (ms) regimes, extending to continuous-wave (CW) lasers [36]. Laser ablation can occur in vacuum, gas, and liquid, providing that the gas or liquid does not strongly attenuate laser energy and the light intensity impinging on the solid surface is still enough to perturb the material away from equilibrium state. The major applications of laser ablation in vacuum or gas is the pulsed laser deposi-



tion (PLD) of thin films [37] and in liquid is the pulsed laser ablation in liquid (PLAL) [38].

Laser ablation is a multiscale process and it is particularly difficult to establish a functional relationship between the different phenomena involved, such as laser-matter interaction, plasma formation, liquid boiling and bubble formation (in the case of pulsed laser ablation in liquid), nanoparticle genesis, as well as growth and stabilization effects [39]. The process consists in a high energy laser pulse that interacts with a bulk target creating a hot and dense plasma. The subsequent rapid expansion process (both in gas or liquid environment) results in plasma quenching and in a shock wave emission that, in the case of ablation in liquid, leads to a bubble formation and expansion for a sub-millisecond time scale, until energy is dissipated and the bubble collapses (shown in Fig. 2.1) [40, 41]. All of these processes are of fundamental importance for nanoparticles generations.

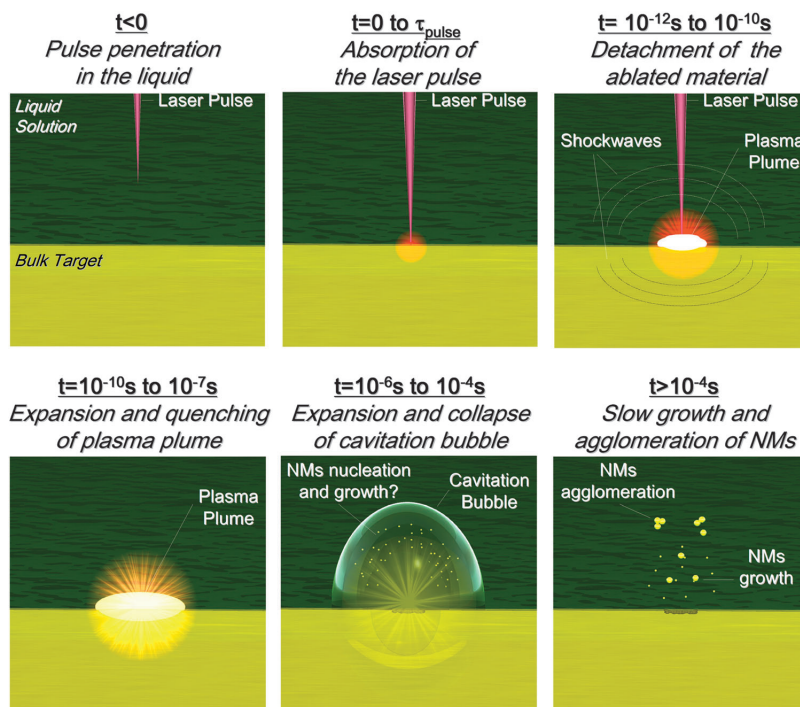


Figure 2.1: Sketch of phenomena occurring during PLAL. Reproduced from Ref. [41] with permission of Physical Chemistry Chemical Physics Owner Societies

The incident laser pulse penetrates into the surface of the material within a certain penetration depth. This dimension is dependent on the laser wavelength and the refraction index of the target material and is typically in the range of 10 nm [42]. The strong electrical field generated by the laser light is sufficient to remove electrons from the bulk of the penetrated volume. The free electrons oscillate with the electromagnetic field and can collide with the bulk atoms, thus transferring some energy to the lattice. The irradiated surface is then heated up and vaporized [43].

To better understand the effect of the laser beam on the irradiated material, electronic and lattice dynamics have to be taken into account.

Electron transitions happen through inter- and intra-band when photons in the typical laser wavelength (visible range) are absorbed. A non-equilibrium electronic distribution is induced by the laser beam with a subsequent thermalization via electron-electron and electron-phonon interactions [44].

Electron thermalization is also a function of the specific electronic structure of the irradiated sample:

- for insulators, the laser photons can promote electrons from the valence band to the conduction band creating electron-hole pairs. The subsequent recombination restores the equilibrium condition on a time scale that, depending on the material properties, can be as long as nanoseconds [45].
- metals behaves differently. The simplest approach is explained by the Drude model [46], where the electron scattering time  $\tau_D$  is related with the electrical conductivity  $\sigma_{el}$  as:

$$\sigma_{el} = Ne^2\tau_D/m \quad (2.0.1)$$

where  $e$  is the electron charge, and  $m$  the electron mass and  $N$  the conduction electron density. Drude model simply provides the electron scattering time, typically of few femtoseconds, even under equilibrium conditions. More sophisticated approaches must be employed because the laser photons induce a non-equilibrium electronic distribution. The Fermi liquid theory describe the lifetime of excited electron that is due to electron-electron collisions [47].

However, electrons do not only scatter between each other, but they can also interact with the lattice by means of the electron-phonon scattering processes. A simplified approach, directly related to laser interaction with solid was proposed by P. B. Allen [48]. It is based on the electron and phonon distributions changes due to collisions. In order to evaluate the variation of the electronic temperature  $T_e$ , it was derived an expression for the energy transfer between the photoexcited electrons and the lattice that can be written as a simple rate equation:

$$\frac{\partial T_e}{\partial t} = (T_L - T_e)/\tau_{ep} \quad (2.0.2)$$

where  $T_L$  is the lattice temperature and the electron-phonon coupling time  $\tau_{ep}$  depends on the electronic temperature, a coupling constant  $\lambda_p$  ( $\approx 0.5$  [49]) characteristic of the material and the Debye frequency  $\omega_D$  of the irradiated solid as:

$$\tau_{ep} = (2\pi k_b T_e)/(3\hbar\lambda_p\omega_D^2) \quad (2.0.3)$$

From the relation 2.0.3, it is possible to estimate that the energy transfer from the electrons to the lattice occurs on the picosecond time scale and is around two orders of magnitude slower than the electron-electron scattering time.

So, it is clear that electrons and lattice dynamics can be developed separately upon laser irradiation, and the time evolution of the energy of the electron gas and the lattice can be described by two separate, but coupled heat transport equations:

$$C_e \frac{\partial T_e}{\partial t} = \nabla(k_e \nabla T_e) - H(T_e, T_L) + S(t) \quad (2.0.4)$$

$$C_L \frac{\partial T_L}{\partial t} = H(T_e, T_L) \quad (2.0.5)$$

where  $H(T_e, T_L)$  is the rate of energy transfer between electrons and lattice ( $Wm^{-3}$ ),  $S(t)$  represents the absorbed laser power per unit volume ( $W \cdot m^3$ ),  $\nabla(k_e \nabla T_e)$  is the diffusive electronic heat transfer,  $C_e$  and  $C_L$  are the electronic and lattice specific heat. These coupled differential equations represent the celebrated Two-Temperature Model (TTM) developed by Anisimov [50]. Various aspects on the TTM have been investigated theoretically and experimentally [51, 52]. Equations 2.0.4 and 2.0.5 are useful as long as the laser pulse duration pulse is comparable to the typical time constants of electron-electron and

electron-phonon couplings. For pulse duration shorter than 50 fs, electrons and lattice dynamics are essentially decoupled because the lattice cannot respond on a time scale as short as the pulse duration.

For pulse duration of few ps, the energy is transferred to the lattice within the pulse duration. For longer pulse duration, the electronic and lattice dynamics are essentially similar since the rate of energy exchange between them is shorter respect to the pulse duration. In this last case, the TTM can be simplified, obtaining:

$$(C_e + C_L) \frac{\partial T}{\partial t} = \nabla(k_e \nabla T) + S(t) \quad (2.0.6)$$

The electron specific heat can be neglected because it is much smaller than the lattice one.

The processes that take place when the laser beam hits the material depend on the laser energy. The incident laser pulse induces extremely rapid heating of a significant mass/volume of target material. This may cause phase transitions, and introduce high amplitude stress waves in the solid target. Material will start to boil off and expand into the gas phase with the consequent formation of nanoparticles [53]. The main formation mechanisms of laser ablated nanostructures are mainly based on:

- thermal and electronic vaporization: the formation of nanostructures was attributed to the combination of ultrafast quenching of a hot plasma and its interaction with the surrounding medium [54].

Thermal contributions will generally dominate when using longer (e.g. nanosecond duration) laser pulses. Relatively long pulse duration allows photon coupling with both the electronic and vibrational modes of the target material.

Electronic contributions are more evident when using very short (i.e. sub-picosecond) pulse durations that allows photon coupling with only the electronic modes of the material.

- the explosive ejection of nanodroplets. The primary ablation products were mainly metal nanodroplets, which were ejected into the liquid medium at a high speed [55].

At a high sufficiently laser power (starting from around  $0.1 J/cm^2$ ), the mate-

rial is typically converted to plasma which contains various energetic species including atoms, molecules, electrons, ions, clusters, particulates, and molten globules. Therefore it possesses some unique characteristics such as high temperature, high pressure, and high density [56].

Hereafter a brief description of the Pulsed Laser Deposition technique and the plasma expansion in vacuum and in gas is given.

## 2.1 Pulsed Laser Deposition

Pulsed laser deposition (PLD) is a growth technique in which an intense laser pulse is focused onto a solid surface placed inside a vacuum chamber. Above a certain power density ( $< 1\text{J}/\text{cm}^2$ ), the material is vaporized from the target surface forming a plasma plume which expand in ultrahigh vacuum or in the presence of a background gas and is then deposited as a thin film on a substrate. The typical PLD setup and process is schematically shown in Fig.2.2.

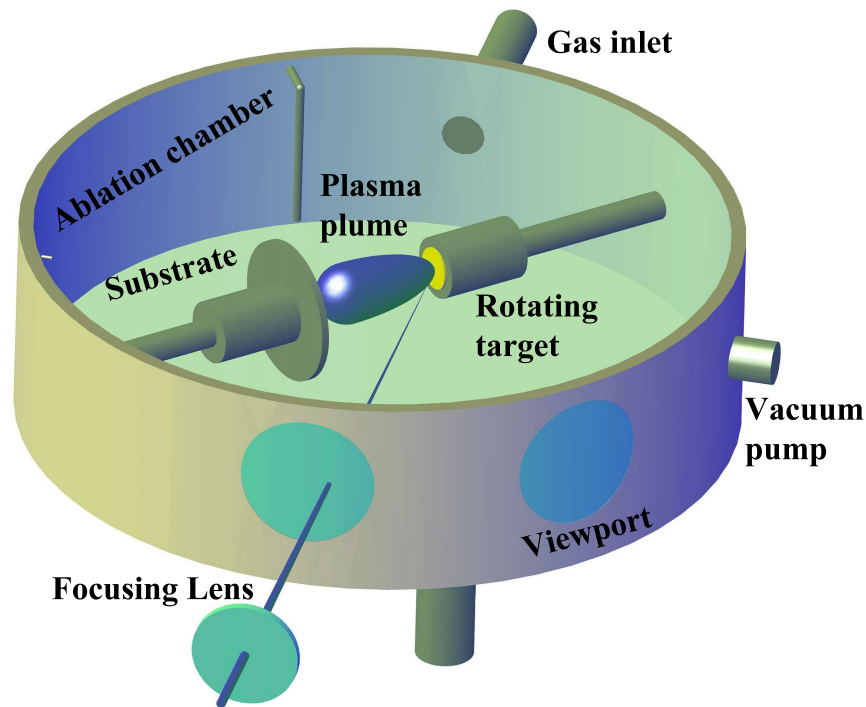


Figure 2.2: Scheme of a typical PLD setup.

The technique of PLD has been successfully applied to fabricate thin films for a large classes of materials including ceramic oxides, nitrides, metallic multilayers, and various superlattices [37]. An accurate control of several experimental parameters allows to tailor both NP size and the surface morphology of thin films, and hence their structural, optical and electronic properties (as shown in Fig.2.3). The deposition process characterized by energetic species usually lead

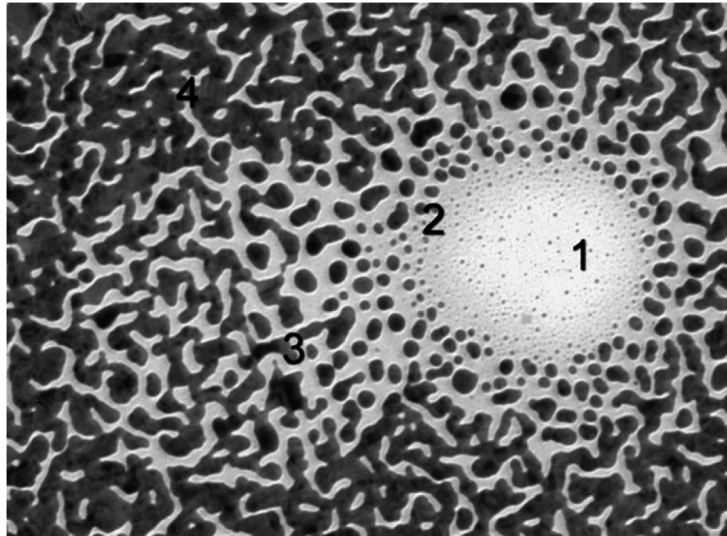


Figure 2.3: Surface morphology (SEM) of silver NPs films deposited in Ar atmosphere at 10 Pa. The film formation mechanism at different times can be observed thanks to the occurrence of a spherical droplet that masked a portion of the substrate leaving then the surface at different times during the deposition process. The circular area (1) is characterized by small isolated particles with dimensions in the range 1-3 nm. At the border of this area larger particle, but still isolated, can be observed, area (2). Such particles then start to coalesce as can be seen in area (3). The region (4) is characterized by a percolated Ag network that covers in a nearly complete way the substrate. Reproduced from Ref. [57] with permission of Applied Surface Science.

to compact and smooth surfaces, while thin film formation by species with low kinetic energy proceeds through cluster coalescence on the substrate surface [58] PLA in vacuum is a deposition technique in which the produced particles can have very high kinetic energy. The energy of the species in the laser generated plasma can be tuned by performing the process in presence of inert or reactive

gases involving the collision processes between the expanding plasma and the background gas. The plasma-gas interaction is a very complex process that involves many different phenomena such as the loss and spreading of kinetic energy of plasma species, chemical reactions, shock wave formation and propagation [57]. For these reasons, film growth is related in a complex way to the background gas nature and pressure and it is important to study the plasma expansion.

### 2.1.1 Plasma expansions

Basically, when a high-energy laser pulse hits the surface of a material, a plasma ball develops from target surface and begins to expand, driven by its high internal pressure. This plasma is composed of highly ionized or atomic species with an initial density of about  $10^{20}\text{cm}^3$ . A free expansion of the plasma plume is observed in vacuum; it is a collision free process, then there is no energy transfer and can be considered an adiabatic process. In this conditions the plume expansion is characterized by an ellipsoid, according to the Anisimov model [59]. The thermal equilibration of the plasma is due to the multiple scattering between plume species, resulting in the formation of the so-called Knudsen layer [60]. The kinetic energy of emitted ions generally follows a Boltzmann distribution but the formation of the Knudsen layer modifies the Maxwell-Boltzmann distribution to a shifted function, which includes the centre of mass velocity given by:

$$f(v) = A \left( \frac{m}{2\pi k} \right)^{\frac{3}{2}} v^n \exp \left( \frac{-m(v-u)^2}{2kT} \right) dv \quad (2.1.1)$$

where  $k$  is the Boltzmann constant,  $v$  is the speed along the propagation direction,  $m$  is the mass of the particles,  $T$  is the stream speed,  $u$  is the stream velocity, which describes the angular distribution of the propagation, and  $n$  is an integer (typically 3 or 4).

A free expansion occurs also in the presence of a background gas, over a limited time interval just after the arrival of the laser pulse, afterwards the collisions between the plasma species and the ambient gas lead to a departure from the free expansion. Collisions start to reduce the kinetic energy of the plume species and to increase the number of chemical reactions between the

plume and gas. The plume dynamics is strongly affected by the gas type and pressure. At a low background pressure ( $<1$  Pa), the plume expansion is similar to the ablation in vacuum. Increasing the background gas pressure, it influences progressively the plume dynamics. At intermediate pressures (10-100Pa) the mean free path of the plume species is reduced. In these conditions the plasma compresses and pushes gas molecules ahead of the contact surface with the plasma and the gas, leading to the formation of a shock wave (see Fig. 2.4) [61].

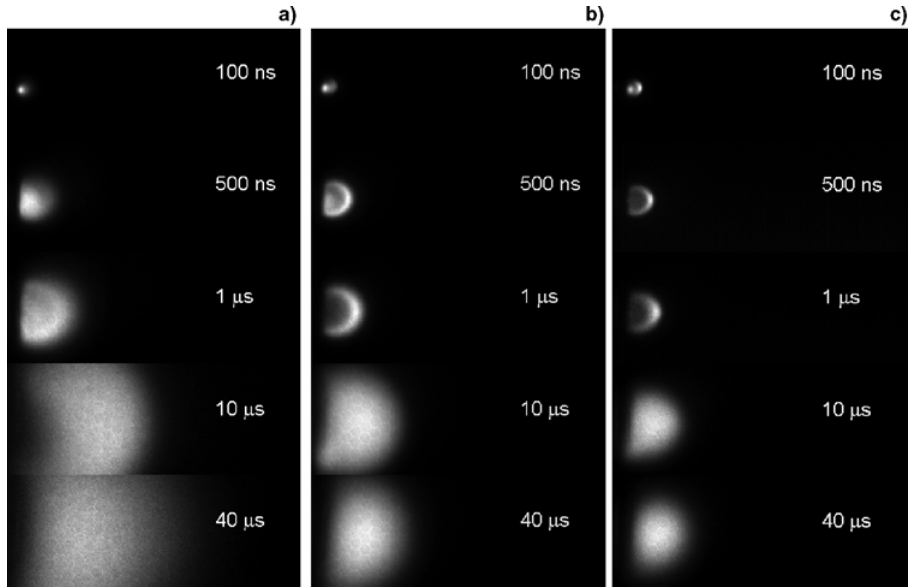


Figure 2.4: Ag plasma expansion in presence of (a) 10Pa, (b) 40Pa and (c) 100Pa of Ar at different time delays respect to the arrive of laser pulse. Reproduced from Ref. [61] with permission of Laser and Particle Beams

The position of the propagating shock wave as a function of time is given by the drag model for the early expansion regime [62]

$$x(t) = a(1 - e^{-bt}) \quad (2.1.2)$$

where  $a$  is the stopping distance of the plasma. At larger distance and high enough gas pressure, the shock wave model describes better the position of the propagating shock wave [31]:



$$x(t) = \xi_0 \left( \frac{E_0}{E} \right)^{\frac{1}{5}} t^{\frac{2}{5}} \quad (2.1.3)$$

where  $\rho_0$  is the density of the unperturbed background gas,  $\xi_0$  is the geometrical factor and  $E_0$  is the plasma energy.

The shock wave develops as soon as the mass of the ablated material becomes small compared to the mass of the gas surrounding the shock wave. This condition is verified increasing the distance from the target as the pressure of the background gas is lowered. When the shock wave develops the kinetic energy of the plasma is converted through collisions in thermal energy with an increase of both luminous emission and temperature at the contact surface between the plasma and the buffer gas.

At pressures higher than 100 Pa, a stronger confinement of the plume with a short stopping distance takes place. The confinement effect is deeply dependent on the gas pressure (see Fig. 2.5). This behaviour is more evident in the case of laser ablation in a liquid environment. The main differences are related to the competition between elementary processes and to the degree of energy exchange with the surrounding environment.

The plasma is strongly confined by the liquid, so that it rests at density of the order of  $10^{20} \text{ cm}^{-3}$ , because of the low compressibility of the liquid. Under these conditions atoms and ions in the plasma phase are affected by the Debye-Hückel effect so that most excited levels are not allowed and radiative recombination is the predominant process [63, 64].

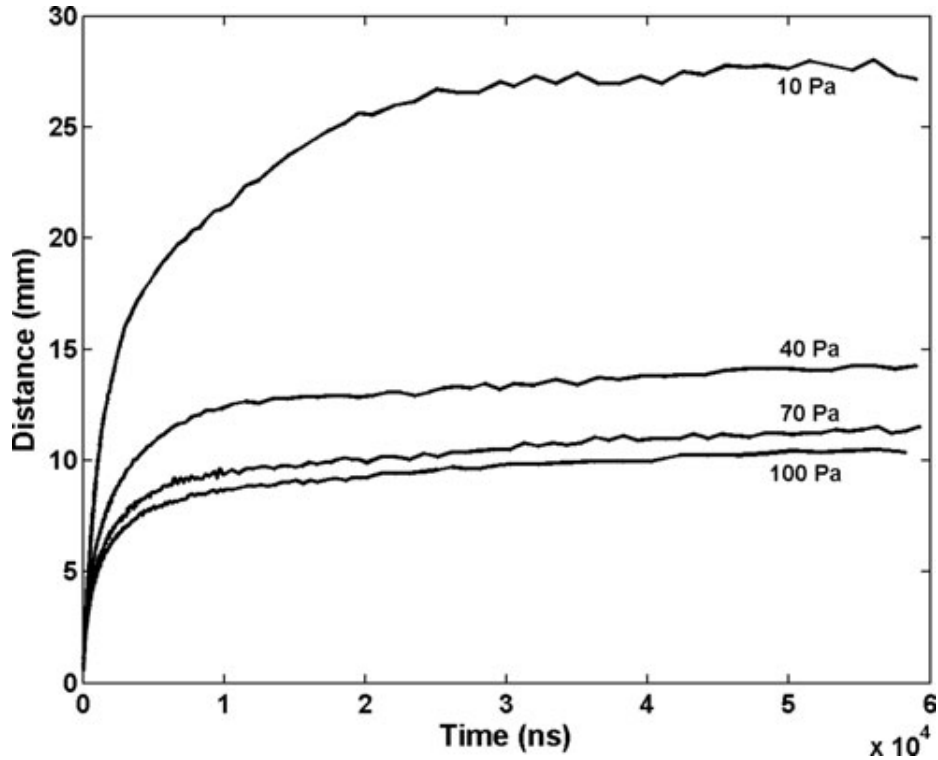


Figure 2.5: Position of the Ag plasma front edge as a function of the time at different Ar pressures. Reproduced from Ref. [61] with permission of Laser and Particle Beams

## 2.2 Pulsed Laser Ablation in Liquid

Pulsed laser ablation in liquids (PLAL) is based on a similar approach respect to PLD with the difference that the solid target is located into a liquid. This generates new physical phenomena and allows the production of a new variety of nanoparticle colloids. Since the pioneer report of Patil et al. [65] on PLAL, it has been a scalable and versatile method for NP synthesis. The derivative techniques of Laser Melting in Liquid (LML) and Laser Fragmentation in Liquid (LFL) allow precise size control of the synthesized colloidal nanomaterials from few nm up to several micrometers.

Immersing a workpiece into a liquid or employing a liquid film has many advantages, such as lowering the heat load on the workpiece, producing debris-free treated surfaces, confining the vapor and plasma, and increasing the shock

pressure on the surface [66]. Moreover, chemical reactions can occur in the interaction between the ablated species (ions, atoms, and atom clusters) and the surrounding liquid. Generally a fraction of the ablated material is inevitably chemically oxidized or reduced at the surface of the NPs during PLAL in relation to the liquids adopted during the process.

The presence of liquid at the interface with the solid during the ablation process has a strong impact on the process itself. Firstly it has to be considered that before reaching the solid surface the laser beam has to penetrate the liquid layer. Along this path inside the liquid the focal length of the focusing lens will change due to refraction or even self-focusing. So, the focal length will increase as:

$$\Delta f = l \left( 1 - \frac{f}{\sqrt{n^2 f^2 + (n^2 - 1)r^2}} \right) \quad (2.2.1)$$

where  $f$  is the focal length of the focusing lens in air,  $l$  is the liquid thickness,  $r$  is the radius of unfocused laser beam, and  $n$  is the refractive index of the liquid. The laser beam will be attenuated when it passes through the liquid because of the absorption of photons and of their scattering by liquid molecules. It is possible to write the light intensity that reaches the target as:

$$I_v = I_{v0} \exp\left(-\int_0^x \mu_v dx\right) \quad (2.2.2)$$

for a path of length  $x$ , where  $\mu_v$  is the attenuation coefficient that contains both absorption and scattering contributions.

Generally, the liquid is assumed to be transparent. Attenuation by laser-produced particles is more significant upon increasing the ablation time which results in higher particles concentration. This happens specially for noble metal nanoparticles, when the laser wavelength is in the excitation range of surface plasmon resonance of the nanoparticles [67]. Absorption of photon energies by laser-produced particles may cause secondary laser processing of the particles themselves such as laser fragmentation and laser melting. After passing through the liquid, the focused laser beam irradiates on the solid surface. The laser ablation of the solid surface produces a shock wave in order to relax the excess energy. The shock wave is the formation of discontinuities in flow variables, such as density and refraction index [31]. The interaction of the laser beam with the solid surface produces the plasma that is quenched during his expan-

sion into the liquid leading to the growth of a vapor layer into a cavitation bubble. The laser ablation process is usually defined as an high temperature and high pressure process. This is usually related to the initial plasma state (few hundreds of nanosecond) rather than cavitation bubble (sub millisecond). The laser-induced cavitation bubbles are considered to be an important site for nanoparticle generation. It is necessary to discuss deeply bubble dynamics throughout the entire process to understand their role in the nanoparticle formation mechanism. This topic was object of my investigation and it will be described in the next paragraph.

### 2.2.1 Cavitation bubble formation

The process starts with the expansion and the ignition of the plasma after the interaction of the laser pulse with the target surface. Plasma temperature and extension influence size and productivity of the generated nanoparticles, as well as on the induced cavitation bubble. Within the first microseconds the plasma transfers its energy to the surrounding liquid inducing its vaporization and the formation of a cavitation bubble [33]. The formation of cavitation bubbles is an important stage involved in PLAL and it plays an important role during nanoparticle formation [68]. Moreover, it has been accepted that the laser-induced plasma and the dynamics of the generated cavitation bubble have a critical role for nanoparticles productivity.

The thin layer of vapour grows around the plasma and it is characterized initially by high pressure and temperature. It generates a cavitation bubble expanding against the surrounding liquid. The dynamics of cavitation bubbles includes an expansion stage and, after the cavitation bubble reaches its maximum height at approximately 20% of its lifetime, it begins to shrink. This process can be repeated several times, reproducing a behaviour similar to that of damping oscillations [69]. The expansion and shrinking phase are almost perfectly hemispherical whereas the second (rebound) bubble is neither hemispherical nor symmetric throughout its evolution. Fast shadowgraph images were acquired with the experimental setup described below and allows the determination of the bubble radius at each observation time (see Fig.2.6). Sometimes asymmetric shrinking of the first bubble is reported, with inward jet, and this effect could

be linked to the wetting angle of the initial bubble, indicating that shrinking symmetry may depend on target wettability and temperature. This shrinking stage plays an important role in determining the process of nanoparticles production because part of the ablated material can be driven back to the target surface instead of being delivered into the solution [69].

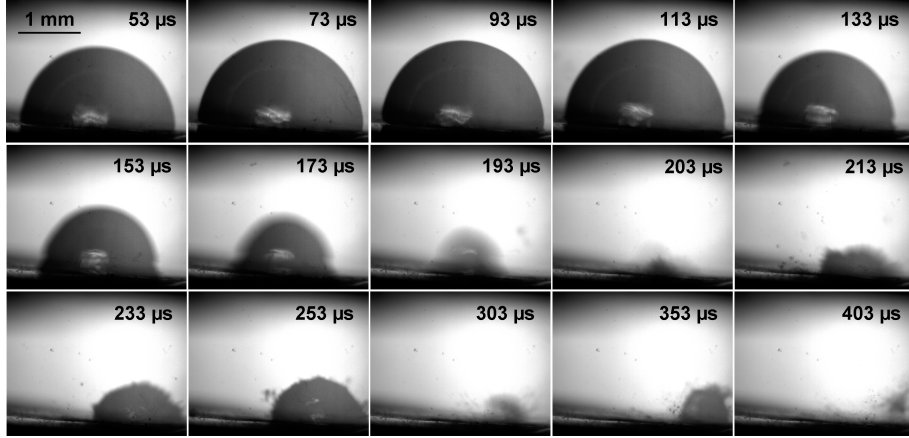


Figure 2.6: Dynamic evolution of cavitation bubble when a laser beam is focused onto a flat target surface.

The lifetime of the first cavitation bubble depends on the laser fluence, and, because the ablated mass scales linearly with the laser fluence, one would expect it to be proportional to the heat available to vaporize a certain volume of the liquid. Accordingly, the bubble volume scales with fluence and, keeping it fixed, the bubble volume may increase with the liquid compressibility and decrease with its density [36].

The bubble evolution is described by the Rayleigh-Plesset model. It starts from the continuity equation and the Navier-Stokes equation and it assumes an incompressible and nonviscous liquid. The Rayleigh-Plesset equation describes the bubble radius evolution as a function of time:

$$R\ddot{R} + \frac{3}{2}\dot{R}^2 = \frac{1}{\rho}(P_B(t) - P_l) \quad (2.2.3)$$

where  $R$ ,  $P_B$ ,  $P_l$ ,  $\sigma$  and  $\rho$  denote the bubble radius, the internal pressure, the surrounding liquid pressure, the fluid surface tension and the liquid mass density, respectively [70]. The Rayleigh-Plesset equation, can be further adapted

by considering the viscosity of the liquid and the surface tension of the liquid in the pressure terms [71, 72]. Anyway this equation fails to describe the bubble dynamics after the collapse of the first bubble.

On the basis of studies of laser-induced spherical bubbles in liquid, the Gilmore model might be better suited to describe the cavitation bubble dynamics occurring during PLAL [73]. This model includes second-order compressibility terms, accounting for the loss of bubble energy due to the radiated pressure waves [74]. It allows to calculate thermodynamic variables during bubble expansion and shrinkage starting from cavitation bubble images. In this way the observation of bubble dynamics throughout the entire process can help to understand its role in the nanoparticle formation mechanism.

In relation to the increasing demand to have nanoparticles solution with high concentration it is necessary to increase ablation time. This can cause damages on target surface that could influence nanoparticles formation. In this context we are interested to study bubble shape and dynamics in order to understand if these changes can leads to different effects in terms of bubble dynamics and ablation efficiency.

In next chapter there will be presented and discussed the results obtained following the cavitation bubble dynamics ablating a flat and an ablated-damaged silver target. A correlation between the cavitation bubbles dynamics, nanoparticles size and ablation efficiency as a function of the number of the applied laser pulses is studied.

## 2.3 Laser post-processing of colloids

Pulsed laser processing of particles in liquid (PLPPL) is a technique in which a laser beam irradiates the particles that are suspended in the liquid that surrounds them. This process enables chemical conversion and modification of particle sizes and can be subdivided into two different processes. One is the pulsed laser fragmentation in liquids (PLFL) whereby particles are fragmented resulting in a reduced particle size. The other processing technique of PLPPL is the pulsed laser melting of particles in liquid (PLML) where particles are transferred into a molten state and resolidify as spheres. In the case of

PLFL, these particles release the smaller product particles that are captured in the liquid. If the educt particles are exposed to laser parameters causing PLML, they melt, fuse and resolidify as spheres while the particle size either increases or remains constant. Whether PLFL or PLML occurs during PLPPL is depending on the laser parameters and the material response to incident light. However, PLML is unique due to the fact that by irradiation with an electromagnetic wave the energy is directly transferred to the particle. Thus the particle can melt while it is in a liquid environment, or is fragmented without any surfactants or impurities.

Precise control of laser fluence enable to study the effect of energy density on particle response causing PLFL or PLML. In order to reach sufficient energy density for both PLFL and PLML, especially in the case of metal oxide materials, the laser beam has to be focused. The experimental design used was developed by Lau [75] and it is showed in Fig.2.7. The setup is composed by a bath containing the NPs colloidal solution that initially flows in a capillar tube and is then free to flow down. During his path the free liquid jet is hitten by the laser beam. The laser energy is then absorbed by the particles in the liquid flow causing PLFL or PLML depending on laser parameter.

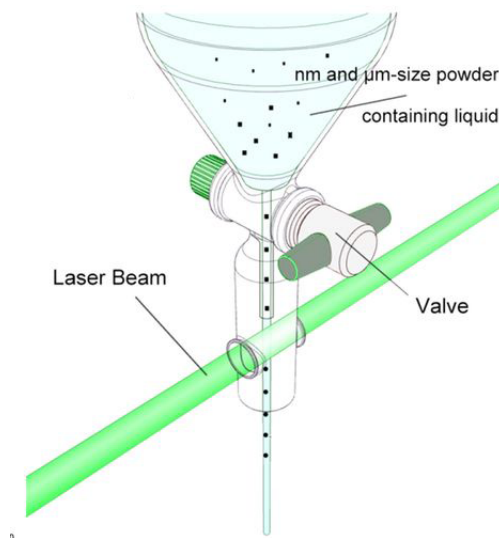


Figure 2.7: Scheme of the experimental design used for PLFL and PLML. Modified and reproduced from Ref. [76] with permission of Scientific Report

### 2.3.1 Laser Melting in Liquid

Pulsed laser melting in liquid (PLML) is a technique to generate sub-micrometer spheres (SMS) starting from micro, sub-micro or nanoparticles. Particles are exposed to a non-focused pulsed laser beam (about 10-300  $mJ/cm^2$ ) and consequently the energy absorption change their size or shape. In this technique, the irradiation causes aggregates in the colloidal solution to melt and form droplets; rapid cooling at the end of each pulse causes the droplets to form spherical particles [77]. Pulsed laser melting in liquid (PLML) has emerged as a simple approach to synthesize submicron spheres (SMSs). It can be applied for a large variety of materials. Typically lasers with long pulse durations in the nanosecond regime are used. However, during melting the energy absorbed by the particle will be dissipated promptly after laser-matter interaction following the temperature decrease within tens of nanoseconds and hence limiting the efficiency of longer pulse widths.

### 2.3.2 Laser Fragmentation in Liquid

The structure and size of particles suspended in liquid can be modified by an intense laser light excitation. Their size can decrease if the target particles are irradiated with a sufficient energy dose, depending on laser parameter. This fabrication method of nanoparticles from suspended micro or nanoparticles is mainly described as laser fragmentation. For all processes, the particle size distribution changes and this is usually associated with an educt-product particle mixing. Thus, investigation of the smallest fraction after laser fragmentation is most convenient, because the nanoparticles can be extracted from educt particles by sedimentation of the educt (micro) particles by using a centrifuge. In Fig. 2.8 is shown a disc centrifuge measurement on samples before and after the Laser Fragmentation process performed using the setup previously described. The samples were composed by a mixture of tungsten oxide ( $WO_3$ ) and Cesium Carbonate ( $Cs_2CO_3$ ) powder milled together and dissolved in ethanol. It is plotted the relative surface distribution as a function of particles size. The distribution was normalized respect to the maximum. It is evident that the LF process reduce the amount of bigger particles in the samples, driving to a tailored and monodisperse size distribution function.



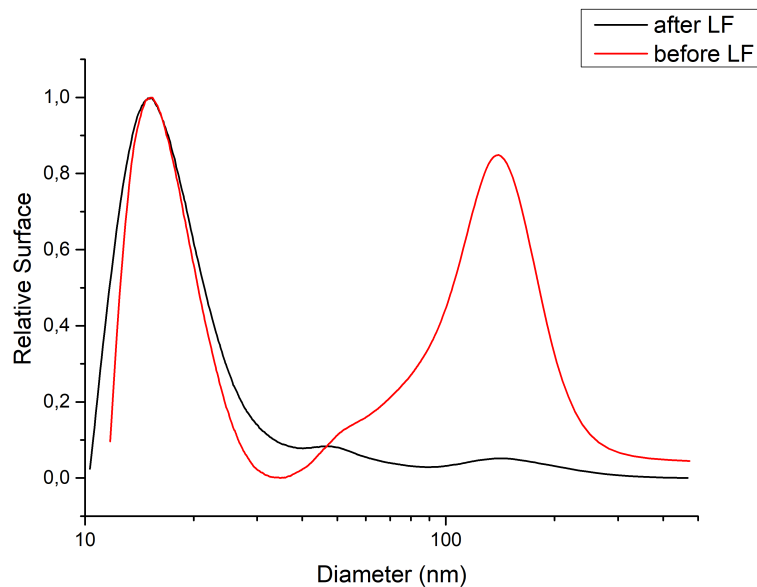


Figure 2.8: Results of ADC measurement on Cesium Tungstate colloidal solution before and after laser fragmentation in liquid. The distribution is normalized respect to the maximum value.

All the techniques discussed previously were applied in this thesis to prepare gold, silver and rhodium nanoparticles for several kinds of applications, such as:

- detection of molecules based on Raman spectroscopy. In particular there were used some standard literature and some new drugs used for Parkinson's disease;
- in a drug delivery system gold and silver were loaded in a polymeric matrix in order to increase light absorption at a certain wavelength and improve the drug release efficiency;
- the realization of a resistive hydrogen gas sensor based on chemical oxidation/reduction.

Even though nanoparticles were proposed to have various possibilities in application due to their unique properties, some materials and techniques still remain inaccessible due to a missing link between synthesis and application or

up-scaling. Appropriate choice of the synthesis technique is therefore relevant in this context.

## Chapter 3

# Cavitation Bubbles on a re-irradiated target

The cavitation bubble mechanism, described in the previous chapter, exhibits important implications in the control of particle size distributions. Microsecond resolved small-angle X-ray scattering studies during nanosecond PLAL identified a bimodal nanoparticles distribution already inside the laser-induced cavitation bubble, but they could not clarify the origin of that bimodality [78].

Even though the dominant mass of nascent nanoparticles is confined within the cavitation bubble (except some particle droplets jetted through the phase boundary of the bubble), their size distribution already can be narrowed significantly in this gaseous phase by adding micromolar amounts of electrolytes to the liquid prior to laser ablation [79]. These ions are also present within the plasma and the cavitation bubble, and they quench the size and increase the colloidal stability by electrostatic repulsive forces through adsorption on the surfaces of the particles [79]. This points towards a ripening process inside the expanded bubble. However, ideal conditions occur if the target and the water are continuously refreshed during the ablation process. In fact, several researchers have investigated the continuous production of nanoparticles using a moving, wire-shaped target [80, 68] and demonstrated a different cavitation bubble dynamics compared to a flat plate-shaped target [78].

However, to date, the influence of individual changes in the cavitation bub-

bles on the size of the nanoparticles has not been determined. Scaramuzza et al. used targets with confined geometries and investigated their impact on the particle sizes with a focus on the temperature gradient inside the target, induced by the interaction with the nanosecond laser [81]. The particle size was found to be tunable by the target rotation speed, which causes different hydrodynamic regimes in close proximity to the target surface. Lam et al. [72] calculated the concentration ratio of ablated inorganic species and liquid molecules (by considering bubble volume and pressure) and found that the bubble consists mostly of vaporized molecules of the liquid. Looking at sub-microsecond timescales when the volume of the bubble is minimal, highly concentrated atoms of the ablated species still undergo coalescence on a sub-nanometer time scale and form solid nanoclusters. Note that the gas phase theory of coalescence indicates that the condensation is proportional to the squared value of the particle concentration [82]. Thus, this points to the importance of knowing the intra-bubble concentration. To date, it is unknown whether this concentration is affected by the size of the bubble or if it changes under multiple-pulse conditions.

In the next paragraph, it is described how a defined series of pulse number changes a silver target's surface geometry. In particular, the focus will be on the dynamics of the cavitation bubble following pulsed laser induced damage on a silver target immersed in water and then on the resulting nanoparticles properties.

### **3.1 Shadowgraphy setup for cavitation bubble imaging**

A custom-designed shadowgraphy system was developed by using an ablation flow chamber. In Fig. 3.1 is shown a scheme of the experimental setup used for simultaneous PLAL and imaging by shadowgraphy in liquid flow. It consists of:

- a peristaltic pump which provided a liquid flow rate of 35 ml/min. This avoid the screen effect of already-existing nanoparticles and persistent microbubbles due to the scattering and absorption of the laser beam.

- A glass bottle for pressure equilibration between the pump and the ablation chamber used in order to remove the pump stroke.
- A flat silver plate (1 mm thick) as a target placed inside the ablation chamber and fixed perpendicular to the incoming, horizontal laser beam.

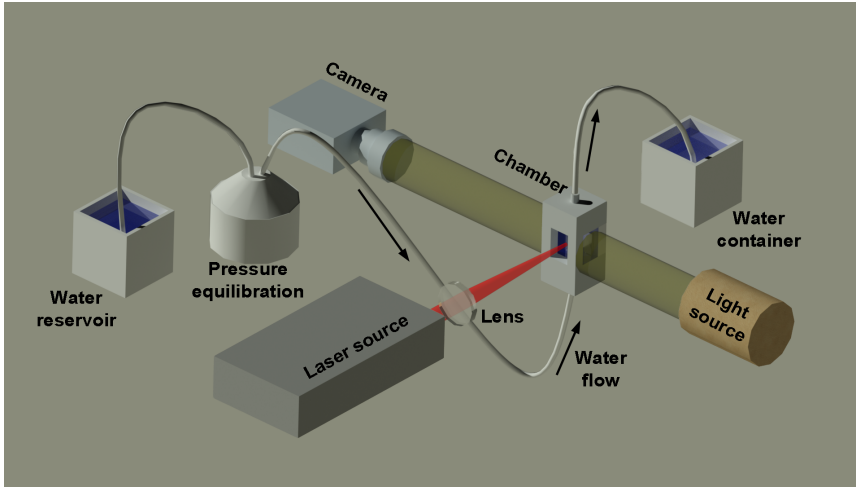


Figure 3.1: Experimental setup used for simultaneous PLAL and imaging by shadowgraphy in liquid flow.

In details, the chamber was custom-made by the 3D-printing of an acrylonitrile butadiene styrene (ABS) filament. An Nd:YAG laser source (Innolas, SpitLight DPSS250-100) with a pulse duration of 9 ns and a wavelength of 1064 nm was focused by a lens that had a focal length of 75 mm and was located 65 mm from the target. The repetition rate was set at 0.2 Hz, ensuring that the ablation conditions for each successive pulse are not altered because the time between two pulses is much higher respect to the determined residence time (0.1 s) of the observable persistent bubbles (Fig. 3.2).

The pulse energy was set at 20 mJ, then the calculated laser fluence, without considering attenuation of laser intensity in the water layer, was 46 J/cm<sup>2</sup>. The effective laser fluence  $F_{eff}$  was calculated by considering this attenuation, it was 11 J/cm<sup>2</sup>. For this calculation the absorption coefficient of water at the laser wavelength of 1064 nm ( $\alpha = 0.61 \text{ cm}^{-1}$ ) was considered and inserted in

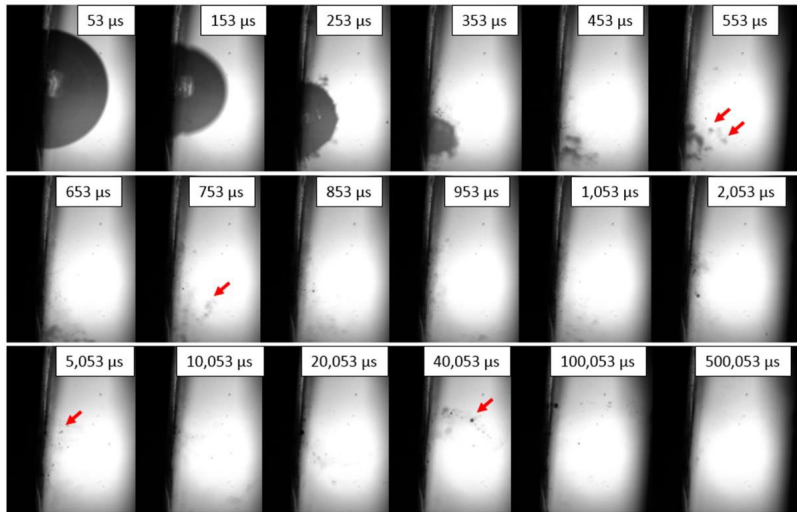


Figure 3.2: Frames of the interior of the ablation chamber at different delays after laser impact with an applied volume flow of water are shown. The cavitation bubble vanished after 500-600  $\mu\text{s}$  but some persistent microbubbles (exemplary marked by arrows) remained present inside the chamber until 100 ms

the Lambert-Beer law [83]. The ablation spot size was 420  $\mu\text{m}$ . A light source (flashlight, Led Lenser P7, 450 lm) and a camera (Basler acA1600-60, lens: Sill optics correctal T/1,5) were placed perpendicular to the laser beam and to the direction of liquid flow (Fig. 3.1) to acquire images of the bubble and to record individual frames of the cavitation bubble.

The gating time was 10  $\mu\text{s}$  and the intrinsic delay of the system was 43  $\mu\text{s}$ , which resulted in a fixed delay of 53  $\mu\text{s}$ . This is inherent since the laser was operated as the master, and the camera was a slave. The images are collected by:

1. changing the delay time of the camera to study the dynamics of the bubbles
2. keeping the delay time of the camera constant at 83  $\mu\text{s}$  with the variation of the pulse number applied to the same spot on the target

In this setup, each frame that was recorded represented a single laser pulse ablation event. Therefore, several pulses were fired while the camera delay was changed manually to acquire movies of the bubble during its entire lifetime.

## 3.2 Cavitation bubble by changing the number of laser pulses

The evolution of the microscopic crater on the surface that was induced by subsequent laser pulses is a model case for the investigation of differences between single-pulse studies, engraving, and microstructuring of the surface of the target that occurs during continuous PLAL. The morphology of each cavitation bubble that occurred after each new laser pulse on the exact same position on the target was examined. For each laser pulse that hits the target, a single camera frame was recorded using a constant delay of  $83 \mu\text{s}$ . This was to ensure that the bubble always was recorded at its maximum extension. Fig. 3.3 shows representative frames of this single-pulse bubble observation after drilling a crater. After the first pulse, the cavitation bubble exhibited a characteristic quasi-hemispherical shape with a sharp interface with the water phase. The height of the bubble was in the order of 2-3 mm as was expected for high-energy, nanosecond PLAL [84]. As many as approximately 50 drilling shots preceded the single pulse, and the bubble basically was unaffected by the surface microstructure that was induced on the silver target. Here, it was not focused on incubation during the first few shots.

Already after 100 laser shots on the same target position, the shape of the bubble was changed significantly, indicating that the crater that was drilled into the silver target was beginning to break the symmetry of the target-bubble interface. This might further have affected the hydrodynamics of the liquid droplets as they lifted off from the surface of the solid target. While the absolute height of the cavitation bubble after 100 laser pulses was still the same as after a single pulse, the shape was no longer hemispherical because the outer areas of the bubble that contacted the target were closer to the center of the bubble. The interface between the gas-filled cavitation bubble and the surrounding liquid phase had multiple indentations, and there were some persistent, bubble-like gases that were very close to the interface. Shih et al. recently described similar bubbles as satellite microbubbles [85]. They attributed these microbubbles to the large, spherical nanoparticles that were ejected from the target in front of the expanding outer layer of the cavitation bubble. Still, the process of

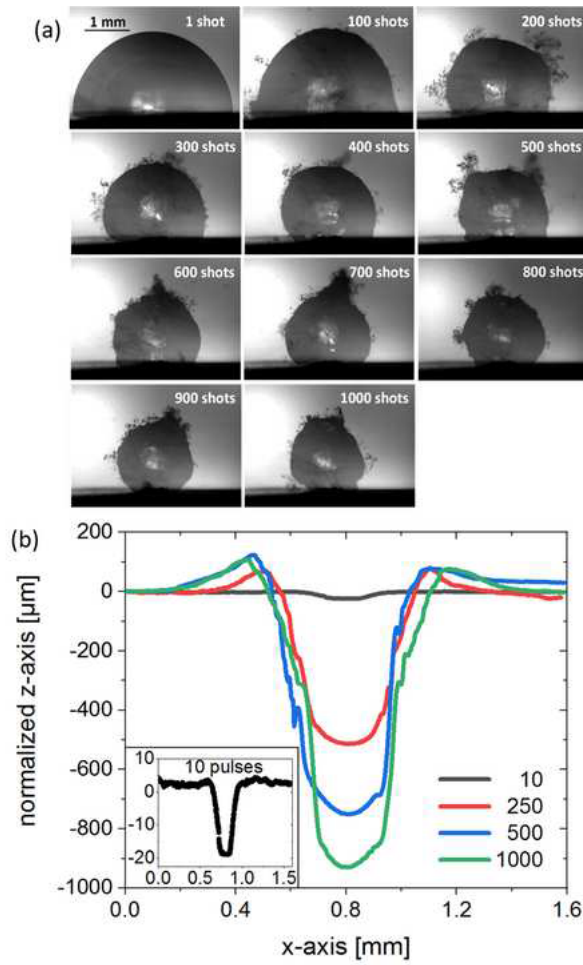


Figure 3.3: (a) Frames of the single laser pulse-induced cavitation bubbles after 1-1000 pulses on the same spot. (b) Line scans of the craters on the silver target recorded by confocal 3D microscopy. All of the datasets were normalized to the zero position.

formation of persistent microbubbles by large nanoparticles remains elusive. The experimental conditions used by Shih et al. [85] deviated from the current conditions, where the authors convincingly pointed out the different ablation mechanisms involved in pico-second and nano-second laser ablation. Thus, it is interesting to see that similar adjacent microbubbles formed under nanosecond laser ablation as a function of the pulse number as well.

With the increasing number of laser shots, the induced cavitation bubble



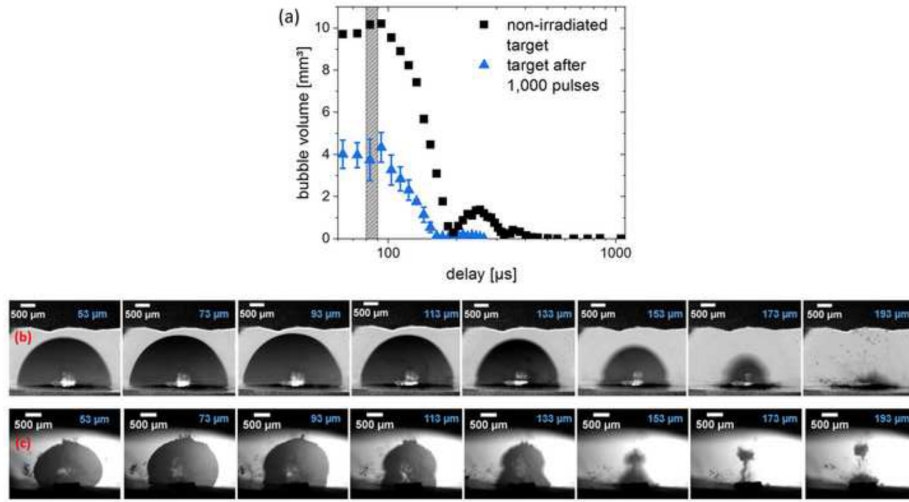


Figure 3.4: (a) Evolution of the volume of the cavitation bubble as a function of the delay time after laser impact on the silver target. The grey bar highlights the gating time of the camera ( $10 \mu\text{s}$ ). (b) Selected frames of the first cavitation bubble induced on a non-irradiated target surface; (c) Selected frames of the first cavitation bubble induced on a target that experienced 1000 pulses in advance.

became more and more spherical instead of hemispherical (Fig. 3.3a, 200-1000 shots) with the satellite microbubbles always present. At the same time, the height and volume of the bubble were shrinking as the number of pulses increased, i.e., the sphericity (vertical radius divided by the lateral radius [68]) increased from 1.01 (hemisphere after single pulse) to 0.94 (quasi-sphere after 1,000 previous pulses). The decreased extension of the cavitation bubble indicated that its overall lifetime was changed [84]. To assure that the trigger delay of  $83 \mu\text{s}$  that was used was sufficient to hit the time point of maximum bubble extension even after a large number of previously fired laser shots, the cavitation bubble was imaged using different delays, i.e., from  $53 \mu\text{s}$  to  $1053 \mu\text{s}$ , and a total of 37 pulses to create an image sequence. The rather low number of pulses was necessary to avoid significant changes in the dynamics of the bubble due to the formation of the crater during the imaging runs. Fig. 3.4a shows the results of the volume of the bubble as a function of the adjusted delay; the grey vertical bar indicates the gating time of the camera ( $10 \mu\text{s}$ ). Both the delay of

the maximum extension and the lifetime of the first cavitation bubble, which is the time until the bubble collapses for the first time, were equal on a non-irradiated target and on a target with a crater that was drilled by 1000 laser pulses. However, the maximum volume of the bubble at 83  $\mu\text{s}$  delay decreased to approximately half of the volume of the bubble on a non-irradiated target. Also, the rebound of the second bubble lacked the energy required to induce a visible third bubble. The lifetime of the entire cavitation and rebound event was reduced significantly from 1000  $\mu\text{s}$  to 250  $\mu\text{s}$ . Fig. 3.4b, c show the changes in the dynamics of the cavitation bubble. On a flat target, the collapse of the bubble evolves towards the target, while the situation changes drastically in the case of single-pulse ablation on a target that already had been ablated 1000 times. The lift-off of the bubble during the first collapse phase was similar to the PLAL of a wire-shaped target [68], probably caused by the symmetry being broken on the surface of the target [86]. The feasibility of using a constant camera delay for observing a cavitation bubble during different stages of laser drilling is evident from Fig. 3.4.

For a bubble with a volume of 10 mm<sup>3</sup>, a fluence of approximately 75 J/cm<sup>2</sup> is expected [87], which does, at first glance, not match the theoretical fluence of 46 J/cm<sup>2</sup> applied during this work. Moreover, if the attenuation of water at the laser wavelength of 1064 nm is taken into account by using the Lambert-Beer Law, and assuming that the liquid layer is 30mm, the effective fluence is 12 J/cm<sup>2</sup> [78]. Indeed, this is a close match with the present effective fluence of 11 J/cm<sup>2</sup> and, as a consequence, the observed bubble volumes are similar. This effective fluence is thus high enough to ensure that the linear regime is reached, because that is where the volume of the bubble increases linearly with increasing laser fluence [87]. It was seen that the ablation volume and the volume of the cavitation bubble are the same for the experimental conditions that were described. They also are the same if the focal point is shifted 1 mm (= target thickness) away from the target surface. The ablated mass was therefore not sensitive to the exact focus position, keeping in mind the increasing crater depths. Still, the distribution of the local laser fluence may undergo changes based on what is known from nanosecond laser drilling in a gas atmosphere [88]. The laser beam undergoes scattering inside the crater, which is partially com-

pensated by light reflection from the walls of the crater. These effects explain the increasing diameter and aspect ratio (depth  $L$  divided by diameter  $D$ ) of the crater as shown in Fig. 3.5, which also shows raw images from the target analysis by confocal 3D microscopy. However, the expansion of plasma inside the crater (= curved surface) is not equal to the expansion of the plasma on the non-irradiated surface (= flat surface) of the target, since the plasma cannot expand freely in all spatial directions [88]. It was shown that the absorption of laser energy in the plasma plume induced by the nanosecond pulses reduced the pulse energy absorbed by the target material to about 30% during laser drilling in air. On the overall, changes in the volume of the bubble cannot be attributed to changes in effective fluence, so they must be linked only to the geometry of the surface.

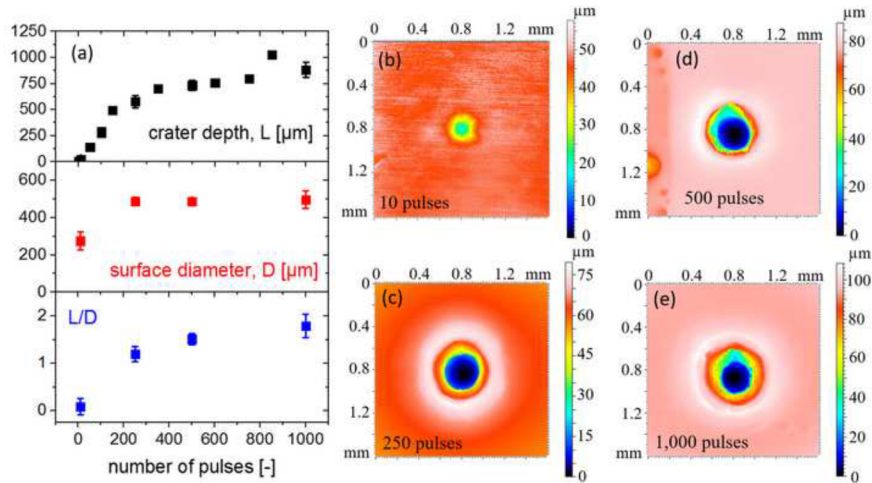


Figure 3.5: (a) Crater depth,  $L$ , crater surface diameter,  $D$ , and aspect ratio,  $L/D$ , as functions of the number of laser pulses.

### 3.3 Correlation between cavitation bubble and ablated mass

Fig. 3.6a shows quantitatively the decrease of the cavitation bubble maximum volume, from  $9.5 \text{ mm}^3$  down to  $3.3 \text{ mm}^3$ , upon increasing the laser shots

until 1000 pulses. This reduction was independent of the volume of the ablation crater, which was 1-2 orders of magnitude less than the volume of the cavitation bubble. Simultaneously, the ablated mass starts to approximately reach a saturation level after 200-300 pulses (Fig. 3.6c). A more detailed view can be achieved by calculating the ablated mass per pulse (Fig. 3.6b) by the first derivative of the exponential fit to the total ablation mass. The ablation rate decreased with the number of pulses and no saturation was observed, indicating that, at some point, no ablation would occur.

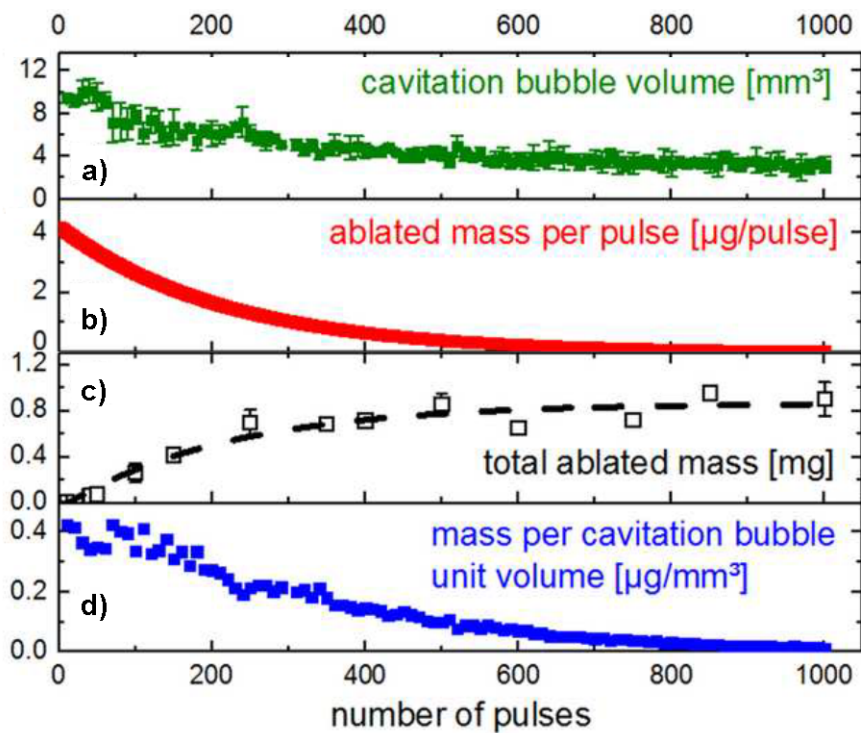


Figure 3.6: (a) Volume of the cavitation bubble; (b) ablated mass per pulse (ablation rate); (c) total ablation mass; (d) silver mass concentration per cavitation bubble volume (mass concentration).

Regarding the decrease in the volume of the bubble, note that laser-induced cavitation bubbles frequently are described using the Rayleigh-Plesset equation (RPE) [70], although it is not suitable for describing the collapse of the bubble or the rebound phases in PLAL. The interfacial tension of water and the

kinematic viscosity were introduced as adjustable parameters to improve the usability of the Rayleigh-Plesset equation in PLAL. Even though the Gilmore model introduced the compressibility of the liquid [73] and described PLAL-induced cavitation bubbles sufficiently well. From the data presented in Fig. 3.6a, b it was calculated the single-pulse ablated nanoparticle mass per unit volume of the cavitation bubble, which is equivalent to the mass concentration inside the bubble (Fig. 3.6d). Therefore, we assumed that most of the ablated mass initially was trapped inside the cavitation bubble. For a significant fraction of the ablated mass, this is a reasonable assumption because nanosecond PLAL structures with sizes between 3 and 100 nm have been identified inside the bubble before its final collapse, while no structures have been identified outside the bubble [79, 40]. In other works it was reported that the minimum detectable size with high time resolution inside the cavitation bubble was 3-5 nm, and, therefore, smaller particles, clusters, and atoms might enter the liquid phase without being detected even before the collapse of the cavitation bubble. Nevertheless, assuming complete confinement of the ablation mass inside the bubble, calculations that were done indicated that the mass concentration inside the cavitation bubble decreased exponentially as the number of pulses increased or the volume of the ablation crater increased, respectively (Fig. 3.6d).

The hemispherical cavitation bubbles that were induced on a non-irradiated target had an internal silver concentration of  $0.4 \mu\text{g}/\text{mm}^3$ . However, after the application of 1000 pulses and a crater as deep as  $900 \mu\text{m}$  and  $500 \mu\text{m}$  in diameter at the target surface (Fig. 3.5), the mass concentration decreased by an order of magnitude, i.e., down to  $0.01 \mu\text{g}/\text{mm}^3$ . However, this was inconsistent with the observation of increasing ablation mass per pulse and the volume of the bubble with increasing fluence [89, 90]. It is generally accepted that the ablated mass per pulse and the size of the cavitation bubble increase linearly with the laser fluence over a large range of fluences, but only above the respective threshold fluence [91]. The applied effective fluence in our work was in a regime in which the volume of the bubble is, indeed, a linear function of the fluence [86]. Hence, dividing both functions, i.e., the volume of the bubble and the ablated mass per pulse, is expected to result in either a new linear function or a constant value. To the contrary, it was found a clearly exponential relationship between the

mass concentration per bubble and the number of pulses. This clearly indicated that the mass concentration of the cavitation bubble was not correlated directly with the laser fluence, which means that changing the laser fluence provided no significant, direct control over the mass concentration of the silver inside the bubble. In turn, laser fluence is not the parameter that sets the mass concentration of the cavitation bubble, and it was more likely the confinement of the plasma inside the ablation crater and the alterations of the laser beam caused by partial refraction. Similar observations have not been reported because most studies have focused on the analysis of the cavitation bubble, on the bubble and the resulting, concentrated nanoparticles, or focusing exclusively on the induced microstructure of the target surface [91]. Yet, the mass concentration inside the extended cavitation was affected significantly by the presence of the pre-existing craters on the surface of the target.

The cavitation bubble that are anticipated to significantly add to the growth of nascent nanoparticles by (barrier-less) coagulation and coalescence, we expected to find further influence of the particle concentration inside the extended bubble on the rate of particle growth and the final size of the nanoparticles. Assuming monodispersed particles and barrier-less sintering of two particles (coalescence), the rate of change of the concentration of the particles would be  $dN/dt = -K_0N^2$ , where  $K_0$  is the coagulation coefficient, and  $N$  is the concentration of the particles [92]. The final size of a respective nanoparticle  $d(t)$  is given by  $d(t) = d_0(1 + N_0Kt)^{1/3}$ , where  $d_0$  and  $N_0$  are the initial particle size and the number concentration, respectively, at time zero [92].

### 3.4 Nanostructures synthesis and characterization

Nanoparticles were collected after several defined numbers of laser shots, stopping the liquid flow and using additional 10 laser pulses for ablation inside the crater that previously had been drilled. During this process no significant fragmentation of the nanoparticles occurs and the nanoclusters observed were formed during PLAL (see Fig. 3.7). Calculation of the mass concentrations of silver in the samples, done by measuring the ablated mass using confocal

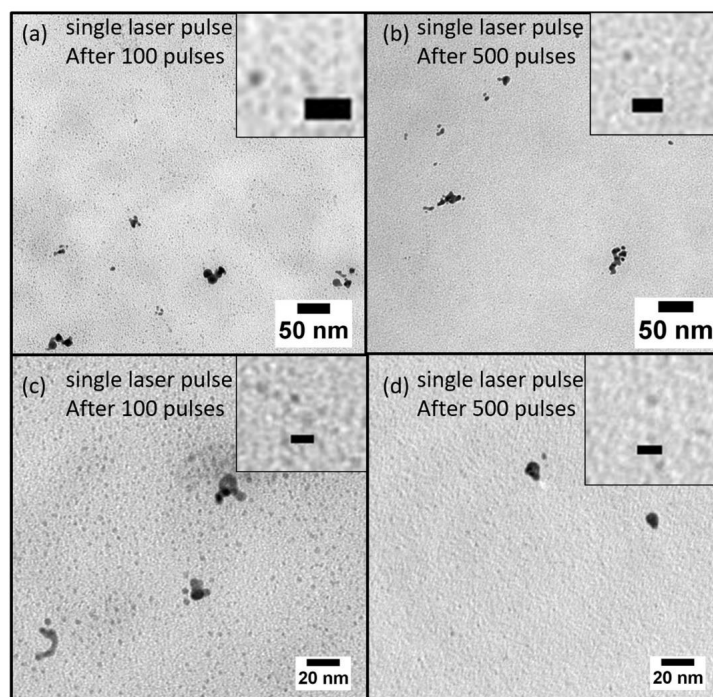


Figure 3.7: TEM images of gold nanoparticles and nanoclusters obtained by single laser pulses deposited in the craters drilled by 100 (a, c) and 500 (b, d) previous pulses, respectively, are presented.

3D microscopy, indicated that they were in the range of 0.8 to 80  $\mu\text{g}/\text{ml}$ . The target surfaces and laser percussion-drilled craters were characterized using a confocal 3D microscope that allowed the direct determination of the volume of the ablation crater, and, thereby, the ablated mass.

The estimated concentration of particles in the samples was extremely low (0.8-80  $\text{mg}/\text{l}$ ) because only 10 laser pulses (used for ablation in the craters) in a liquid volume of 0.5 ml were used for synthesis. The particle size distributions are summarized in Figure 3.8b for 10, 250, 500, and 1,000 previous laser pulses. The size distributions were similar because they have a large peak at 8 nm and a pronounced shoulder at about 11-13 nm, independent of the number of pulses. Regarding the same results, but weighted by particle mass, the size resolution of Analytic Ultracentrifuge (AUC), here used to obtain particles size distributions [93], allows the identification of five peaks in the size regime between 5 and 27

nm (Fig. 3.8a). All four mass-weighted, normalized particle size distributions were similar, with dominating peaks at 8 nm and four additional peaks around 12, 16, 20, and 24 nm. This is summarized in Figure 3.8e in which the colors of the data points are identical with the colors of the bars in the background of Fig. 3.8a, which mark the rough peak positions in the AUC size distributions.

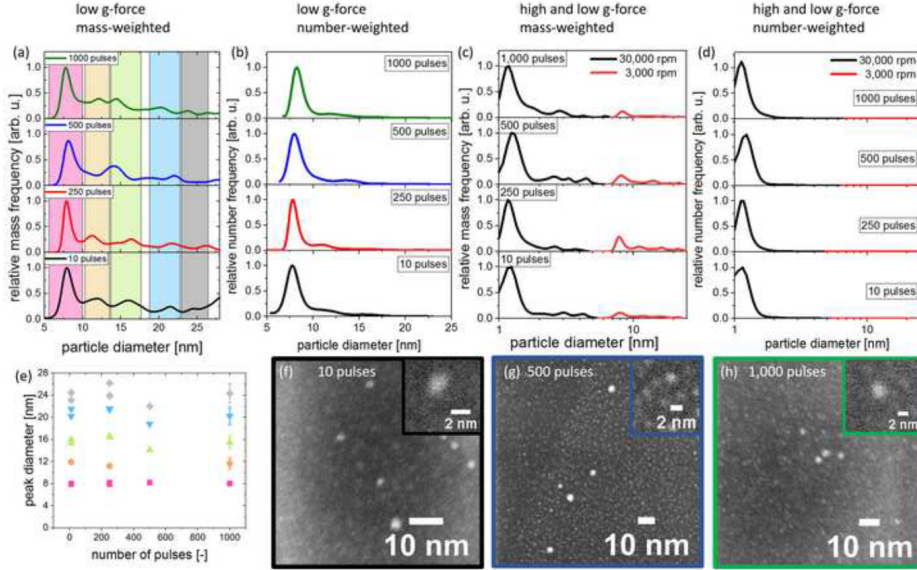


Figure 3.8: Analysis of the silver nanoparticles by AUC (a-c) and scanning HR-TEM (d,e). The images from scanning HR-TEM confirmed the presence of nanoclusters (10 pulses in (f), 500 pulses in (g), and 1000 pulses in (h)).

The dominance of the peak around 8 nm matched the results from in situ, small-angle X-ray scattering size determination inside the nanosecond PLAL-induced cavitation bubble [79]. Even though the peak at 12 nm was absent after 500 pulses, the distributions were quite similar in terms of the positions of the peaks. However, this did not account for the relative amounts of each particle fraction (i.e., peak integral). The additional normalized distributions shown in Figure 3.9b show that the peak integrals varied significantly from synthesis to synthesis, which makes it impossible to conclude on trends regarding possible higher shares of large secondary spheres induced by satellite microbubbles surrounding the cavitation bubbles induced in deep ablation craters. In turn, what is constant is the fact that we observed no effect of the volume of the extended



cavitation bubbles on particles  $\leq 25$  nm. No changes were identified in the aggregation behavior induced by fastened bubble dynamics or decreased silver mass concentration inside the bubble as a function of the number of preceding laser pulses. It was hypothesized two possible reasons for this, i.e., (1) aggregation might be statistically meaningless and (2) the collapse of the bubble might change the share of large particles that cannot be resolved by AUC, even at angular velocities as low as 3000 rpm. However, the main point is that a significant size alteration of the produced nanoparticles was not observed for changing the confinement conditions inside the bubbles. The particle production was rather defined by secondary processes, e.g., interaction with the plasma as well as laser fragmentation. The growth dynamics may have come to a halt at a time delay where the confinement due to the collapsing bubble sets in. This agrees with earlier findings that there is only minor growth observable during the lifetime of the bubble in an ideal (fresh substrate) condition.

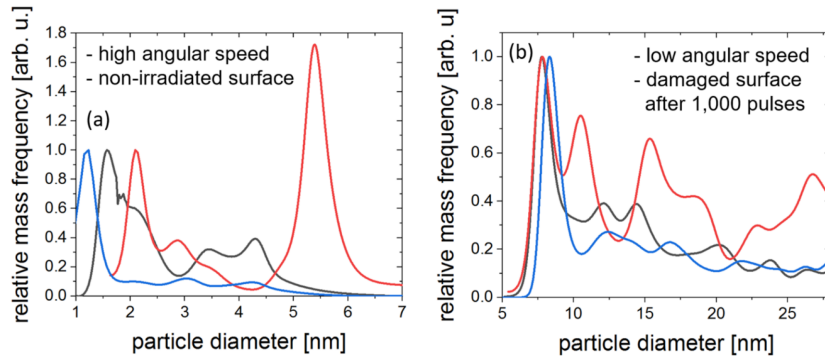


Figure 3.9: Ag particle size distributions of colloids, fabricated under identical conditions, measured by AUC at angular velocities of 30000 rpm to detect particles  $\ll 10$  nm (a) and 3000 rpm to detect particles  $> 5$  nm (b). All size distributions were normalized to the respective peak of minimum diameter

Such a correlation was not observed for the silver mass inside the extended cavitation bubble (Fig. 3.6d) and the size of primary particles, around 8 nm, (Fig. 3.8 c,e). Obviously, the primary particles were pre-defined even before the evolution of the cavitation bubble, in accordance with recent theoretical simulations [94]. These results are supported by a study by Dell’Agljo et al. in

which PLAL was performed under high pressure [95]. Although the maximum size and the lifetime of the bubble were decreased by increasing pressure, no influence on the final particle size distribution was identified. The conclusion is that the mass concentration inside the extended bubble was not linked in a simple way to the initial mass concentration on a sub-microsecond time scale. Performing AUC at the high angular velocity of 30000 rpm (Figs. 3.8c, d) indicated that there was a dominant particle size fraction below 3 nm. Such small nanoparticles are referred to as nanoclusters because they have different physical properties than ordinary nanoparticles, such as the lack of surface plasmon resonance and increased fluorescence [96]. The presence of nanoclusters was verified by the scanning HR-TEM images presented in Fig. 3.8f-h. Such ultra-small clusters have been reported as products of intensive laser fragmentation but only 10 pulses were used. Similar silver clusters were observed earlier during a laser fragmentation process using the second harmonic of an Nd:YAG laser system [97].

On the overall, the presence of nanoclusters during nanosecond PLAL, in the absence of laser fragmentation in liquids (LFL), has important implications for the particle-formation mechanism involved in and the experimental routines of PLAL. Since nanoclusters obviously are the dominant species that initially form during PLAL and since the peak positions of the secondary large spheres are unaffected by the presence and depth of a crater, it's possible to conclude that:

1. particle growth by ripening and coalescence has a major role in the definition of the colloids after the final collapse of the cavitation bubble, which is even more significant than the shape, volume, and total lifetime of the bubble;
2. during continuous PLAL, even when applying a scanning strategy the advancing surface microstructure induced on the target strongly affects the cavitation bubble, but, interestingly, it does not affect the resulting nanoparticles; hence, it is further confirmed that continuous, liquid-flow PLAL is a stable synthesis process;

3. manipulating the particle size is not limited to the early stage of ablation, e.g., inside the cavitation bubble, but expands to the minutes-to-days regime.

Regarding the satellite bubbles that were observed (Fig. 3.3a), alternative explanations are (1) the (partially) ablated walls of the crater as shown by the non-linearly increasing crater aspect ratio  $L/D$  (Fig. 3.5a); (2) hydrodynamic effects induced by additional confinement of the cavitation bubble inside the craters, which led to higher acceleration of parts of the cavitation bubble. The latter hypothesis is supported by the frame recorded after 700 shots in Figure 3.3, in which a tail is visible on the top of the cavitation bubble; and (3) droplet jetting may have benefited from the geometry of the crater or sub-surface voids created by the preceding pulses [98].

The combined effects of plasma confinement, alteration of the cavitation bubble, and mass concentration per unit volume of the cavitation bubble could raise expectations for changes in the sizes of the nanoparticles. Surprisingly, the detailed analysis of the properties of the particles by means of analytical ultracentrifugation and scanning HR-TEM did not reveal systematic changes, either as a function of the depth of the crater or the shape of the cavitation bubble. Hence, the effect of altering the volume or shape of the cavitation bubble on particle size was found to be minor or even non-existent. Furthermore, long-time nanocluster-induced growth processes and primary plasma/ablation effects seem to be more important for the final colloids obtained by PLAL as the shape change of the bubble. Nevertheless particle yield is drastically reduced by the corrugated substrate.

## Chapter 4

# Noble metal nanoparticles for SERS applications

### 4.1 Surface Enhanced Raman Spectroscopy substrates for therapeutic drug monitoring

In this chapter are illustrated the context and activities that have been carried out to prepare Ag and Au SERS substrates for clinical applications in therapeutic drug monitoring (TDM) with focus on anti-epileptic and anti-Parkinson drugs.

TDM is a clinical practice to determine the drug concentration in the blood of patients. TDM is based on the idea that the concentration of a drug in the plasma, or in the blood, reflects the concentration of the drug at the target site better than the given dose [99]. Thus, monitoring the drug concentration in patients allows for adjusting the dose in prolonged therapies and helps understanding the patient dependent pharmaco-kinetics and pharmaco-dynamics. Therefore, it is relevant for medical doctors to monitor the concentration level of narrow therapeutic index drugs. This allows to associate the clinical conditions of the patient to the drug posology, thus ensuring the efficacy of the treatment for the minimal drug concentration, which also avoids adverse, or toxic effects.

The standard techniques currently used in clinical laboratories for TDM are

the immunoassay and chromatographic techniques (High Performance Liquid Chromatography, HPLC), often associated with mass spectrometry (i.e., HPLC-MS). Both techniques are highly sensitive and reliable, but unfortunately the associated costs are high, the waiting time is long and sizeable blood withdrawal (a few milliliters) is required.

Recently, in TDM literature a complementary approach to the measurements of drug concentration has emerged which considers SERS as the analytical technique.

Among the drugs, the detection of Perampanel, a widely used drug to treat epilepsy, is highly significant to improve the quality of life of patients, mainly in developing countries. The same considerations on life quality improvement hold concerning Apomorphine (APO) for Parkinson's disease at an advanced stage. In this scenery, the straightforward use of SERS with gold and silver colloids, even if very sensitive to qualitatively detect analytes, is not acceptable because of its strong limitations in quantitative detection, mainly arising from uncontrolled colloid aggregation. This is reflected by the lack of scientific literature on this specific subject [100].

The intrinsic limitation to Raman spectroscopy is the signal weakness, i.e. the small number of inelastically scattered photons with respect to the overwhelming majority of elastically scattered photons that originate the Rayleigh peak. Although in resonant conditions the efficiency of the Raman process increases significantly, not always laser sources suitable to exploit resonance conditions with the system of interest are available. Thus, since the discovery of SERS effect at the beginning of the 70s of XX Century many efforts were devoted to use either spontaneously, or artificially corrugated surfaces of selected metals to significantly extend the range of application of the technique. In particular the study of an analyte dissolved in a highly diluted solution is a typical scenery suitable to highlight the characteristics of the SERS technique. To get the Raman signal intensification it is required that the analyte molecule is in close proximity to a roughened metallic surface where a surface plasmon (SP) can resonantly be excited at the energy of the probe photon beam [20]. We recall that if a semi-infinite electron gas is confined by a plane surface, solving the Laplace equation for the admissible fluctuations of the charge density, periodic

plasma oscillations are predicted in the surface plane, whose amplitude decays exponentially towards the bulk of the electron gas. The quantum of oscillation is called surface plasmon. Once we use EM periodic boundary conditions, so that the tangential component of the EM field and the normal component of the displacement are both constant across the surface-vacuum interface and we take into account the dispersion relation for the dielectric constant of the electron gas, we obtain the relation between the frequency of a SP,  $\omega_S$  and that of a volume plasmon  $\omega_p$ :

$$\omega_S^2 = 1/2\omega_p^2 \quad (4.1.1)$$

The relative intensities of volume and surface plasmon excitations depend on the incidence angle, the energy and the polarization of the exciting EM radiation. When the typical size of the metallic structure downscales to the nanometer range (5-50 nm) the relative weight of surface atoms becomes relevant with respect to that of volume atoms and we observe a displacement of the experimentally measured plasmon wavelength to higher values.

Nanoparticles (NPs) of silver and gold show SP absorption peaks around 410 and 520 nm, respectively, thus in the visible range. Such SPs originate from the plasma oscillations of conduction electrons at the NP surface. It is thus possible to excite electron oscillations with some of the most commonly used laser sources operating in the visible range. For this reason, both nanostructured noble metals are very popular as SERS substrates [101]. Compared to other metals nanostructured Ag and Au show the most relevant intensification effects of Raman signals. In many cases for both metals also the chemical intensification mechanism has been observed. The latter is ascribed to resonance effects within the target molecule and charge transfer effects between molecular orbitals and the conduction band of the noble metal surface [102].

A perspective direction towards the synthesis of noble metal based sensors with SP wavelength adjusted ad hoc between the two extremes belonging to isolated NPs either pure Ag (around 400 nm) or pure Au (around 520 nm) is provided by the use of Ag and Au colloidal solutions produced by pulsed laser ablation in a stationary liquid.

## 4.2 Ag and Au nanoparticles: synthesis and characterization

A good basis for the enhancement of SERS signals is a fine control of NP size, shape, spatial density and their distribution. In the last few years, different preparation techniques have been used to prepare gold (Au) and silver (Ag) nanocolloids. However, wet chemical synthesis methods (i.e. precipitation and sol-gel techniques) leave residual reagents which, unfortunately, cause the deactivation of NP surfaces. In contrast, pulsed laser ablation in liquid (PLAL) that produces ligand-free [35], high purity NPs with superior conjugation efficiency [103, 104] that are key parameter to enhance the Raman scattering signal. Nevertheless, with this synthesis method, it is difficult to achieve the large amounts of NPs required for industrial applications, in a short time, keeping unaltered the morphological properties. As described in the previous chapters, being the ablation phenomenon in liquid a combination of different, probably competing, mechanisms in the laser-target-liquid system, it is of paramount importance to determine the appropriate ablation parameters to obtain NPs with tailored size distributions and concentration.

Then, it was investigated the morphological and optical properties of ligand-free Ag and Au nanoparticles (NPs) synthesized by nanosecond (ns) and picosecond (ps) laser ablation. First, the effects of the focusing conditions on the ablated spot diameter which, in turn, determines the operative fluence were investigated. Established the optimal focusing conditions, the effects of the pulsed laser fluence was examined, in order to obtain an higher NPs productivity.

For ns-PLAL, we analysed the irradiation geometry, finding optimal focusing conditions to maximize the ablation rate. The 532 nm second harmonic emission wavelength of a Nd:YAG laser with a 6 mm beam radius delivering pulses of 5 ns length and operating at a repetition rate of 10 Hz, was used for the ablation experiments (see scheme in Fig. A.8 in Appendix A).

The effects of the water level above the target and the lens positions on the ablated spot diameter which, in turn, determines the operative fluence was studied. To discern the appropriate conditions (in terms of lens position and water level) the ablation processes at the fixed pulse laser energy of 20 mJ/pulse

and for an ablation time of 20 min was carried out. The focal position that allows to have the maximum amount of the Au nanoparticles was chosen. Now, keeping fixed these ablation parameters, the ablation processes were carried out varying the pulse laser energy between 6 mJ/pulse and 150 mJ/pulse. The optical characteristics (plasmon resonance) of the colloids and the Au concentrations vs the laser pulse energy was evaluated [105].

As the laser pulse energy increases:

- the absorption peak slight shifts to the longer wavelengths;
- the overall optical absorbance decreases;
- a new contribution to the absorption at 750 nm is observed, which is indicative of a clustering process;
- Au nanoparticles concentration initially increases up to the value of  $5.5 \cdot 10^{-4}$  M (in correspondence of the laser energy of 50 mJ) and then, progressively, decreases.

The high pressure and temperature conditions established at the interface between the expanding plasma and the confining liquid may favour the fragmentation of the existing nanoparticles that will rearrange in clusters [106, 107, 26]. Thus, the observed decrease of the nanoparticles amount, deduced from optical absorption, simply reflects this rearrangement.

For noble metals and ceramics, more recent systematic investigations compare the morphology, size, size distribution, production yield, absorption spectra of NPs produced by ns-, ps- and fs-PLAL at different laser wavelengths [108]. Compared to ns lasers, high repetition rate ps lasers are advantageous whenever the total thermal load produced by laser irradiation can be redistributed over a larger area [109]. When laser ablation is carried out in a polar liquid (typically, water), surface-charged NPs are produced. These are solvated by a shell of dipolar molecules (e.g., water) and do not agglomerate because of the Coulomb repulsion generated by their surface charge [110].

Fig. 4.1 representative crater shapes produced by a ps laser ablation of an Ag target in water, with a laser power of 4.5 W for a fixed number of pulses of 500000 (see Appendix for more details about the PLAL setup). SEM images



show that ps laser pulses produce on a target, immersed in the liquid medium, craters whose width slightly changes as a function of the scanner objective-target distance  $d$ .

Moreover, surrounding the edge of the crater, an accumulation of removed material can be envisaged. This is more evident when the objective-target distance  $d$  is fixed at 20 mm and 30 mm, respectively (Fig. 4.1a,c,e). This distance represents the optimal focusing condition in terms of ablation efficiency was established by looking at optical properties (see Fig. 4.1b,d,f). These observations can be explained taking into account that the removal of mass from the irradiated zone can occur by both thermal and nonthermal mechanisms. The incident laser radiation on the metal creates a large population of highly excited nonequilibrium electrons in a region near the target surface. This electronic excitation can lead to bond breaking of the sample material or "desorption" and, subsequently, can cause atomic-size particulate to be ejected from the surface. For a thermal mechanism, the electron energy is redistributed through lattice vibrations and consequently, heat is conducted into the sample. Such heat besides melting the sample can bring its local temperature to the vaporization. Mass removal in the form of micron-sized droplets can also result from hydrodynamic instability of the molten liquid layer. The evaporating vapor can exert a recoil pressure on the melted surface, and molten mass can be pushed radially outward from the irradiated zone [111]. In focusing conditions, the crater has sharp borders and matches the laser spot. This occurs mainly with ultrafast localized laser energy transfer (the machining process occurs via non-linear absorption, enabled by the high intensity in the focus of radiation, resulting in the direct evaporation of the material, in principle, without activating any melting mechanism) when ablation is dominated by direct photoionization processes, thus by locally induced space-charge separation fields and by electron-ion collisions. Thus, a first control over the optical properties of Ag and Au NPs must be carried out modulating the beam intensity profile at the target (see Fig. 4.1g). The colloids, produced with laser power of 4.5 W and irradiation time of 10 min in the three selected focusing conditions show that:

- the Surface Plasmon Resonance (SPR) peak position remains almost unchanged;

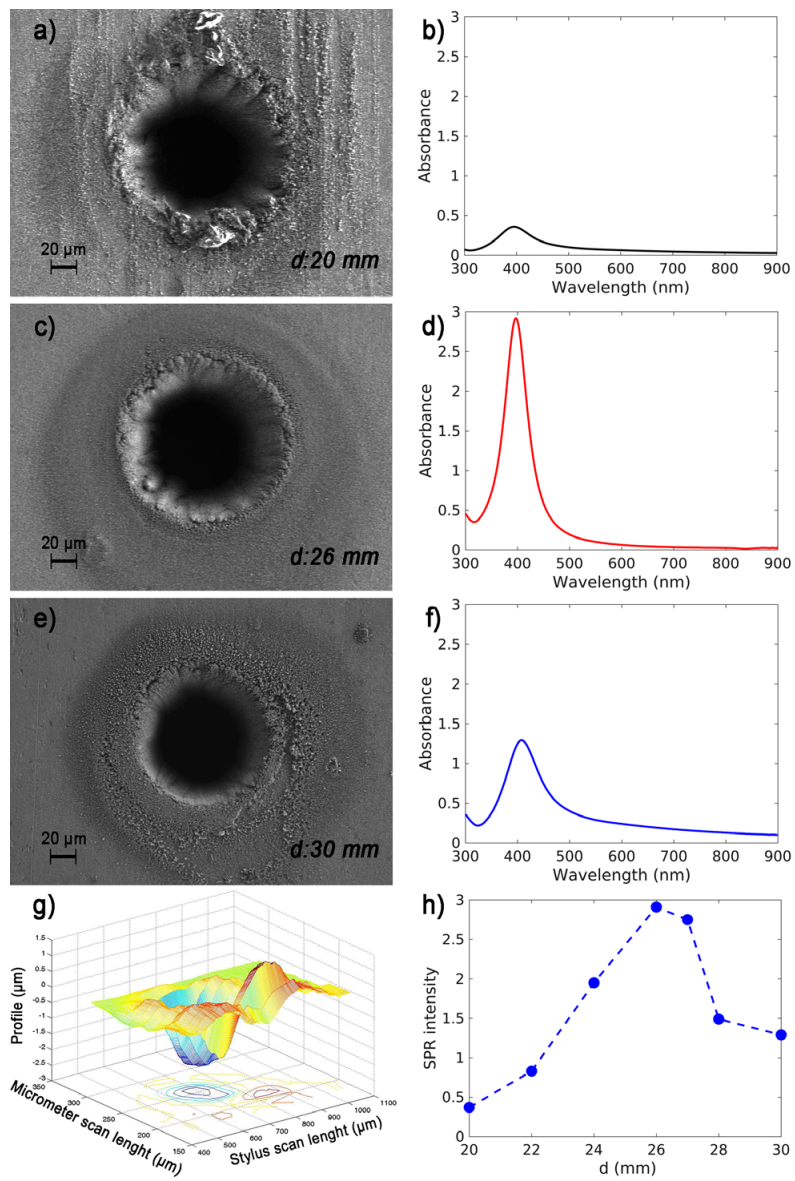


Figure 4.1: SEM images of craters produced by ps laser ablation of the Ag target at a laser power of 4.5 W for 500000 pulses (a,c,e), varying the objective-target distance  $d$ . The optical absorbance spectra of Ag colloids (b,d,f); Crater profile for  $d=26$  mm (g) and effect of objective-target distance  $d$  on SPR intensity (i.e. on NP productivity) (h). The dashed line is a guide for the eyes.

- its intensity changes as a function of  $d$  (see Fig. 4.1b, d, f).

On the overall, it emerges that the higher Ag NP amount was obtained for  $d$  value of 26 mm. Similar results were obtained using the Au target (not shown). The NP productivity of ps pulse laser ablation mainly depends on the pulse energy or fluence and on the pulse repetition rate used in processing. Both these factors are limited by physical processes. For a given pulse energy the ablation rate can be increased by using a higher average power and a higher frequency. The increase in frequency can determine shielding effect caused by the presence of plasma or cavitation bubbles. In this case, the laser repetition frequency was not examined as a parameter limiting the NP productivity.

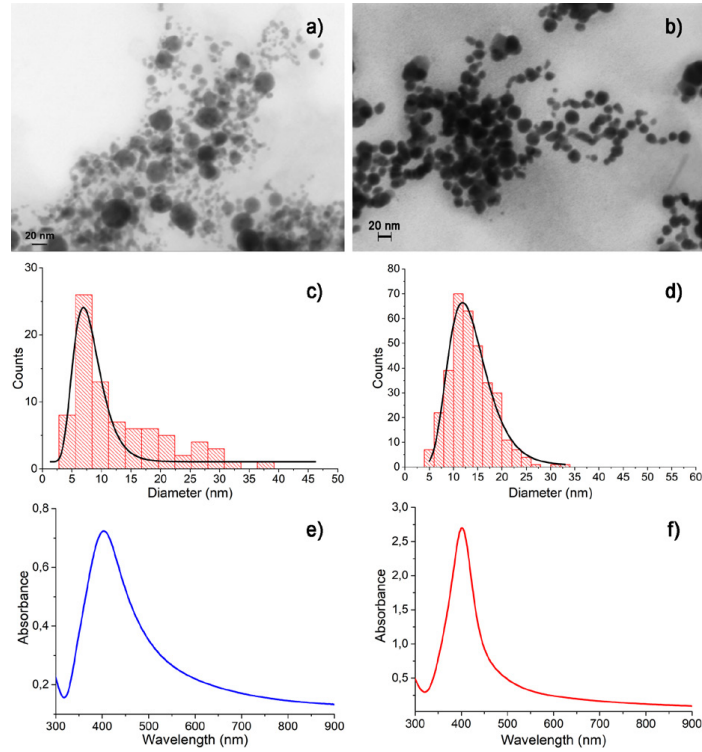


Figure 4.2: STEM images, averaged size distribution and optical absorbance spectra of Ag colloids prepared at the laser fluence of  $0.5 \text{ J/cm}^2$  (a,c,e) and  $1.5 \text{ J/cm}^2$  (b,d,f), respectively.

Keeping fixed the objective-target distance  $d$  at 26 mm, for which we found the highest NP productivity, we investigated the effects of the laser fluence on

the optical/morphological properties of the colloids. In Fig. 4.2 are shown STEM images and optical absorbance spectra of Ag colloids prepared at the laser fluence of 0.5 and 1.5 J/cm<sup>2</sup>, respectively. In the sample prepared at 0.5 J/cm<sup>2</sup>, nearly spherical NPs with a diameter of about 8 nm are observed (see Fig. 4.2c). Few NPs larger than 40 nm are also evident. Increasing the laser fluence (1.5 J/cm<sup>2</sup>) the spherical NPs, whose size is of about 15 nm, often agglomerate and overlap (see Fig. 4.2d). We show in Fig. 4.2e-f the trend of the UV-Vis absorption spectra as a function of the different morphologies. We observe that the SPR peak intensity increases and the Full Width at Half Maximum (FWHM) decreases, when we increase the laser fluence, keeping fixed all other deposition parameters. In Fig. 4.3 are shown a STEM representative

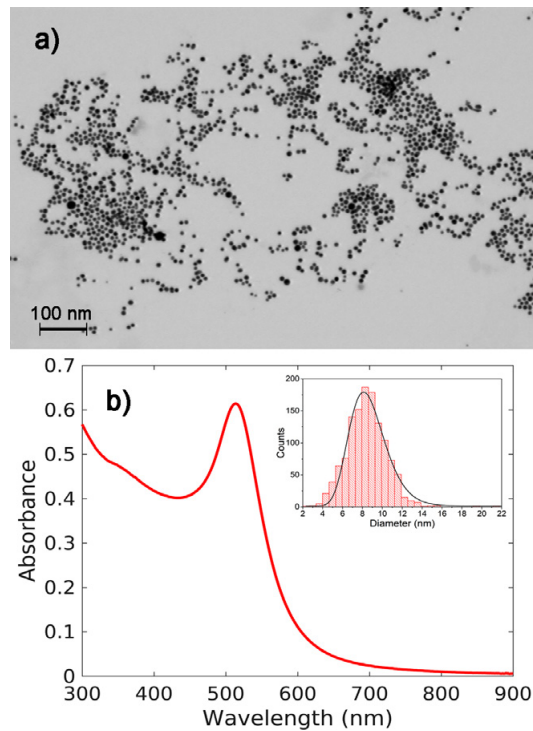


Figure 4.3: Representative STEM image (a) and optical absorbance spectrum (b) of Au colloids prepared at the laser fluence of 1.5 J/cm<sup>2</sup>. In the inset the NP colloid size distribution.

image, the size distribution and the optical absorbance spectrum of Au colloids prepared at the laser fluence of 1.5 J/cm<sup>2</sup>. A high NP productivity as well as

a uniform and narrow size distribution (centred around 9 nm) emerges from STEM image analysis. These evidences are confirmed by the relatively narrow SPR lineshape centred at about 505 nm.

Fig. 4.4a,c show the optical absorbance spectra of the films obtained spraying Ag and Au colloids on glass substrates. A red-shift and a broadening of the width of the SPR peak is observed, mainly for Ag sample. This behavior is ascribed to a clustering process occurring during the transfer of colloids onto the substrates. In fact, different surface morphologies, from isolated nearly spherical NPs, detected by STEM images, to larger islands (agglomerates) with smooth edges were observed by means of SEM on the inhomogeneous films sprayed on the support (see Fig. 4.4b, d). We tested the sprayed films for their SERS activity.

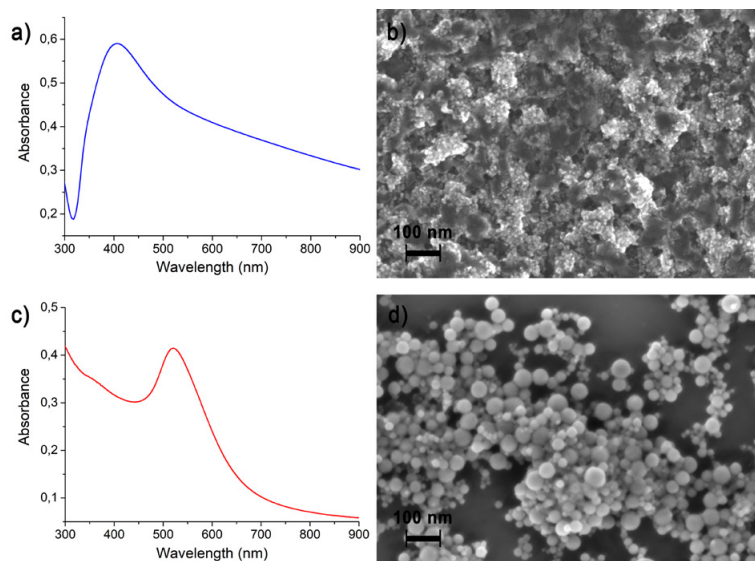


Figure 4.4: UV-vis optical absorbance spectra (a,c) and SEM images (b,d) of the films obtained spraying Ag and Au colloids on a Si support (a,b).

In Fig. 4.5 are shown SERS spectra measured from the Ag and Au films on silicon after exposition to an aqueous solution of CV (concentration  $8.9 \times 10^{-6}$  M). For both films we observe well resolved SERS spectra, showing all expected features of CV, i.e., the main peaks located at about 420, 441, 725,

780, 915, 1173, 1392, 1587, 1619  $\text{cm}^{-1}$  [112].

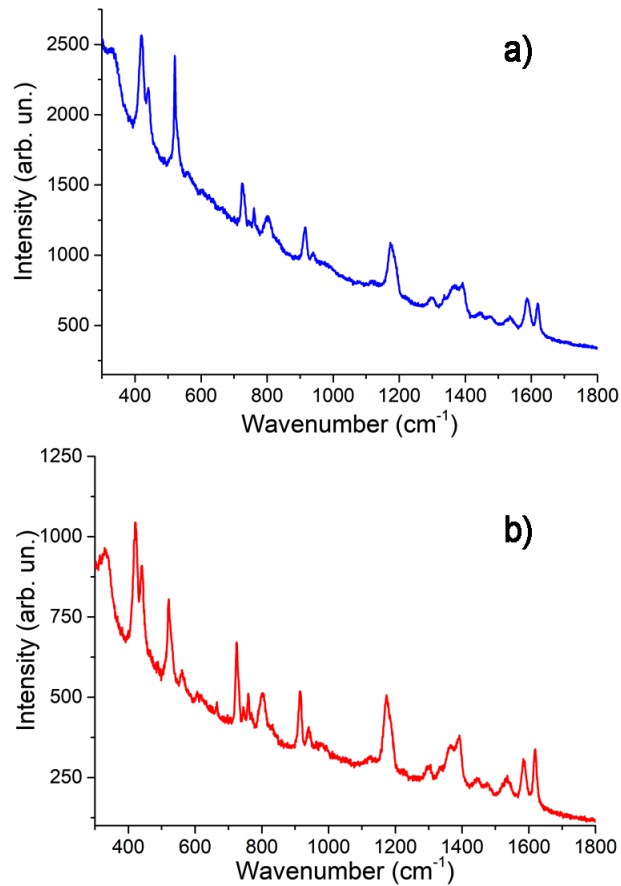


Figure 4.5: Raman spectra of crystal violet in  $\text{H}_2\text{O}$  at the concentration  $8.9 \times 10^{-6}$  M adsorbed onto the surface of the Ag (a) and Au (b) samples, respectively. Exciting line wavelength: 785 nm.

### 4.3 SERS sensing of perampanel with nanostructured arrays of Au particles

Au colloids were prepared by pulsed laser ablation using the 532 nm radiation provided by the second harmonic of a Nd:YAG source with a repetition rate of 10 Hz and pulse width of 5 ns as well as by an ultra-fast Nd:YVO<sub>4</sub> source with

	Nanosecond	Picosecond
$y_0$	$1.3 \pm 0.8$	$-2.1 \pm 5$
$x_c$	$24.8 \pm 0.4$	$8.4 \pm 0.1$
$w$	$0.21 \pm 0.02$	$0.29 \pm 0.02$
$A$	$313 \pm 22$	$1077 \pm 53$
$R^2$	0.95387	0.95683

Table 4.1: Fit parameter for the LogNormal function:

$$y = y_0 + \frac{A}{\sqrt{2\pi wx}} \exp^{-\frac{(\ln(x/x_c))^2}{2w^2}}$$

repetition rate of 100 kHz and pulse duration of 6 ps. The pulsed, high-power laser beam impacts onto a rod-shaped Au target (99.99% purity) immersed in demineralized water, as showed in Fig. A.8 in the Appendix A. The optimized ablation times, ensuring high NP productivity were 20 min (ns-PLAL) and 5 min (ps-PLAL) as previously determined and discussed. For both conditions, the laser fluence was  $F = 1.5 \text{ J/cm}^2$ .

Au NPs with narrow size distribution using both ns and ps laser pulses were obtained. The latter allows for a higher NP productivity, as indicated by the SPR profile (Figure 4.6e, red line) which is more intense and slightly narrower than that collected from NPs produced by ns pulses. Compared with ns-NPs, a narrowing of the SPR peak for the ps-NPs as well as an increase in the background is observed, while the SPR position is practically unaffected (Figure 4.6e). The narrowing depends on the presence of small, isolated NPs, while the background increase is due to a larger NP yield. Both features agree with STEM images (Figure 4.6a,b) and the size histograms in Figure 4.6c,d (see Table 4.3 for details on the fitting procedure of the size distribution).

The laser fluence and wavelength were kept fixed, so that we could better compare NP sizes and production yields between ns and ps synthesis conditions with respect to previous studies, assuming that NP size is mostly affected by the laser wavelength, whereas production yield is mostly affected by the laser fluence [108]. Results can be interpreted by considering that laser ablation in a stationary liquid involves the simultaneous production of NPs by ablation of

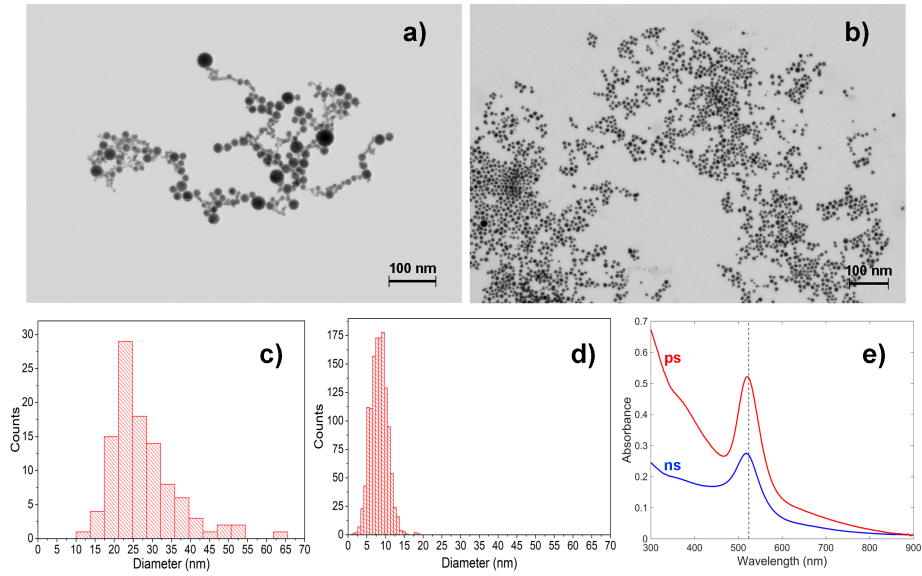


Figure 4.6: STEM image (a) and size distribution (c) of Au NPs prepared at  $F = 1.5 \text{ J/cm}^2$  for  $t = 20$  minutes (ns irradiations). STEM image (b) and size distribution (d) of Au NPs prepared at  $F = 1.5 \text{ J/cm}^2$  for  $t = 5$  minutes (ps irradiations). Optical properties of the colloids (e). Au content in colloids prepared by ps-PLAL and ns-PLAL (determined by GF-AAS, see Section ), is  $312.0 \pm 2.5$  and  $174.5 \pm 1.8 \mu\text{g/ml}$ , respectively.

the target material and the fragmentation/assembling of dispersed NPs by continuous irradiation of the already synthesized particles. In this respect, pulse duration is a relevant parameter for NP generation [113]. By changing the pulse duration from ns to ps, the relevance of melting and thermal evaporation among ablation mechanisms significantly decreases. The shorter the pulse duration, the more efficient the ablation process that involves a nearly instantaneous evaporation with a minimized heat affected zone [114], thus resulting in a shorter time to produce the colloids. Furthermore, primary plasma shielding that is detrimental to ablation efficiency is much reduced with ps laser pulses, as compared to ns pulses [115].

X-ray diffraction data in Figure 4.7 show that the Au NPs prepared by ps-PLAL are crystalline, as confirmed by the (111), (200), (220) and (311) Bragg reflections of fcc Au (see card JCPDS 04-0784). (111) texture is present. The



XRD features are broader than those in Au nanocrystals [116]. Most likely, this is due to a combination of the small size of such particles (see Figure 4.6d) with the associated residual stresses.

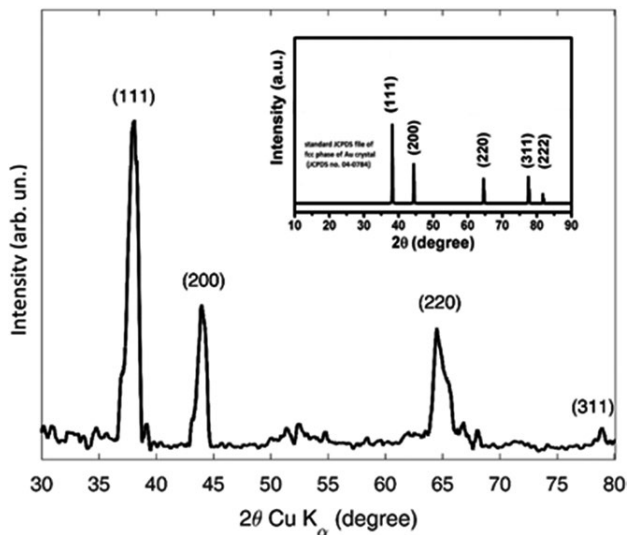


Figure 4.7: XRD pattern of Au NPs prepared by ps-PLAL in demineralized water. A reference XRD from the literature (card JCPDS 04-0784) is shown.

Dynamic light scattering (DLS) allows to estimate the changes in size and size distribution of the particles. DLS data systematically correlate with the changes in the SPR lineshapes observed by UV-Vis spectroscopy. Au colloids produced by both ns- and ps-PLAL were stored for 3 months at atmospheric conditions; thereafter, their optical properties were tested by UV-Vis spectroscopy and DLS, and compared to those of freshly prepared colloids. In Fig. 4.8 the optical characterization of colloids prepared by ns-PLAL are shown. The results for colloids produced by ps-PLAL are very similar and are not discussed. After 3 months of storage in dark, at ordinary laboratory conditions, we observed no colour change of the colloids and no evidence of colloid instability. The intensity decrease with time of the SPR (Figure 4.8a) indicates gravity-induced sedimentation. Accordingly, changes in DLS (Figure 4.8b) occur at high delay times that correspond to larger NPs that are more sensitive to gravity. The estimated average size of NPs deduced from DLS reduces from 85 nm (fresh NPs) to about 45 nm (NPs stored for 3 months). Particle sedimentation induces a decrease

in the optical density of the colloid and a corresponding change in its refractive index. The evident discrepancy between NP size estimated by DLS and STEM data is due to detection limits of DLS in the presence of poly-disperse colloids. Sample polydispersity can affect DLS data because the fraction of non-precipitated large NPs can shield the smaller ones, thus altering the true NP size population [117].

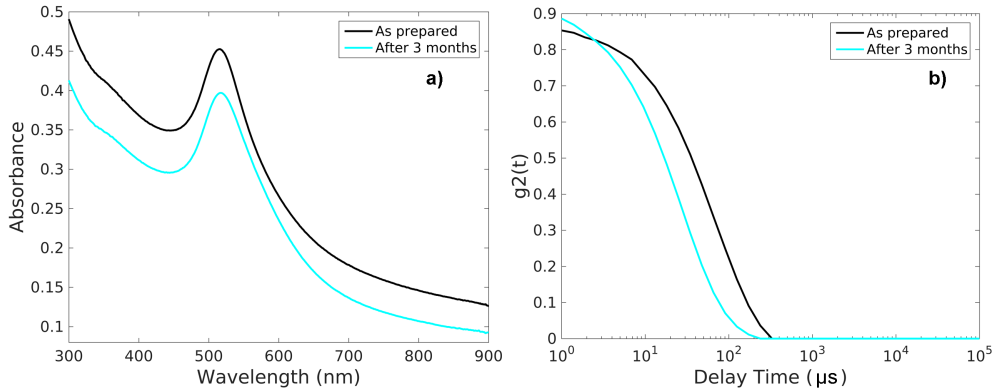


Figure 4.8: (a) UV-Vis optical absorption spectra and (b) DLS correlation curves from Au NPs synthesized by ns-PLAL. Black line: freshly prepared sample; blue line: sample aged 3 months. In the inset, the STEM micrograph of the aged NPs

A fraction of the Au colloids produced by ps-PLAL was ultrasonically sprayed on glass or on (100) Si supports to obtain thin films suitable for SERS measurements. Before performing the SERS tests, we characterized with UV-Vis spectroscopy the films supported on glass, and we examined by SEM the morphologies of the films supported on Si (Figure 4.9). Comparing the upper absorbance spectrum in Figure 4.6e (colloids prepared by ps-PLAL) with the homologous spectrum in the inset of Figure 4.9, we see that the SPR red shifted from 517 nm (Figure 4.6e) to 522 nm (Figure 4.9). The FWHM changed from 47 nm (Figure 4.6e) to 79 nm (Figure 4.9). Such redshift and broadening of the SPR is ascribed to the clustering of the colloids when they are transferred on the glass support. Indeed, by SEM, we observe surface morphologies on the films sprayed on Si (Figure 4.9) which differs from the colloid morphologies observed by STEM (Figure 4.6b): The isolated, small spherical NPs detected by STEM

evolve into larger agglomerates consisting of mostly spherical particles observed by SEM (Figure 4.9). Such an agglomeration process induced by spraying is actually a desirable feature when producing substrates for SERS considering that it fosters the formation of hot-spots [118].

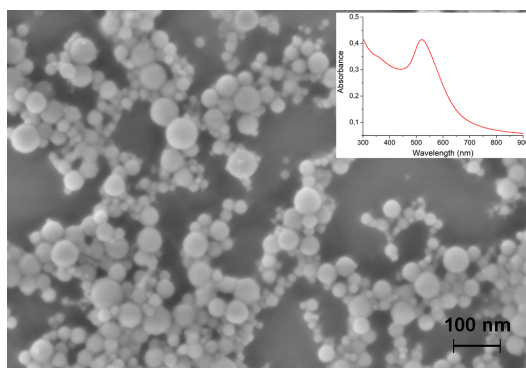


Figure 4.9: SEM image of a representative film obtained ultrasonically spraying on a Si support Au colloids made by ps-PLAL. The associated UV-Vis optical absorbance spectrum is reported in the inset

Before addressing the SERS experiments, we measured as a reference the FT-Raman spectrum of a sample consisting of a 6 mg pharmaceutical tablet of Fycompa, denuded of its protective external coating. In such a sample (namely, the core of the tablet), the API perampanel is mixed with the listed excipients (Figure 4.10). As shown in Figure 4.10, among all the declared excipients of Fycompa, the FT-Raman spectrum of lactose monohydrate closely matches the measured spectrum of the sample. The well-resolved Raman features (a-d), which by comparison are not due to lactose monohydrate, are assigned to the API, as the most intense Raman peaks of the other excipients cannot be individually observed and just contribute to the background signal. Thus, based on the qualitative assessment of the FT-Raman data, we conclude that the most abundant excipient in the sample is lactose monohydrate that fits the declared composition of the pharmaceutical formulation ([http://www.ema.europa.eu/docs/it\\_IT/document\\_library/EPAR\\_Product\\_Information/human/002434/WC500130815.pdf](http://www.ema.europa.eu/docs/it_IT/document_library/EPAR_Product_Information/human/002434/WC500130815.pdf)).

The FT-Raman spectrum of the Fycompa sample shows four distinct fea-

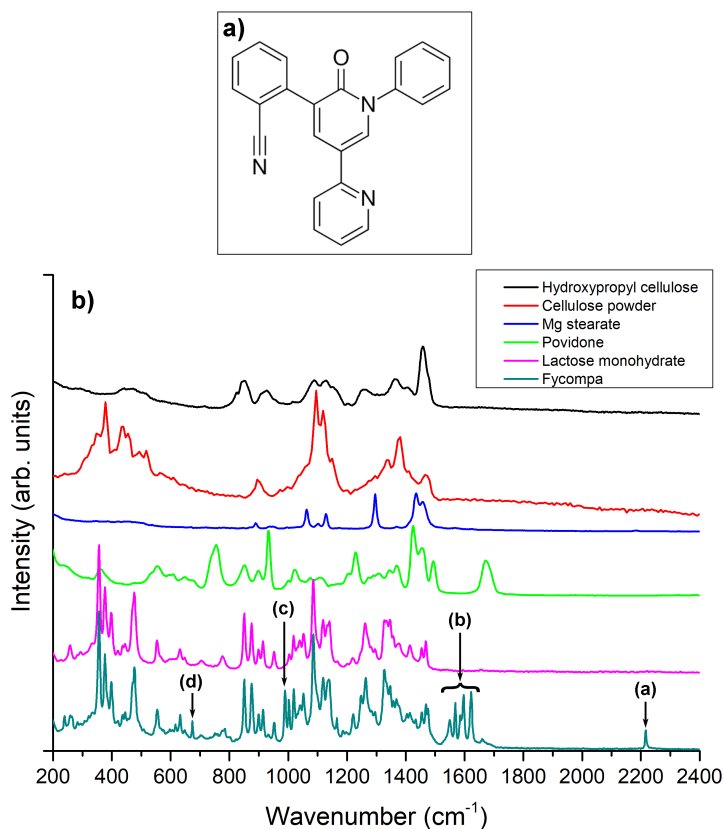


Figure 4.10: (a) Chemical structure of perampanel; (b) FT-Raman spectrum of the core of a Fycompa 6 mg commercial tablet compared with representative FT-Raman spectra of all the excipients declared in the pharmaceutical formulation ([http://www.ema.europa.eu/docs/it\\_IT/document\\_library/EPAR\\_Product\\_Information/human/002434/WC500130815.pdf](http://www.ema.europa.eu/docs/it_IT/document_library/EPAR_Product_Information/human/002434/WC500130815.pdf)). The labels (a-d) mark the Raman features assigned to the active pharmaceutical ingredient, perampanel. See text for details.

tures (a-d) that can be attributed with confidence to the API, as they fall in wavenumber ranges where the excipients do not show any strong Raman line. The position of the observed Raman peaks is also consistent with the chemical structure of perampanel (Figure 4.10a). Line (a) at 2216 cm<sup>-1</sup> is assigned to the stretching of the CN bond. The manifold of Raman lines (b) (1622, 1597, 1585, 1569, 1550 cm<sup>-1</sup>) is assigned to aromatic ring stretching modes, and the line (c) at 989 cm<sup>-1</sup> can be assigned to the breathing of one of the rings of perampanel.

Finally, the position of line (d) at  $674\text{ cm}^{-1}$  is consistent with an aromatic ring deformation mode.

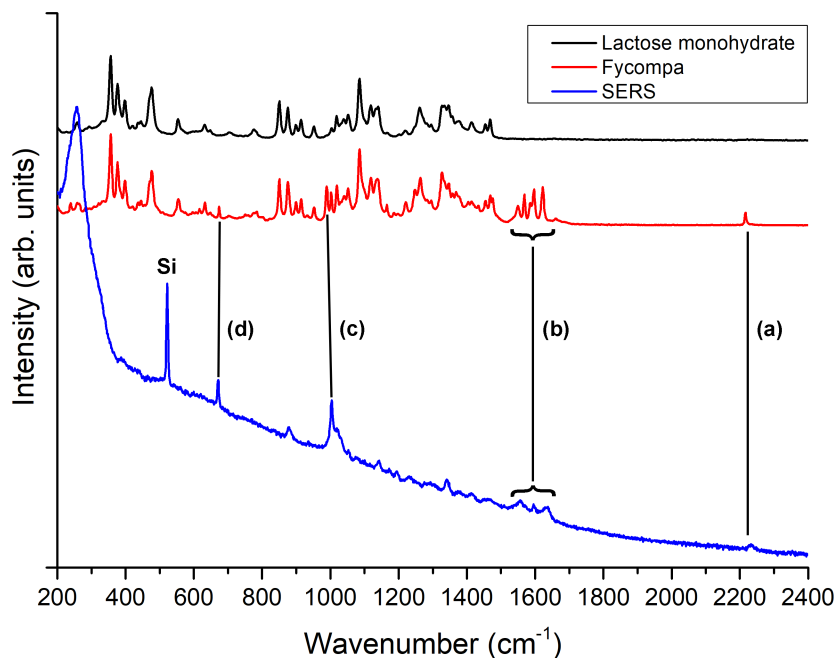


Figure 4.11: SERS spectrum of the methanol extract of perampanel (estimated concentration  $< 1.4 \times 10^{-3}\text{ M}$ ; 785 nm excitation wavelength - see Experimental section for details on sample preparation) compared with the FT-Raman spectrum of the Fycompa sample, and with the FT-Raman spectrum of the main excipient (lactose monohydrate). FT-Raman spectra were collected with 1064 nm excitation wavelength

The SERS spectrum of the methanol extract of the Fycompa sample is shown in Figure 4.11. Notably, most of the well-defined SERS features observed in Figure 4.11 can be traced back to the FT-Raman signals of the above discussed API. We remark that the difference between the position of the CN stretching line (and other API features, as well) in the SERS spectrum, as compared to the FT-Raman, highlights that such signals originate from drug molecules adsorbed on the Au film, that is, not from perampanel recrystallized from the solution. This indicates the successful SERS measurement of perampanel in the solution extracted from the Fycompa sample even in the presence of excipients. This

is a promising result in view of clinical applications, where one expects the interference from organic molecules co-extracted with the API from the patient plasma samples.

### 4.3.1 Ag-Au alloy nanoclusters: synthesis and characterization

Aiming at obtaining systems with variable Ag-Au ratios, Au and Ag colloidal solutions (produced ablating high purity Au and Ag target, as discussed before, using the ns laser) were mixed in different volumetric ratios and then irradiated with ns- laser light, leading to the formation of  $\text{Au}_{1-x}\text{Ag}_x$  alloys.

Looking at the optical absorbances in Fig. 4.12a we observe that the intensity ratios between Ag and Au plasmon peaks correlate with the volumetric ratios used to prepare the colloidal mixtures. Thus, neglecting to a first approximation absorptivity differences between Ag and Au NPs, we can transpose volumetric ratios into atomic fractions.  $\text{Au}_{1-x}\text{Ag}_x$  ( $x = 25; 50; 75$ ) alloyed NPs were synthesized by a post-synthesis ns irradiation treatment of the starting colloidal mixtures. The optical properties of such NP mixtures were investigated as a function of stoichiometry and synthesis history. In Fig. 4.12 the position of the plasmon maximum (observed for the Ag and Au NPs at 410 and 515 nm, respectively) remains almost unchanged in the different mixtures, while their relative intensity changes according to the stoichiometric ratios of the mixtures. Such mixed colloids are mainly characterized by NPs with size less than 10 nm as shown in the micrograph from  $\text{Au}_{75}\text{Ag}_{25}$  (Fig. 4.12b).

In Fig. 4.13 we report, for the illustrative case of  $\text{Au}_{75}\text{Ag}_{25}$ , the absorbance change undergone by the solution upon a post-synthesis irradiation stage using again radiation at  $\lambda$  532 nm, with  $\tau$  6 ns pulses, depositing an energy density value  $F=1.2 \text{ J cm}^{-2}$ . The post irradiation lasted for a time  $t$  120 min. A single absorption peak emerges at about 505 nm, associated to the disappearance of the Ag spectral contribution at about 410 nm. Such a feature indicates that Ag-Au alloy NPs were formed after the post-synthesis irradiation. Support to this hypothesis is provided by the same qualitative features, with a single plasmon peak, of the profile displayed by ps-PLAL prepared colloids synthesized from a home-made  $\text{Au}_{50}\text{Ag}_{50}$  alloy target as shown in the inset of Fig. 4.13a. In

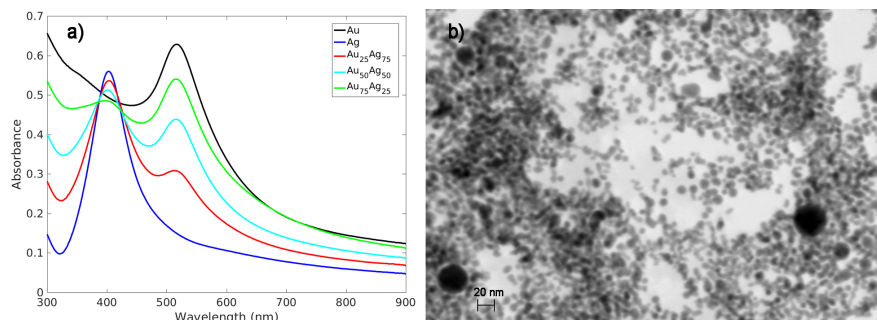


Figure 4.12: a UV-vis spectra of films obtained spraying and drying colloidal suspensions on transparent inert substrates; b STEM micrograph of an  $\text{Au}_{75}\text{Ag}_{25}$  colloid droplet dried on a STEM grid

Fig. 4.13b is shown also a STEM image of the ns-irradiated  $\text{Au}_{75}\text{Ag}_{25}$  colloids. Besides coalescence, the lack of an apparent core-shell structure in the picture strongly suggests that the NPs are alloys rather than core-shell composites.

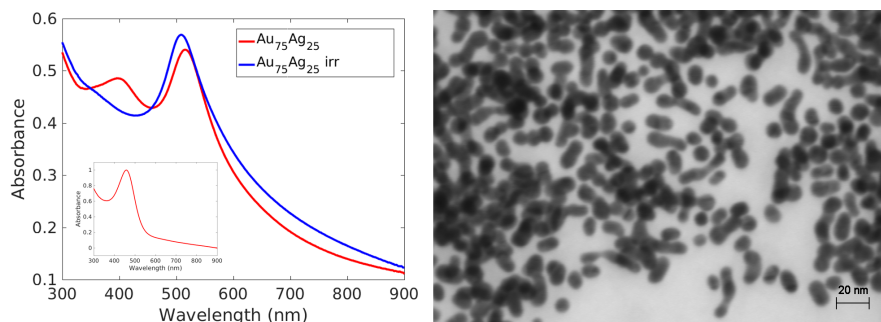


Figure 4.13: (a) UV-Vis spectra of films obtained spraying on transparent inert substrates and drying colloidal suspensions of  $\text{Au}_{75}\text{Ag}_{25}$  as prepared and after post-synthesis irradiation; in the inset the spectrum of the colloid obtained ablating an alloy target. (b) STEM micrograph of the  $\text{Au}_{75}\text{Ag}_{25}$  post-synthesis irradiated colloid droplet dried on a STEM grid: evidence for coalescence and lack of core-shell structures

The first example deals with the development of a method for the quantification of APO in water solution by means of SERS spectroscopy, and the subsequent evaluation of the applicability of the method to the detection on

samples of clinical origin. The main result has been to obtain a SERS signal of apomorphine (APO)  $3.3 \times 10^{-4}$  M water solution adsorbed onto Au and  $\text{Au}_{75}\text{Ag}_{25}$  alloy substrates (see Fig. 4.14).

In Fig. 4.14 are shown preliminary SERS spectra measured from the Au and  $\text{Au}_{75}\text{Ag}_{25}$  alloy substrates after exposition to an aqueous solution of apomorphine (concentration of  $3.3 \times 10^{-4}$  M). No Raman signal was detected using the Au substrate while, for the  $\text{Au}_{75}\text{Ag}_{25}$  alloy substrate, the most intense characteristic Raman features of APO, centered at 1515 and 1353  $\text{cm}^{-1}$  were clearly observed.

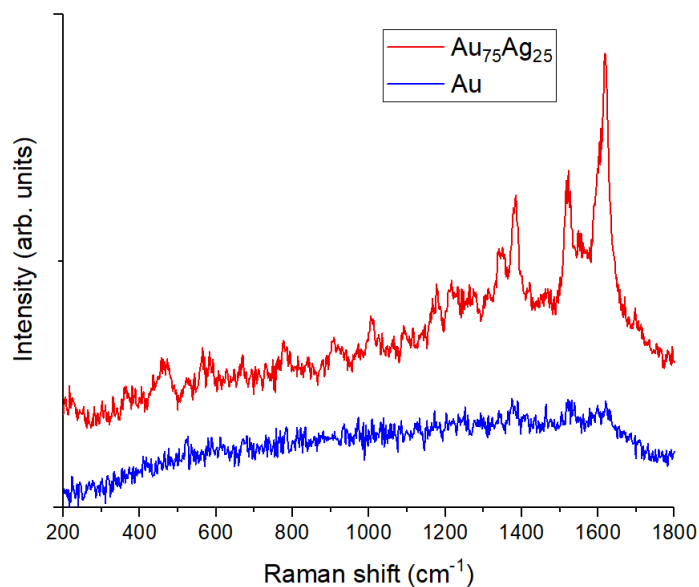


Figure 4.14: SERS spectra of APO adsorbed onto the surface of an Au (blu line) and on  $\text{Au}_{75}\text{Ag}_{25}$  alloy (red line) substrates. The measurement were performed at 514 nm wavelength and at the laser power of 0.1mW.

## 4.4 Ultraviolet plasmonic response of Rhodium nanoparticles

As discussed in the previous paragraphs, SERS substrates based on gold and silver nanostructures are extensively explored for high local electric field



enhancement only in visible-NIR region of the electromagnetic spectrum. However, ultraviolet Surface enhanced Raman spectroscopy (UV-SERS) has recently emerged as an efficient molecular spectroscopy technique for ultra-sensitive and ultra-low detection of analyte concentration. Thus, the template synthesis of controlled nanoscale size metallic nanostructures supporting localized surface plasmon resonance (LSPR) in the UV region should be explored in view of potential applications in optoelectronic, catalysis and magnetism. Among the synthesized materials, Indium nanoparticles exhibit active surface plasmon resonance (SPR) in ultraviolet (UV) and deep-ultraviolet (DUV) region with optimal absorption losses. This extended accessibility makes indium a promising material for UV plasmonic, chemical sensing and more recently in UV-SERS. Moreover, several others metals (like Al, Mg, Ga, Rh, etc.) present analogous interesting properties, but also with some important drawbacks.

Aluminum is a particularly promising metal for UV nanoplasmonics because it is one of the most abundant materials in the Earth's crust, it is inexpensive, and it has compelling electromagnetic properties [119, 120]. However, Al suffers from the formation of an oxide layer several nanometers thick that limits its UV plasmonic performance and utility for applications such as plasmon-assisted photocatalysis requiring contact with the metal surface [121]. Magnesium, another promising metal for UV plasmonics, forms an even more aggressive oxide, which severely limits its utility [122]. Although Gallium is an appealing metal for UV plasmonics because of its self terminating oxide layer being only a monolayer thick [123], it has lower electrical conductivity and presents a liquid-solid phase transition near room temperature that hinders its manipulation. On the overall, for each of the above mentioned materials, the deleterious effect caused by the metal's native oxide, the subsequently accelerated photodegradation and photocatalysis limits their effective technological use [124].

Particularly intriguing metal whose UV plasmonic behavior has only recently been discovered is rhodium, already well known for its catalytic activity produced by a partially filled d-shell and its commensurately low tendency to oxidize [125]. Rh nanoparticles (NPs) may be synthesized into a variety of shapes through chemical methods with nanometer size control [126]. A recent theoretical study found that only Rh has a strong UV plasmonic response and

it is possible to fabricate Rh nanoparticles smaller than 10 nm through chemical means [127]. Moreover, Rh is routinely used as a hydrogenation catalyst for a wide variety of alkenes, alkynes, and aromatic cyclic arenes, as well as nitriles, pyridines, and various N-heterocycles. Indeed, the primary industrial use of Rh is in three-way catalytic converters to reduce  $\text{NO}_x$ , where Rh is often alloyed with Pt and Pd because of its corrosion resistance [128]. Given the rapidly growing interest in plasmonically assisted photocatalytic processes, Rh represents a tremendously promising metal for combining plasmonics and catalysis. In particular, there is the real possibility of enhancing rhodium's already favorable catalytic and SERS activities by UV illumination near its plasmonic resonance, by contemporarily limiting the effects of oxide shell which, as already outlined, affects the plasmonic behavior of this type of NPs.

The research activity, presented in the next paragraph, will be addressed to the synthesis and characterization of (Rhodium)-(Rhodium oxide) nanoparticles, in different liquid media, by the PLAL technique. The goal is to tune the oxide chemical bonding fraction with respect to Rh metallic phase and the morphological properties of the synthesized nanostructures, directly during the ablation process by changing the PLA parameters.

#### **4.4.1 Rhodium oxide nanoparticles: synthesis and characterization**

Although various noble metal (e.g. Pt, Pd and Au) structures have been synthesized by hard- and soft-templating methods, rhodium (Rh) nanoparticles have never been generated via PLAL. However, PLAL technique should allow a successful synthesis of Rh based nanoparticles with a well-defined composition, a high surface to volume ratio, a controlled size distribution and an high stability in the colloidal phase. Then, PLAL processes were carried out ablating a high purity (99.9%) rhodium rod target in ethanol, a weakly oxidizing liquid and in water, a significantly oxidized solvent, by a Nd-YAG laser operating at 10 Hz repetition rate with a pulse width of 5 ns. All the ablation processes were made with a laser fluence of  $2 \text{ J/cm}^2$  and irradiation time of 40 min. First, the ablation conditions were optimized by changing the laser fluence and the ablation time in order to determine the appropriate conditions leading to the

highest production of NPs.

In Fig. 4.15 are shown STEM images (a,c) and size distribution histograms (b,d) for the samples prepared in water and in ethanol, respectively. The shape of the NPs is almost spherical but their size and density distributions are markedly affected by the solvent. The nanoparticle size is significantly smaller when prepared in water.

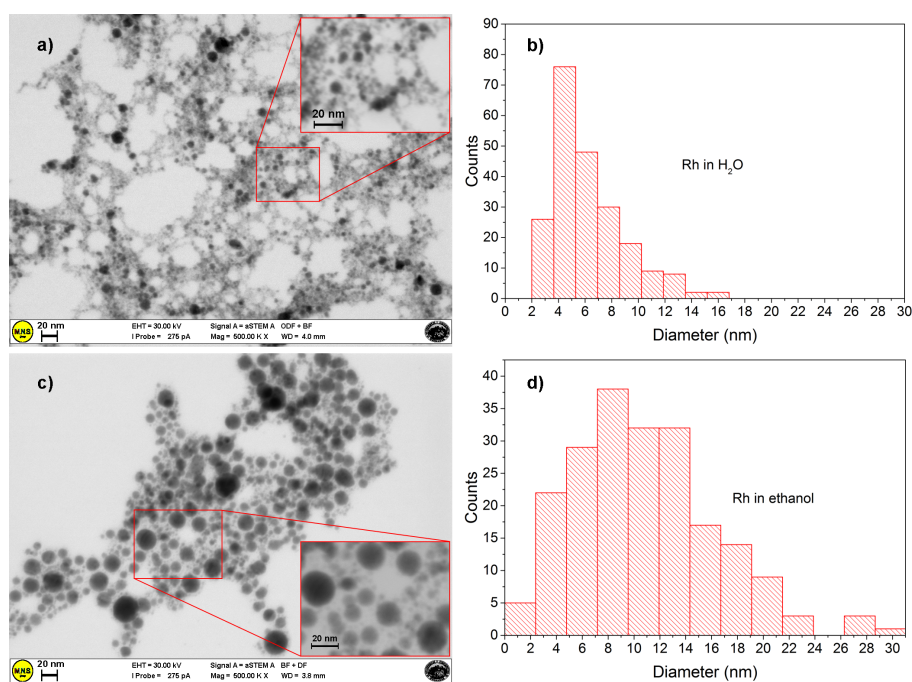


Figure 4.15: STEM image (a) and size distribution histogram (b) for the NPs prepared in water; (c, d) corresponding information for the NPs prepared in ethanol.

Liquid environment affects also the colloids optical response, as shown by the absorption spectra shown in Fig. 4.16. An absorbance contribution associated to the synthesized Rh NPs surface plasmon resonance (SPR) was identified below 400 nm for all the samples. For the samples prepared in ethanol, an additional absorption feature is observed around 340 nm, which may be ascribed to Rh-C bonds [129]. Moreover, Rh SPR position red-shifts towards higher wavelengths (see Fig. 4.16b) upon increasing NPs size. From these preliminary evidences, it is evident that both the size of the NPs and, in turn, the SPR peak position are

affected by the morphology and by the chemical interactions occurring during the ablation process, depending on whether the PLAL process takes place in water or ethanol.

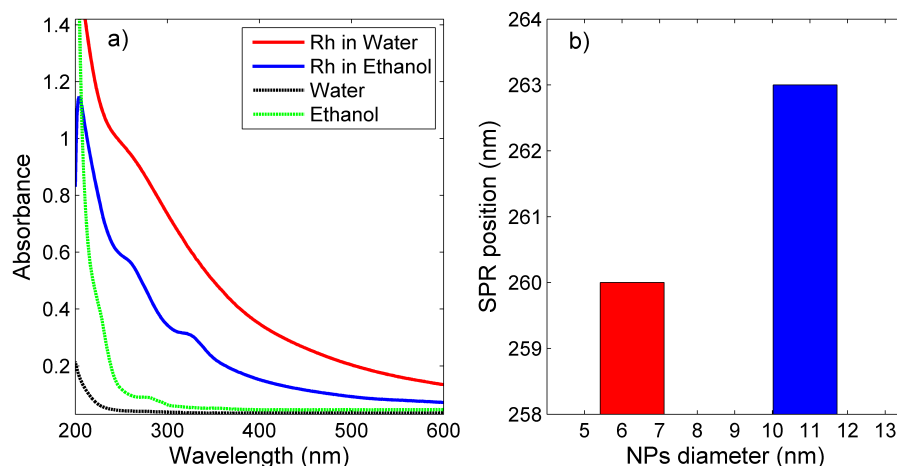


Figure 4.16: Optical absorbance of synthesized Rh NPs (a); SPR position vs NPs diameter medium values (b).

The NPs surface charge, estimated performing Dynamic Light Scattering (DLS) measurements, is negative (about -30 mV) and positive (about 5 mV) for the water and ethanol colloids, respectively. The differences in the zeta-potential can be associated to differences in the electric double layer surrounding the Rh NPs. In a simple picture, these differences may be justified by a different equilibrium involving the adsorption of  $H_3O^+ = OH^-$  species. Globally, the high zeta potential value (about -30 mV) measured in water indicates a relatively high stability of the colloids. Hence, NPs aggregation processes should be less dramatic than in ethanol.

The chemical composition and the bonding configurations of the samples were investigated by XPS. In Fig. 4.17 the Rh 3d fingerprints are assigned to the metallic Rh and the oxidized Rh phases centered at about 307.5 eV and 310 eV, respectively [130]. Thus ablation of Rh target in water leads to the production of mixed Rh/Rh-oxide nanocollids, while in ethanol essentially Rh oxide NPs are produced.

In Fig. 4.18. are shown the micro-Raman and XRD spectra of the synthe-

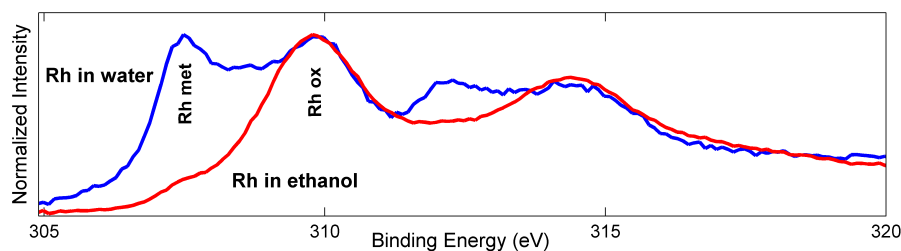


Figure 4.17: HR Rh 3d XPS spectra of the samples prepared in water and ethanol.

sized samples. Micro-Raman pattern appears to be dominated by the broad  $\alpha - \text{Rh}_x\text{O}_y$  feature centered at  $\approx 530 \text{ cm}^{-1}$ . Particularly, in the ethanol based colloids (blu line in Fig 4.18a), the  $E_g$  Rh-O stretching mode, typical of the  $\alpha - \text{Rh}_x\text{O}_y$  crystal structure, appears overlapped to the broad  $\alpha - \text{Rh}_x\text{O}_y$  feature [131, 132, 133]. XRD analysis of the as prepared material shows two main diffraction peaks, indexed as (104) and (006), pertaining to  $\text{Rh}_2\text{O}_3$ . XRD spectrum of the Rh colloids prepared in ethanol displaying, in addition, new peaks ascribe to  $\text{RhO}_2$  phase [134].

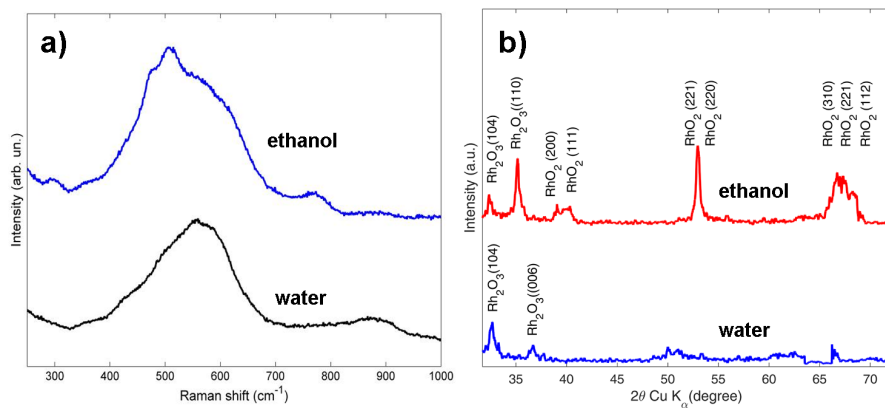


Figure 4.18: Raman (a) and XRD (b) spectra of the samples prepared in water and ethanol.

The colloids were deposited by a spraying procedure (described in Appendix A) on glass to produce SERS substrates. They were tested for SERS activity against a well-known standard analyte (Rhodamine-6G, hereafter abbreviated as RH-6G). A drop of  $10^{-4} \text{ M}$  water solution of RH-6G was cast on the Rh-

covered glass substrate and let dry before the micro Raman measurements. To carry out Raman measure, the laser power was kept at 1mW and the 457nm laser excitation was focused through a 50X objective onto the sample surface. The Raman signal was integrated for 3s, 22 s and 110 s in order to investigate about the possible photodegradation effects. No detectable Raman activity was observed for the colloids prepared in ethanol (not shown). This behaviour could be due to the low content of the oxidized Rh-O coordinated species.

On the contrary, the water colloids substrates (characterized by a well defined stoichiometric  $\text{Rh}_2\text{O}_3$  phase) show the RH6G Raman signals in good agreement with the reference spectrum. In Fig 4.19 are shown Raman spectra of RH6G onto bare glass (a) and Rh-covered glass (b) substrates. Well defined Raman peaks, ascribed to the stretching modes of aromatic C atoms, at about 1190, 1315, 1365, 1515 and 1650  $\text{cm}^{-1}$  are visible [135]. No clear Raman feature is evident for the bare glass substrate soaked in the RH6G  $10^{-4}$  M concentration solution even by extending the integration time to 240 s.

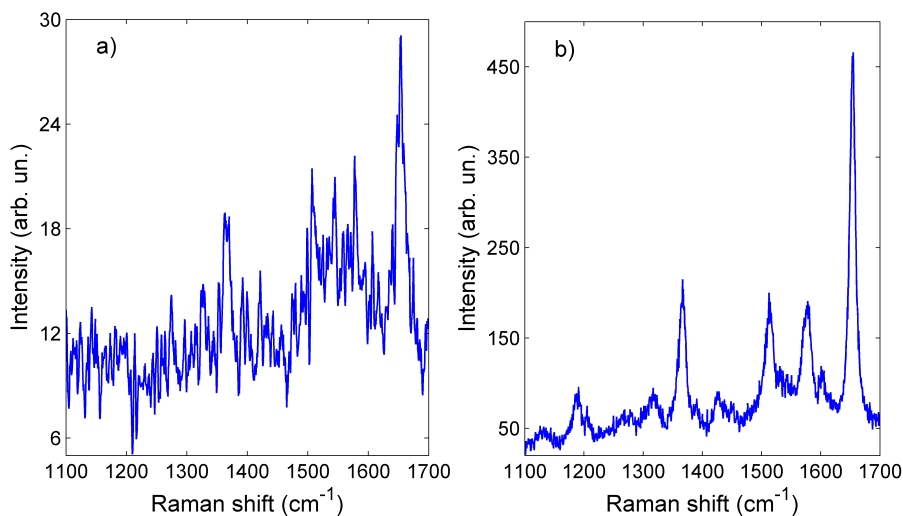


Figure 4.19: Raman and SERS spectra of RH6G drop cast on glass (a) and on Rh-covered glass (b), respectively (see text for experimental detail).

In fig. 4.20 are shown different acquisition times SERS spectra. As exposure time increases, the intensity of the rhodamine Raman signals decreases until it disappears altogether after 110 s, while only the fluorescence signal emerges.

This trend is consistent with photodegradation and formation of less conjugated species of RH6G.

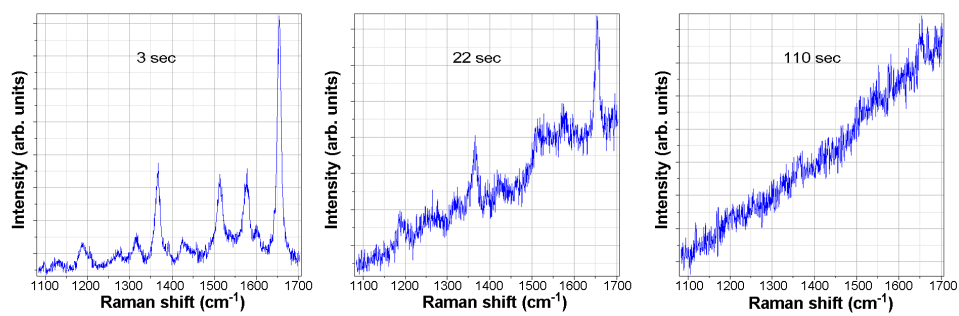


Figure 4.20: Different acquisition times SERS spectra.

## Chapter 5

# Plasmonic Noble Metal Nanoparticles for drug delivery

Nanomedicine deals with diagnosis, monitoring and treatment of diseases and as well as control and understanding of biological systems. Several nanomaterials were suitably designed in order to develop multi-modal systems able to mix the diagnostic and the therapeutic action in a single one structure, which carries the drug [136]. On the other hand, it is well known that drugs entrapped into polymeric nanostructures are primarily released in a passive manner, usually by simple diffusion during spontaneous hydrolysis of the polymer matrix. This is normally a slow process that may take from a few days to months. Otherwise, external stimuli including optical irradiation, electrical and magnetic fields can be utilized to suitably trigger the drug-loaded carriers to release the drug content in a controlled manner [137].

In this view, gold, silver and iron oxide nanoparticles (NPs) are valuable building blocks for the development of drug delivery systems (DDS), because they exhibit low cytotoxicity and good cell permeability. Due to their high surface area to volume ratio and easy interaction with biomolecules (e.g. enzymes, antibodies and DNA) and cells, they are very attractive candidates for use as



carriers in medical diagnosis and treatment, and for a wide variety of biomedical applications (biological sensing, imaging and nanomedicines) derived from their optical properties [138].

The metal-polymeric composites show a drug release profile, which is strongly dependent on laser wavelength and nanoparticles Surface Plasmon Resonance (SPR). The resonant laser light excites the SPR of the NPs and the absorbed energy is converted into heat due to electron-photon collisions. The localized and intensive heating of the metallic NPs results in the thermal expansion of the polymer; thus, the drug starts to diffuse out and it is released in an active and controllable manner [139]. In particular, polymeric nanostructures bearing a hydrophobic inner core and hydrophilic outer shell are considered ideal vehicles for antitumor drug delivery due to their ability to self-assemble into nanosized core/shell structures in aqueous media. In particular, their hydrophobic inner core is a suitable reservoir for hydrophobic anticancer drugs. At the same time, the hydrophilic outer shell facilitates avoidance of the reticuloendothelial system as well as long blood circulation, and the improvement of the enhanced permeation and retention effect in tumor tissue [140]. Compared to other materials like smart hydrogels, environment-responsive nanofiber-based drug delivery systems are relatively new but possess incomparable advantages due to their greater permeability, which allows shorter response time and more precise control over the release rate.

Thus, the engineering of a polymeric nanofibrous membrane designed for the simultaneous encapsulation of therapeutic agents, thermally activable metallic NPs and non-toxic iron oxide magnetic NPs, is a technological challenge that would enable controlled SLB release [141]. In fact, the use of polymer blends can improve the tunability of the physico-chemical and mechanical properties of the drug-loaded fibers, which can be conveniently employed for local and controlled administration of drugs, i.e., as transdermal delivery systems or as implants releasing bioactive molecules, including proteins and anticancer drugs [142].

Nowadays, electrospun-nanofibers are ideal candidate for a wide range of biomedical applications, such as drug and gene delivery, wound healing, and tissue engineering since they form a large, interconnected porous network with

a high surface-to-volume ratio. From literature [143], it is known that electro-spinning parameters influence the drug distribution in the fiber cross-section and the subsequent release efficiency. Otherwise, active and controllable drug release can be achieved by incorporating thermally activated Au or Ag NPs in the polymer matrix, followed by laser light irradiation [144]. In fact, the addition of noble metal NPs confers thermoplastic properties to the polymers and this endows the nanocomposite with peculiar optical properties, improving their performance in releasing the drug upon light irradiation.

In the present study, Au, Ag and iron oxide NPs, synthesized by pulsed laser ablation were embedded alternatively into PEG-PLGA and PEG-PLA copolymers. Particularly, two differently structured nanocomposites, namely particles and fibers respectively, were synthesized and their influence on the drug release phenomenon was investigated. The synthesized nanocomposites were remotely activated by laser light and a magnetic field to release on demand the drug, namely silibinin (SLB), a flavonolignan with promising anti-neoplastic effects. The delivery of SLB is hindered by its complex hydrophobic nature, which limits its bioavailability. In fact, the low aqueous solubility of SLB decreases its bioavailability and distribution, thus limiting its clinical role [145]. This leads to the need for an alternative approach to overcome the limitations of hydrophobic drugs, to increase their biocompatibility and improve their efficacy.

## **5.1 Biocompatible silver NPs embedded in a PEG-PLA polymeric matrix for stimulated laser light drug release**

### **5.1.1 Ag NPs synthesis**

Pulsed Laser Ablation of high-purity (99.9%) silver rod target in pure water and in polyvinyl alcohol (PVA)-water solution was carried out by using the same setup described in chapter 4 for the picosecond laser, ranging laser power density from 0.6 up to 3 W/cm<sup>2</sup>. The PVA water solution was obtained mixing 7.5g of PVA (PM = 86000) in 30mL of distilled water.

It is well known that an efficient control of the ablation parameters (flu-

ence, pulse duration, wavelength) is critically important to obtain Ag NPs with tailored size distributions and concentration [57]. Hence, to discern the appropriate conditions to achieve the higher NP productivity, the ablation process was carried out in water varying the laser power density  $P$  and the ablation time  $t$ . Firstly, it was fixed the laser frequency at 100 kHz and the ablation time at 2 min, and the laser power was varied between  $0.6 \text{ W/cm}^2$  and  $3.0 \text{ W/cm}^2$ . The optical absorption spectra of the Ag NP colloids as a function of the ablation parameters (Fig. 5.1) are characterized by peak centered at about 400 nm, ascribed to silver SPR. Upon increasing the laser power density  $P$  (Fig. 5.1a), it was observed a slight red-shift of the absorption peak, together with a new contribution to the absorption at about 650 nm, which is indicative of a clustering process of the existing NPs ([146, 147].

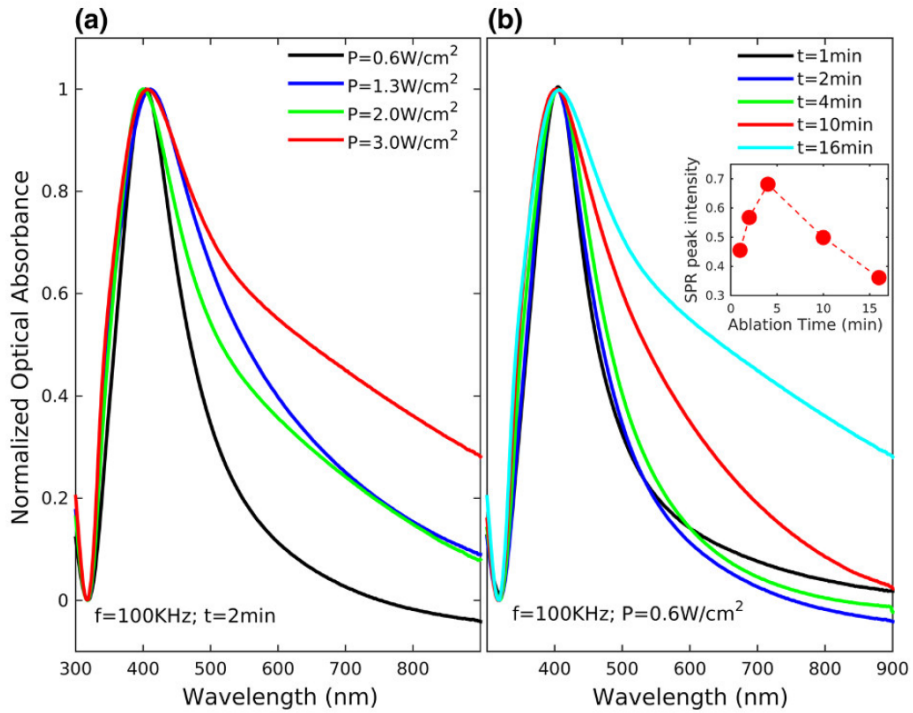


Figure 5.1: Optical absorption spectra of silver nanocolloids prepared in water varying (a) laser power density  $P$  and (b) ablation time  $t$ .

On the overall, from the linear relationship between the optical absorption intensity and the size of the nanocolloids reported by Lee et al. [148], it emerges

that the optimal laser power value to obtain NPs with reduced dimensionality is  $0.6 \text{ W/cm}^2$ . Thus, to achieve the highest productivity of NPs, the ablation experiments were carried out in water fixing the laser power at  $0.6 \text{ W/cm}^2$  and varying the ablation time  $t$ . In Fig. 5.1b and its inset, the normalized optical absorption spectra and the SPR signal intensity trend are shown as a function of the ablation time  $t$ . Again, a well-defined absorption band is visible at around 400 nm in all the spectra and the SPR feature is almost unchanged up to 4 min of ablation time. On the other hand, when the ablation process was carried out for 10 min, SPR optical absorption intensity decreases (see inset Fig. 5.1b) as well as its features change, broadening toward longer wavelengths. This could be explained by considering that the generated plasma strongly scatters and absorbs the incoming pulses: less energy reaches the target and, hence, the ablation efficiency is drastically reduced [149]. Furthermore, during the 10 min ablation process, the confining liquid favors the agglomeration of the NPs produced in the first five minutes. Overall, in relation to the higher NP productivity, it emerges that the optimal ablation time is 2 min, fixing the laser power density at  $0.6 \text{ W/cm}^2$ . Since the influence of the liquid environment and the role of host polymer/organic matrix on the formation of size-controlled metallic NPs is well known [150], the ablation processes were carried out in a PVA-water solution in order to control the Ag NPs size and distribution.

The SPR signal is barely visible in the colloids prepared in PVA with a single step ablation, while its feature is narrower and more intense when the ablation was carried out in PVA with the steps of 1 min for a total ablation time of 16 min, with 10 min between the ablative processes (Fig. 5.2). The efficiency of the Ag NPs productivity in the two liquids is very different in the same ablation time, indicating that the combined effects of several factors and mechanisms (i.e., refractive index of the medium, scattering, absorption, etc.) are involved in the synthesis process [32].

TEM measurements were carried out (Fig. 5.3) to further outline the difference in terms of size and distribution between the silver nanocolloids prepared in water and in PVA, at the same power density ( $P = 0.6 \text{ W/cm}^2$ ). A uniform distribution of well defined spherical Ag NPs with low dimensionality are obtained in PVA-water solution (Fig. 5.3b), not observed in water (Fig. 5.3a).

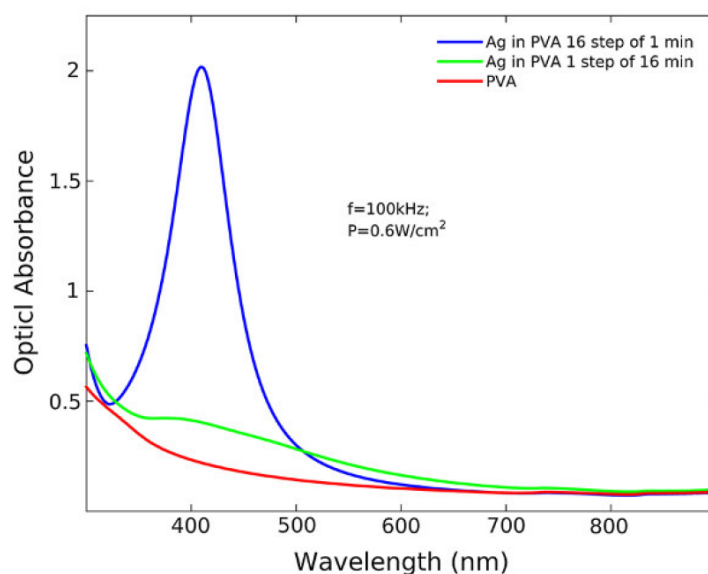


Figure 5.2: Optical absorption spectra of PVA and Ag NPs prepared in aqueous solution of PVA, with varying ablation time

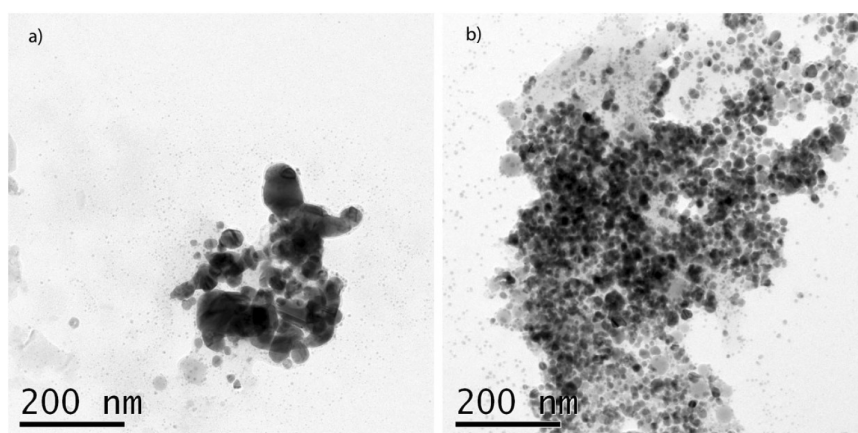


Figure 5.3: TEM images of Ag NPs synthesized at  $P = 0.6 \text{ W/cm}^2$  in water for  $t=2 \text{ min}$  (a) and in a PVA-water solution for  $t=16 \text{ min}$  (b) realized with 200kV acceleration voltage by a JEM-2010 electron microscope.

### 5.1.2 PEG-PLA copolymer synthesis

PEG (MW=8kDa, 123mg, 3 equiv) and PLA (MW=75-120kDa, 500 mg, 1 equiv) were dissolved in anhydrous toluene (20 mL) and then added to Stannous

2-ethylhexanoate (purity 99.8%, 0.22 equiv). Then, the solvent was evaporated and the residue was dissolved in 13mL of dichloromethane (DCM). After DCM evaporation, the aqueous phase was centrifuged at 6000 rpm for 45 min and a solid was isolated and washed twice with water.

In Fig. 5.4 is shown the  $^{13}\text{C}$  NMR spectrum of the PEG-PLA copolymer. The features corresponding to PEG and PLA are well defined one with respect to the other. Moreover, two additional peaks, ascribed to carbonyl and aliphatic contributions, are present and index of the interactions of the different sequences randomly distributed along the copolymer chains [151].

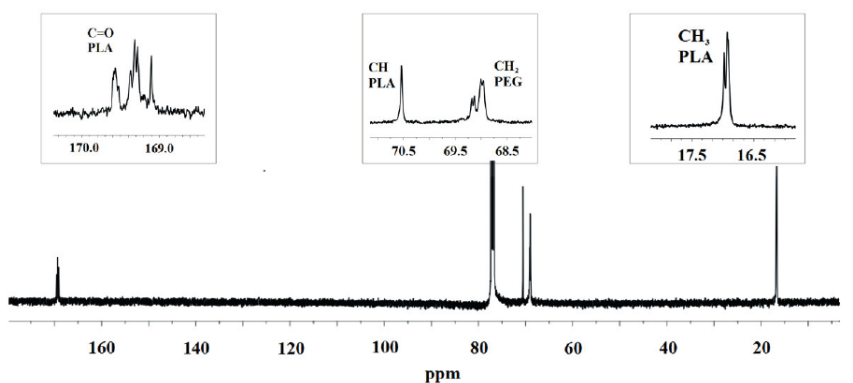


Figure 5.4:  $^{13}\text{C}$  NMR spectrum of PEG-PLA in  $\text{CDCl}_3$ .

NMR spectroscopy was also exploited to study the self-assembly properties of PEG-PLA @Ag/SLB composite in water and to confirm the drug incorporation (Fig. 5.5). In particular, when the spectrum is registered in  $\text{D}_2\text{O}$ , the specific peaks of PLA and SLB disappeared, while the characteristic peak of PEG was the only one observed. However, the  $^1\text{H}$  NMR spectrum revealed all the peaks of PEG, PLA, and SLB in  $\text{DMSO-d}_6$ , a solvent in which the system is disassembled, according to literature [152, 153]. These results indicated that our PEG-PLA@Ag/SLB is an amphiphilic composite able to self-assemble in water as core-shell-type NPs, with a PLA-based hydrophobic core responsible for drug incorporation, and a water-soluble PEG back-bone that constitutes the outer shell.

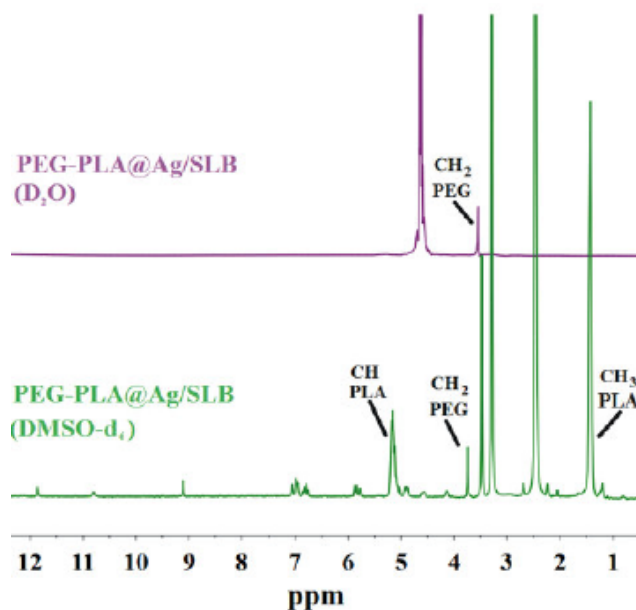


Figure 5.5:  $^1\text{H}$  NMR spectrum of PEG-PLA in  $\text{D}_2\text{O}$  and  $\text{DMSO-d}_6$ .

### 5.1.3 PEG-PLA@Ag-PVA composite synthesis

PEG-PLA copolymer (50 mg), dissolved in 1 mL of DCM, was added into 9mL silver solution and PVA-water solution (7.5% w/v). The emulsion was placed under gentle stirring inducing solvent diffusion into the external phase. The aqueous phase was centrifuged at 6000 rpm for 20 min and a solid was isolated.

The PEG-PLA and PEG-PLA@Ag FT-IR spectra (Fig. 5.6) showed almost the same absorption peaks as pristine PEG and free PLA. A slight shift of the carbonyl stretching frequency is observed from  $1745\text{ cm}^{-1}$  for free PLA to  $1748\text{ cm}^{-1}$  for the copolymer PEG-PLA, confirming the formation of a new ester linkage. In addition, the interaction of Ag NPs with the composite induces several slight modifications in the PEG-PLA@Ag IR spectrum indicative of the conjugation of oxygen atoms with the Ag NPs, such as (a) a slight shift of the carbonyl stretching frequency to  $1751\text{ cm}^{-1}$ , (b) a strong decrement in the intensity and a shift of the  $-\text{CH}_2$  stretching frequency of PEG from  $2874\text{ cm}^{-1}$  to  $2880\text{ cm}^{-1}$ , and (c) a shift of the intense C-O stretching frequency of PEG-PLA

from  $1081\text{ cm}^{-1}$  to  $1084\text{ cm}^{-1}$ .

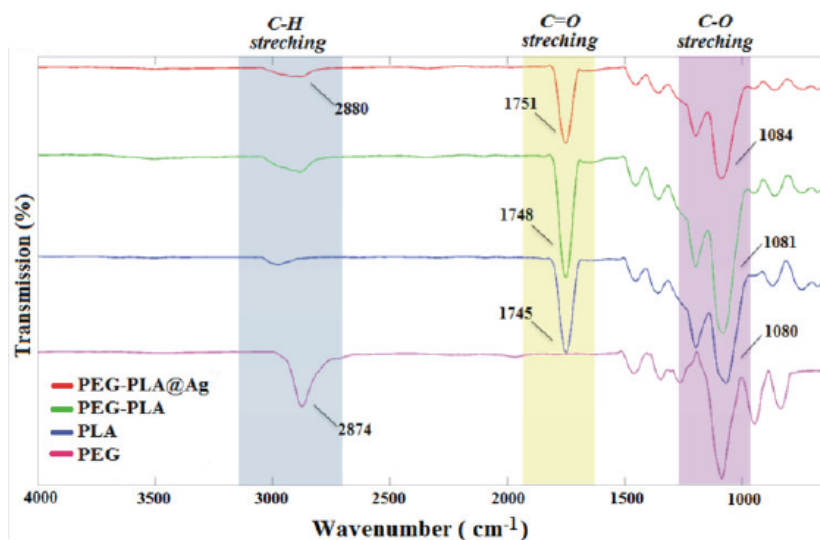


Figure 5.6: FT-IR spectra of PEG-PLA@Ag, PEG-PLA, PLA and PEG.

#### 5.1.4 PEG-PLA@Ag-PVA/SLB composite preparation

PEG-PLA@Ag composite loaded with SLB was prepared at a 50:5 polymer/-drug weight ratio [151, 144]. The molecular weights ( $M_W$ ) of the PEG-PLA, PEG-PLA@Ag, and SLB-loaded PEG-PLA@Ag composites were evaluated by Static Light Scattering (SLS). The scattered light intensity of the polymeric solution is proportional to the product of the weight-average molecular weight and the concentration of the solution ( $I \approx (M_W \cdot C)$ ). This is called a Debye plot ( $KC/R_\theta$  versus  $C$ ) and allows the determination of absolute molecular weight and the 2nd virial coefficient ( $A_2$ ) values. Therefore, a plot of  $KC/R_\theta$  versus  $C$  gives a straight line whose intercept at zero concentration is  $1/M$  and whose gradient is  $A_2$ :  $KC/R_\theta = (1/M + 2A_2C)$ . The estimated  $M_W$  values of PEG-PLA, PEG-PLA@Ag, and PEG-PLA@Ag/SLB composites are of 103.9 KDa, 104.6 KDa, and 116.3 KDa, respectively. On the other hand, the  $A_2$  positive values of  $1.5 \times 10^{-5}$ ,  $1.9 \times 10^{-5}$ , and  $2.7 \times 10^{-5}$  for PEG-PLA, PEG-PLA@Ag, and PEG-PLA@Ag/SLB, respectively, indicate that all the composites tend to



remain in solution, avoiding the aggregation process.

The estimated concentration of Ag in the composite is about  $6.0 \cdot 10^{-6}$  M, indirectly calculated by UV-Vis absorption, taking into account the microscopy results (see Fig. 5.7) and assuming an average molar extinction coefficient of  $2.0 \cdot 10^4 \text{ M}^{-1} \text{ cm}^{-1}$  according with the literature [154]. Furthermore, the amount of Ag loaded into the composite was estimated by EDX data and it is about 0.5 %, while no signal related to Ag was detected by XPS probe, indicating that Ag NPs are barely present on the surface, but rather they are located within a few nanometers (about 10 nm) from the sample surface.

SEM image of the PEG-PLA@Ag composite (Fig. 5.7a) shows characteristic sponge-like spheres with an average size of  $2 \mu\text{m}$  and a bumpy and porous surface. The formation of spherical protrusions and pores can be explained by taking into account an interfacial tension instability, dependent on the organization of the polymer at the interface during the emulsion evaporation process [144]. Due to the porous morphology of the sample, the Ag NPs cannot be distinguished by SEM images even if they are detected by the EDX probe. The SEM-EDX analysis (Fig. 5.7b) shows that Ag NPs are uniformly distributed in the composite, with a size in the range of 5-50 nm (yellow circles), in agreement with the "hydrodynamic" average obtained by DLS. Moreover, DLS measurements show that the PEG-PLA@Ag composite hydrodynamic diameter on an ensemble average is about  $3 \mu\text{m}$  with a PDI value of 0.5 (where 0.5 refers to the most polydisperse population).

### 5.1.5 Light-activated drug release

The SLB amount in the composite was determined spectrophotometrically on the basis of the optical absorbance data and the molar extinction coefficient ( $\lambda^{286} = 11320 \text{ M}^{-1} \text{ cm}^{-1}$ ) previously calculated, using the following equations:

$$\text{Drug content(\%)} = \left( \frac{\text{Drug weight in the NPs}}{\text{Weight of the NPs}} \right) \times 100 \quad (5.1.1)$$

$$\text{Drug loading Efficiency(\%)} = \left( \frac{\text{Drug weight in the NPs}}{\text{Weight of drug used in the formulation}} \right) \times 100 \quad (5.1.2)$$

For evaluation of drug content and loading efficiency, the lyophilized PEG-PLA@Ag/SLB composite was dissolved in PBS by sonication and centrifuged

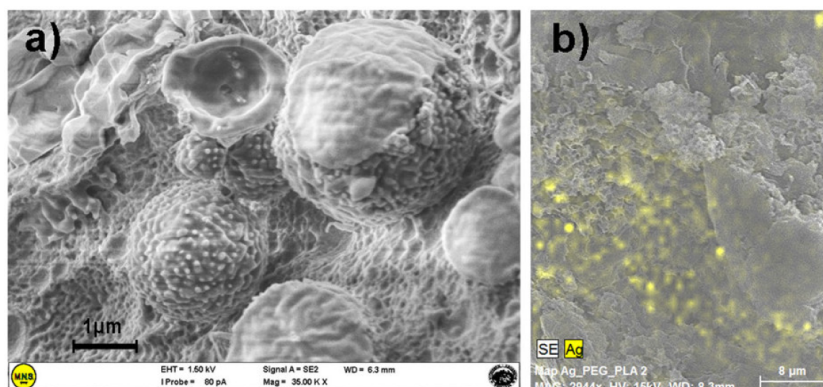


Figure 5.7: (a) SEM image and (b) SEM-EDX analysis results of the PEG-PLA@Ag composite. The presence of Ag NPs is indicated by the yellow color features.

to remove the free drug. Afterwards, the amount of drug present in the NPs was determined spectrophotometrically at 286 nm ( $\lambda_{max}$ ), according to the equations 5.1.1 and 5.1.2. On the basis of the optical absorbance data and the molar extinction coefficient ( $\epsilon_{286} = 11320 M^{-1} cm^{-1}$ ), the drug loading efficiency is about 77 % and the drug content is found to be 7.7 % (0.077 mg of drug/mg of drug carrier).

Additionally, the amount of the drug loaded into the nanocomposite was quantified using the standard calibration curve method. The SLB standard calibration curve was determined in DMSO:PBS 1:99 in the range 10-83  $\mu M$  (10, 21, 31, 42, and 83  $\mu M$ ). The absorbance values at  $\lambda_{max} = 286$  nm versus SLB concentration were plotted with a correlation coefficient  $R^2 = 0.998$ . The estimated drug loading efficiency is about 77 % and the drug content is found to be 7.7 % (0.077 mg of drug/mg of drug carrier).

The release experiments were performed by a dialysis method in 10 mM PBS at pH 7.4. A sample solution (4 mg of PEG-PLA@Ag/SLB dispersed in 4 mL of PBS by sonication for 1 h) was placed in a dialysis bag (MWCO = 3.5-5 kD, Spectra/Por). Next, the dialysis membrane was plunged in 15 mL of PBS and kept at 37°C under stirring. At specific times, 1 mL of release medium was sampled and analyzed by UV-Vis spectroscopy, using the SLB molar extinction coefficient ( $\epsilon_{286}$ ), previously calculated. After each sampling, 1 mL of release

medium was replaced with an equal volume of fresh PBS. The experiment was carried out in duplicate.

For the laser light-triggered release experiments, different lines (454, 465, 488 and 514 nm) of an Ar laser source (laser power value of  $130 \text{ mW}=\text{cm}^2$  for the 488 and 514 nm and of  $20 \text{ mW}$  for the other wavelengths) and the radiation produced by a LED source ( $\lambda=420 \text{ nm}$ , power density value of  $30 \text{ mW}=\text{cm}^2$ ) were used. Each experiment was performed in duplicate and the cumulative released SLB optical absorbance values as a function of time are shown after normalization to the laser power. The values of the SLB cumulative optical absorbance are normalized to the laser power values measured by a power meter, for each wavelength, at the output of the laser source; so the obtained results are unaffected by the irradiation parameters. The composite was suspended in PBS (pH 7.4) at  $37^\circ\text{C}$  and the release was monitored for 6 days.

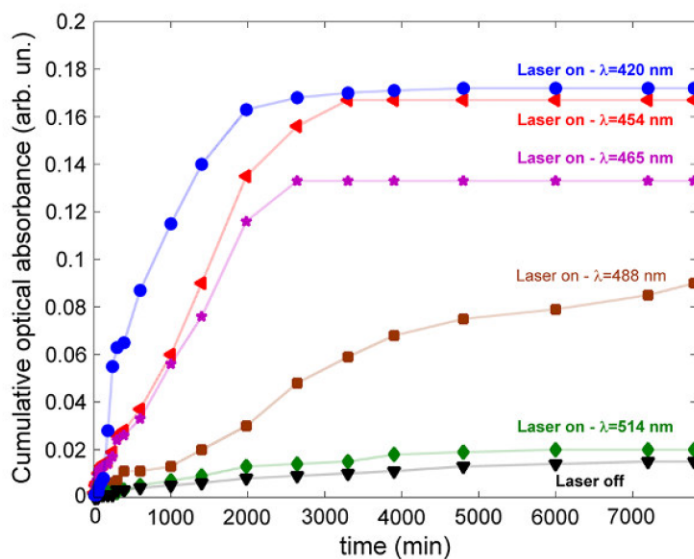


Figure 5.8: Cumulative released SLB optical absorbance values as a function of time.

In Fig. 5.8, the cumulative released SLB optical absorbance values are reported as a function of time. It can be observed that, using the laser source wavelengths of 454, 465, and 488 nm, no substantial drug release was detected at the early stage (before  $1000 \text{ min} \approx 17 \text{ h}$ ), while the drug starts to be released

from the polymeric composite at 2000 min ( $\approx$  33 h). Finally, over 7000 min ( $\approx$  5 days) and for even longer times the drug release remains almost unchanged. Interestingly, by comparing the effects of the different laser wavelengths on the release efficiency, it is evident that the cumulative optical absorbance values estimated for the nanocomposite irradiated with 420 nm wavelength are comparable to those obtained using the 454 nm wavelength, but the drug is more quickly released (50% of the total release occurs within the first 500 min). Thus, the laser with  $\lambda = 420$  nm is the most effective in promoting the SLB release over time, likely because it is the wavelength closer to the plasmon resonance of silver. Conversely, the laser with  $\lambda = 514$  nm, wavelength far from the silver plasmon, exhibits a very poor effect on SLB release, almost the same registered with the laser off. This behavior could be explained by considering the relative contribution of the polymer degradation promoted by the Ag-mediated laser irradiation heating effect that makes the drug diffusion more effective upon irradiation dose to the resonant wavelength, with respect to the non-irradiated sample or to the sample irradiated with laser wavelengths off-resonance with the Ag SPR.

In view of potential applications, compounds biocompatibility is of fundamental importance. In the next section, the biocompatibility of Ag NPs both in water and in PVA-water solution and that of the PEG-PLA@Ag-PVA composite were tested in vitro by SRB assay on NIH/3T3 fibroblast cells.

### 5.1.6 In vitro biocompatibility

In Fig. 5.9a is shown the semilogarithmic plot of the % of cell death versus the Ag content ( $\mu\text{L}$ ) of the tested preparations. Survival curves are evaluated in the SRB assay on NIH/3T3 cells (information about cell culture treatment are reported in Appendix). Data are shown as mean  $\pm$  SD of a minimum of three independent experiments done in quadruplicate. Cell viability of NIH/3T3 cells exposed for 24 h to different concentrations (0.375-3.0 mg/mL) of unloaded and SLB-loaded PEG-PLA@Ag-PVA NPs is shown in Fig. 5.9b. Vehicle-treated cells were used as control. Data represent the percentages compared to control and are expressed as mean  $\pm$  SD of three experiments.

The semilogarithmic plot of the cell death percentage versus the Ag con-

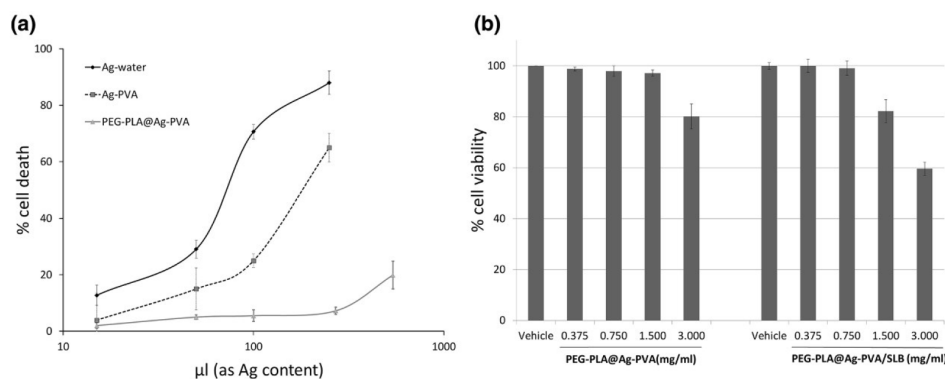


Figure 5.9: (a) Semilogarithmic plot of the % of cell death versus the Ag content ( $\mu\text{L}$ ). (b) Cell viability of NIH/3T3 cells exposed for 24 h to different concentrations (0.375-3.0 mg/mL) of unloaded and SLB-loaded PEG-PLA@Ag-PVA NPs.

tent of the tested samples (Fig. 5.9a) demonstrated that the higher cytotoxic effect was observed for Ag colloids in water, while the addition of PVA reduced the cytotoxicity of silver. Interestingly, PEG-PLA@Ag-PVA showed a better biocompatibility with a weak toxic effect at the highest tested concentration (3 mg nanosystem/mL, containing 180  $\mu\text{L}$  of Ag solution). The results obtained by comparing unloaded and SLB-loaded NPs (Fig. 5.9b) revealed that only the concentration of 3 mg/mL of PEG-PLA @Ag-PVA showed a weak cytotoxic effect in NIH/3T3 fibroblasts cells, while PEG-PLA@Ag-PVA/SLB is able to induce cell death starting from 1.5 mg/mL, and this effect can be clearly related to SLB content (240  $\mu\text{M}$  SLB). It is well known that most chemical drugs including SLB experience the lack of aqueous solubility. SLB is a poorly water-soluble drug (maximum solubility: 100  $\mu\text{M}$ ) and this limitation hinders its clinical usefulness. Our nanoplatform allows advantageously to convey higher concentration of the drug, and the cytotoxic effect, detected on NIH/3T3 fibroblast cells as a proof of principle, demonstrated that SLB is delivered from the vector and bioavailable for its effect. Further investigations are ongoing to assess the antiproliferative effects of our SLB-l oaded nanoplatform on cancer cells by means of laser light irradiation. On the overall, the results show that the drug is released more effectively upon light irradiation in an active and time

definite way. Then, by encapsulating appropriate drugs, the proposed nanovec-  
tor could be used for photothermal therapies that make use of visible optical  
radiation due to the presence of noble metal NPs. In principle and taking into  
account the novelty from fiber-fabrication technology, an injector including an  
optical fiber could be engineered to administer and deliver the light radiation to  
the tumor. Technological advances may suggest the use of more sophisticated  
wirelessly controlled nanowires responding to an electromagnetic field generated  
by a separate device. This system eliminates the tubes and wires required by  
other implantable devices that can lead to infections and other complications,  
whilst allowing the activation of drug release in proximity of areas of the body  
that are often difficult to access.

In the next paragraph, we discuss about the synthesis and characterization  
of PEG-PLGA nanofibrous scaffolds, obtained by electrospinning deposition,  
simultaneous loaded with: i) silibinin, ii) Au/Ag and iii) non-toxic  $Fe_2O_3$  mag-  
netic nanoparticles. In these systems both the time release and the amount of  
drug released at a specific target site was fine tuned by two external stimuli: a  
light source and a magnetic field, respectively. Another interesting aspect of the  
present work regards how the morphological structure can influence the drug  
release. All data obtained about the fiber scaffolds are compared to copolymer  
based on NPs, reported in this paragraph.

## 5.2 PEG-PLGA electrospun nanofibrous membranes loaded with silibinin and $Ag/Au@Fe_2O_3$ nanopar- ticles

Electrospinning is a simple and versatile top-down method for generating  
ultrathin fibers from a wide range of materials, including polymers, compos-  
ites, and ceramics, by applying electric shear stress. During electrospinning,  
the polymer solution, which is typically highly viscous, is forced through a spin-  
neret by a syringe pump and then subjected to a strong electric field. The  
resultant liquid jet evaporates under a controlled temperature and humidity,  
and the remaining semi-solid polymer fiber is deposited onto a collector. The

fluid emission speed from the needle varies in the 2-200 m/s range, depending on the physical properties of solution and processing conditions. This method produces non-woven membranes with individual fiber diameters typically ranging from 50 to 500 nm [155].

Electrospun fiber-based drug delivery systems starting from the previously prepared solutions of PEG-PLGA/SLB@Au and PEG-PLGA/SLB@Ag loaded with SLB and iron oxide nanoparticles were prepared by electrospinning deposition. In our setup (see Fig. 5.10), a coaxial two-way stainless steel needle (with an inner core capillary opening diameter of 0.8 mm and a sheath capillary opening diameter of 1.8 mm) was connected through short path silicone rubber pipes to two syringe pumps, equipped with 10-mL syringes, that enabled fluxing of the NPs-loaded polymers at a very low rate (about 1 cc/h). The  $\text{Fe}_2\text{O}_3$  – PVA solution were flushed through the inner core capillary while the copolymers loaded with SLB and Au-Ag@ $\text{Fe}_2\text{O}_3$  NPs were flushed by the sheath capillary. A voltage of 30 kV DC was applied to the coaxial spinneret, and the solution jet from the needle was collected onto a grounded aluminum plate positioned at a distance of 150 mm from the needle. Subsequently, the aluminum foil was removed from the collecting plate, and the nanofibrous membrane obtained was dried for at least 24 h. All experiments were performed at room temperature in controlled air-dry conditions.

Previously, Ag, Au and  $\text{Fe}_2\text{O}_3$  NPs syntheses were carried out by pulsed laser ablation in water. Specifically, the 532 nm second harmonic emission wavelength of a laser, operating at a repetition rate of 100 KHz (pulse length: 6-8 ps), was used to prepare Ag and Au water colloids. The ablation process was carried out using a laser fluence of  $1.3 \text{ J cm}^{-2}$ , 5 mm of water above the target and an ablation time of 10 min.  $\text{Fe}_2\text{O}_3$  NPs were synthesized by pulsed laser ablation in a PVA 7.5% (w/v) solution. 7.5 g of PVA was dissolved in 30 mL of distilled water. The dispersion was heated under stirring up to  $90^\circ\text{C}$  and refluxed for 2 h. After cooling to room temperature, the dispersion was diluted in water to obtain a 7.5% w/v final solution. Moreover, PEG-PLGA and PEG-PLA copolymers was synthesized as reported in the previous paragraph.

SLB loading in the nanocomposite was 0.088 mg of drug per 1 mg of the drug carrier. We estimated that the drug loading efficiency is about 89% and the

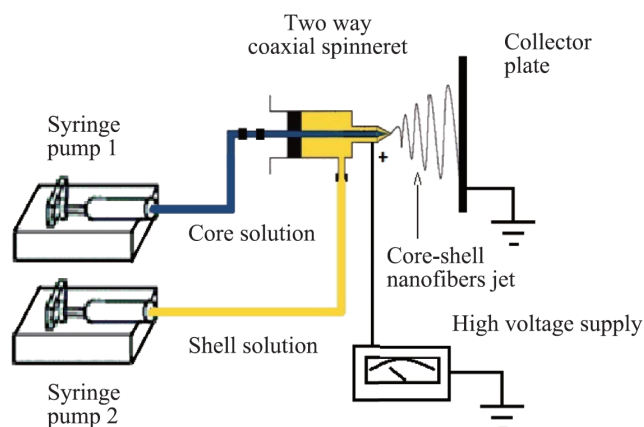


Figure 5.10: Scheme of the electrospinning setup. In the figure, the core and shell solutions refer to  $\text{Fe}_2\text{O}_3$ -PVA and PEGPLGA\_Au-SLB/PLGA in DMF, flowing from the syringe pump 1 and 2, respectively.

drug content is about 8.8%. On the other hand, the thermogravimetric analysis (TGA), under air flow, allowed to estimate that the percentage of Au and  $\text{Fe}_2\text{O}_3$  into the polymers is about 1.5% and 0.9%, respectively. TGA analysis also shows that degradation starts later than in the electrospun scaffold (see Fig. 5.11).

The structure of the iron oxide particles was determined by carrying out Raman spectroscopy and XPS measurements. The Raman spectrum (Fig. 5.12a) is characterized by some contributions, centered at about 226.8, 292.5, 400, 486.5 and  $600\text{ cm}^{-1}$ , ascribed to the Fe-O vibrational stretching mode, in hematite phase ( $\alpha - \text{Fe}_2\text{O}_3$ ) [156]. Fe 2p XPS lineshape (Fig. 5.12b) is characterized by two main contributions centered at 710.7 and 724.2 eV, respectively. The satellite peak at 719 eV is also evident, indicating that the hematite ( $\alpha - \text{Fe}_2\text{O}_3$ ) and maghemite ( $\gamma - \text{Fe}_2\text{O}_3$ ) phases coexist on sample surfaces [157].

Finally, Au and  $\text{Fe}_2\text{O}_3$  NP sizes and distributions in the polymeric composite were determined by using STEM images (Figs. 5.12c, d). The Au and  $\text{Fe}_2\text{O}_3$  NP size ranges from 5 nm up to 50 nm. SEM images of the sample after the electrospinning deposition are shown in Fig. 5. Good quality nanofibers with smooth surface and without beads were obtained (Fig. 5.13a).

The nanofibers, with an average diameter of about 200 nm, are spatially dispersed in random orientations, resulting in a three dimensional porous net (Fig.



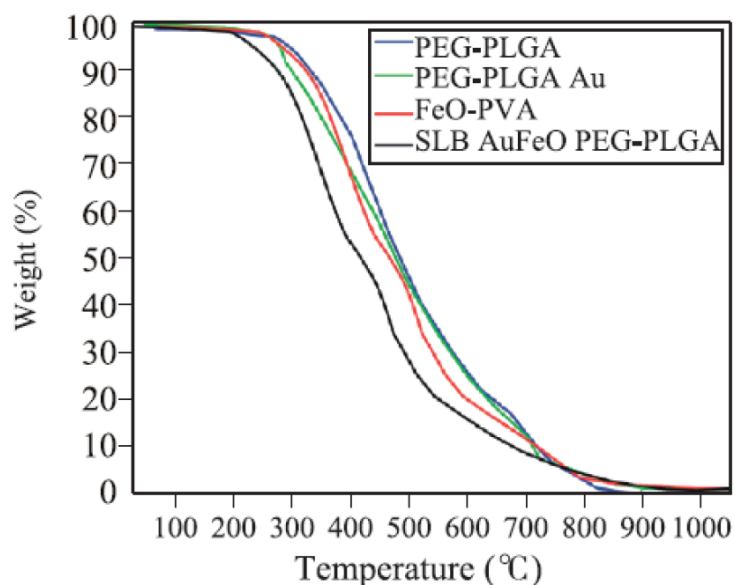


Figure 5.11: TGA profiles for all investigated nanocomposites.

5.13b, c). Therefore, the architecture of the electrospun membrane is composed of two parts, the macroscopic organization of the nanofibers and the secondary structure of the individual fiber arrangement (Fig. 5.13c, d). The random fiber deposition is explained by taking into account the fact that the electrospinning deposition was carried out using a static collector plate configuration. SEM images show that the nanofiber polymeric surface is not decorated by Au and/or  $\text{Fe}_2\text{O}_3$  nanoparticles (Fig. 5.13d). This evidence is supported by the results of XPS and EDX analyses. In fact, XPS probe does not reveal the presence of metallic NPs in the samples, indicating that they are embedded within the nanofibers. Conversely, EDX probe (EDX detected pear-shaped volume dimension is about  $0.7 \mu\text{m}$  while XPS probes only few nanometer in depth) collects the signals from Au and Fe atomic species. Thus, the composition of the system was determined by EDX analysis at different points of the sample. The estimated atomic percentage are: C (on average 80.5%), O (on average 19.2%), Au (on average 0.1%), and Fe (on average 0.2%).

Then, the antibacterial activity of  $\text{Fe}_2\text{O}_3$  nanoparticles, assessed using bacterial functional activities as an indicator of cell viability, is made for a potential

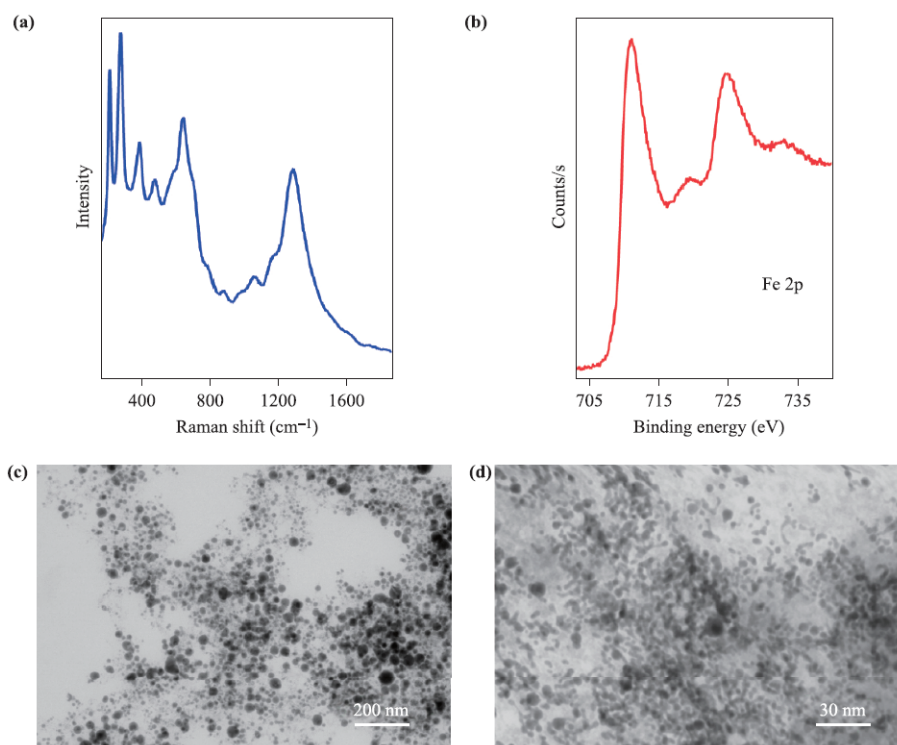


Figure 5.12: Raman spectra (a), XPS results (b), and STEM images of  $\text{Fe}_2\text{O}_3$  (c) and Au (d) NPs in the PEG-PLGA\_Au-SLB/PLGA@ $\text{Fe}_2\text{O}_3$ -PVA nanocomposite.

application as efficient vectors in drug delivery and/or as constituent of specific platform for drug targeting. The procedure adopted is described in the following paragraph.

### 5.2.1 $\text{Fe}_2\text{O}_3$ antimicrobial activity

The antimicrobial activity of  $\text{Fe}_2\text{O}_3$  nanoparticles on *Staphylococcus aureus* was studied by means of MTT [3-(4,5-dimethylthiazol-2-yl)-2,5-diphenyltetrazolium bromide, Sigma M-5655] assay [110].

MTT was dissolved in distilled water to a concentration of 5.0 g/L. Bacteria were incubated at  $37^\circ\text{C}$  in an orbital shaker-incubator for about 14 h. Then, the bacteria solution was diluted in MHB and incubated at  $37^\circ\text{C}$  under agitation at 350 rpm. The pH was not adjusted during the course of cultivation. *S. aureus*

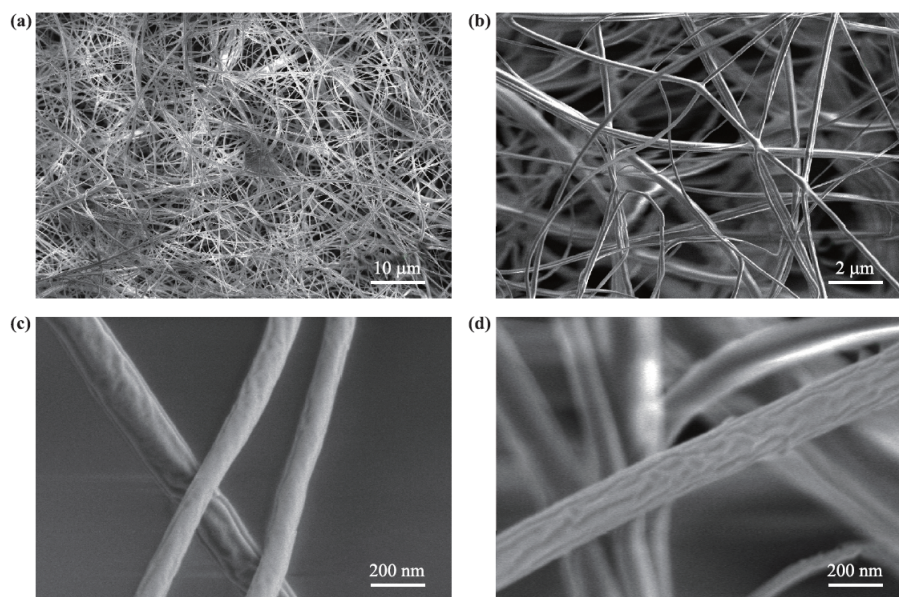


Figure 5.13: SEM images of the nanofibrous membrane realized at 1.5 kV at a working distance of 6mm with a ZEISS-Merlin with Gemini II column.

cell growth was monitored by measuring the optical density of the broth at 600 nm (OD<sub>600</sub>). After three hours, bacterial culture shows an optical density (OD) of 0.9 at 600 nm. According to the standard curve correlating bacteria number with optical density, this value was equivalent to  $5 \times 10^6$  cells/mL.

Iron oxide nanoparticles, both in water or PVA aqueous solutions, were added to bacteria cultures. A culture of bacteria without nanoparticles served as control. MTT reduction assay was carried out according to the procedure described by Wang et al. [158]. The MTT reduction activities of *S. aureus* cells were presented as MTT reduction unit (MRU) per OD<sub>600</sub> and per milliliter culture. One MTT reduction unit (MRU) is defined as an A<sub>550</sub> value of 1.0 produced by the dissolved formazan crystals from the cells in the medium at 37°C in 20 min. All experiments were conducted in triplicate and repeated three times [110].

Hence, the antibacterial activity of Fe<sub>2</sub>O<sub>3</sub> nanoparticles prepared by pulsed laser ablation in water and in PVA aqueous solutions was assessed by a cell metabolic activity assay, using bacterial functional activities as an indicator of cell viability. According to the procedure described by Wang et al. [158], MTT

reduction activity of *S. aureus* cultures, indicated by the parameter MRU (MTT reduction unit), can be estimated as follows:

$$MRU = A_{550} \times \left( \frac{2500\mu L}{200\mu L} \right) \times \left( \frac{1000\mu L}{200\mu L} \right) \times \left( \frac{K}{OD_{600}} \right) \quad (5.2.1)$$

where the terms  $A_{550}$ ,  $OD_{600}$  and  $K$  indicate the optical absorption values of the cultures, at the wavelength of 550 nm, the optical density at the wavelength of 600 nm (per milliliter) and the dilution rate of the *S. aureus* samples, respectively. The formazan dissolution, related to the cellular metabolic activities, was tracked collecting the absorbance values at 500 nm ( $A_{550}$ ) of formazan crystals formed within the 20 min of the reaction. Moreover, 200 L is the volume of the *S. aureus* cell dilution, and 220 L is the total volume of the mixture of 200 L of cell and 20 L of MTT stock. The presence of  $Fe_2O_3$  nanoparticles (in absence of *S. aureus* culture) do not interfere with the MTT assay, as indicated by the optical absorption value acquired on the  $Fe_2O_3$  nanoparticles incubated only with the medium (data not shown).

In Fig. 5.14a are shown the optical density values at 600 nm ( $OD_{600}$ ) of *Staphylococcus aureus* in MHB medium, supplemented with  $H_2O$  in  $Fe_2O_3$  and in PVA. No differences during the growth phase between  $Fe_2O_3$  in water,  $Fe_2O_3$  in PVA and in control sample is observed by the optical density value of the cultures.

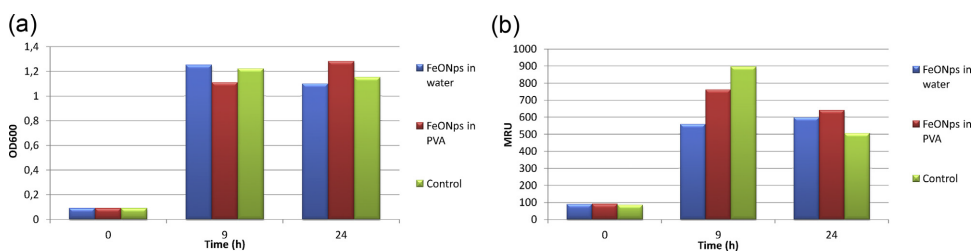


Figure 5.14: (a) Optical density at 600 nm ( $OD_{600}$ ) of *Staphylococcus aureus* in MHB medium supplemented with  $Fe_2O_3$  in  $H_2O$  and in PVA; (b) MTT reduction unit (MRU) of *Staphylococcus aureus* in MHB medium supplemented with  $Fe_2O_3$  in  $H_2O$  and in PVA.

However, the respiratory activity of the cultures treated with iron nanoparti-

cles in water and PVA is different, as observed by the absolute values of *S. aureus* MTT reduction unit (MRU) in MHB medium supplemented with Fe<sub>2</sub>O<sub>3</sub> nanocolloids. MRU values as a function of time are shown in Fig. 5.14b. After 9h of incubation, MRU values are significantly lower in the solution with Fe<sub>2</sub>O<sub>3</sub> in water respect to the control sample. On the other hand, PVA-Fe<sub>2</sub>O<sub>3</sub> solution has a minimum effect on *S. aureus* growth. Thus, the presence of PVA does not induce an additional toxic effect of bacteria growth in comparison to what reported in literature [159, 160]. After 24h, MRU values are not statistically different in all tested samples, indicating that the antibacterial activity of the water-Fe<sub>2</sub>O<sub>3</sub> nanocolloids is partial. Furthermore, we outline that, for the water prepared sample, no significant MRU values differences occur between 9h and 24h while, in the control and PVA prepared samples, a decrement of the MRU values is evident at around 24h (see Fig. 5.14b). This behaviour is explained taking into account the bacterial culture is in a stationary growth phase in which the respiratory activities are reduced.

On the overall, iron oxide nanoparticles prepared by pulsed laser ablation in water show a partial bactericidal effect on *Staphylococcus aureus*. Conversely, a minimum effect is observed for the bacterial growth in the PVA-Fe<sub>2</sub>O<sub>3</sub> nanocolloids. This behaviour could be due to the Fe<sub>2</sub>O<sub>3</sub> nanoparticles surface properties given by the polymeric matrix around the single distributed iron oxide particles

### 5.2.2 Silibinin release in response to light source and magnetic field

The release experiments were performed with the membranes and the corresponding colloidal solutions, following the procedure described previously. In order to assess the magnetic-responsive drug-release behavior, the PEG-PLGA/SLB@Au\_Fe<sub>2</sub>O<sub>3</sub>-PVA or PEG-PLGA/SLB@Ag\_Fe<sub>2</sub>O<sub>3</sub>-PVA scaffolds were subjected to alternating current magnetic fields (ACMF, 200 KHz). When the field was applied, the temperature was monitored using a pyrometer placed above the inductor. A reference measurement of the pure solvent (equivalent volume) was subtracted from the data of all the investigated samples.

Fig. 5.15 shows the cumulative release of SLB observed for the irradiated electrospun sample and for the nonirradiated sample, as a function of time.

For comparison, we also report the corresponding data for the colloidal samples before the electrospinning deposition. The drug is released more effectively upon light irradiation in an active and timely manner by the colloidal nanocomposite, as described in Refs. [144, 151], for analogous nanocomposites. Regarding the membrane, a significantly higher percentage of SLB (about 30% vs 10% at about 40 h) is released upon irradiation with respect to the non-irradiated membrane. However, a slow response of the nanofibrous membrane toward the light stimulus is evident, probably due to the Au NPs distribution along the nanofibers.

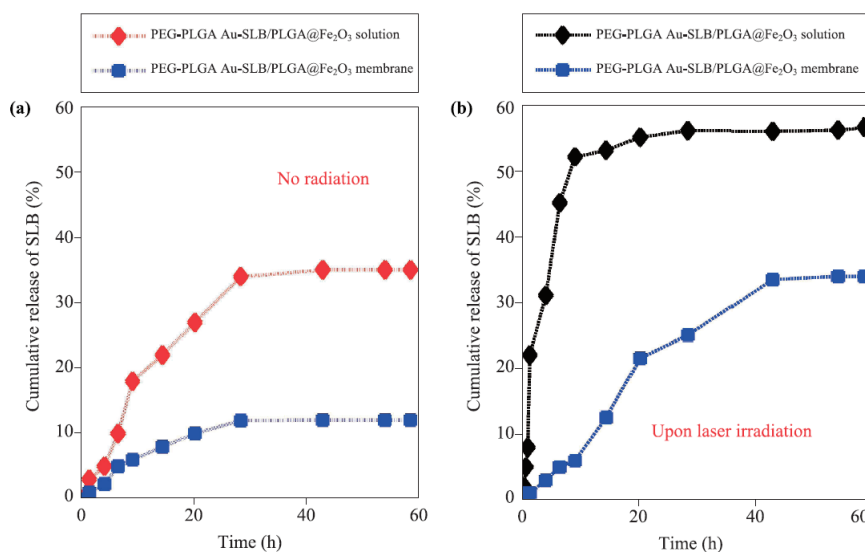


Figure 5.15: Cumulative release of SLB as a function of time.

Moreover, the investigated nanomaterials show interesting sustained responsive drug release induced by a magnetic field. The magnetization curves, acquired at room temperature, for all the investigated samples are shown in Fig. 5.16a. No magnetization is observed in the PEG-PLGA\_Au-SLB/PLGA since no Fe<sub>2</sub>O<sub>3</sub> NPs are present. On the other hand, the magnetization of the PEG-PLGA\_Au-SLB/PLGA@Fe<sub>2</sub>O<sub>3</sub> in the membrane is lower than that of the PEG-PLGA\_Au-SLB/PLGA@Fe<sub>2</sub>O<sub>3</sub> in the corresponding solution. Moreover, no hysteresis loops (near-zero coercivity and remanence) is evident.

In Fig. 5.16b the variation of the temperature as a function of time, in presence of the alternating magnetic field, is reported. Before applying the magnetic

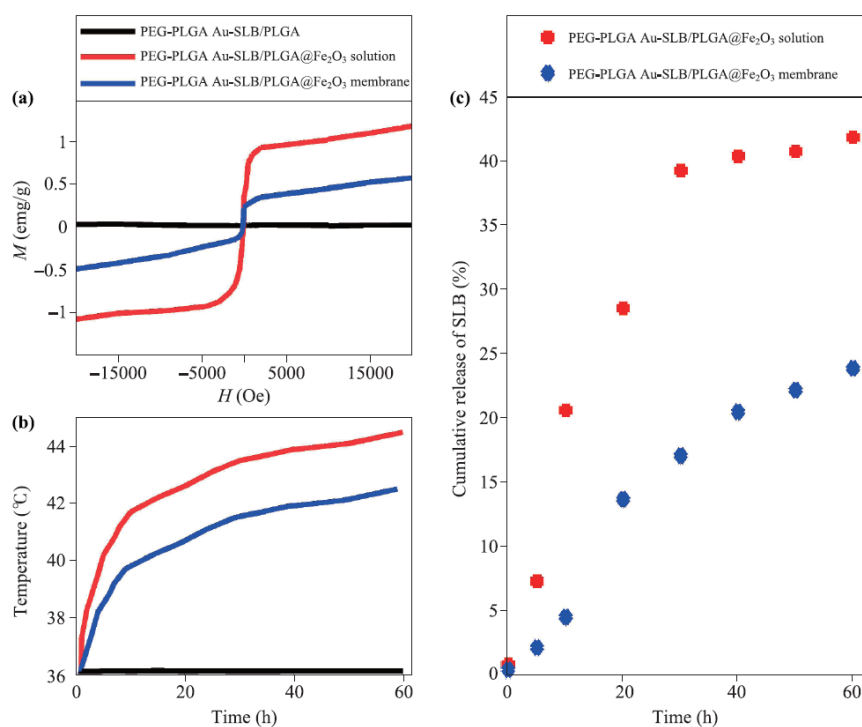


Figure 5.16: Cumulative release of SLB as a function of time.

field, the samples are maintained at 37°C. After 60 h, a temperature of 42°C and 44°C is reached for the solution and membrane, respectively. Under the external magnetic field, an initial fast release (within 20 h) followed by a relatively slow release during the time is observed (see Fig. 5.16c). This behavior confirms that the magnetic field induces heating of the polymeric nanocomposites due to the delay in Neel relaxation of the magnetic moment [161], consequently triggers the release of the drug. All these behaviors are explained by considering the relative contribution of the polymer degradation promoted by the Au@Fe<sub>2</sub>O<sub>3</sub> mediated laser-magnetic irradiation heating effect.

Similar behaviours are shown by the PEG-PLGA/SLB@Ag-Fe<sub>2</sub>O<sub>3</sub>-PVA membranes. Also in this case, iron oxide and Ag nanoparticles were identified and distinguished by energy dispersive X-ray analysis (EDX). Estimated atomic species percentages are: 66.3 % (Carbon), 30.0% (Oxygen), 2.5% (Silver) and 1.2% (Iron). The structure of the iron oxide particles was determined by carry-

ing out XRD spectroscopy measurements. In Fig. 5.17 is shown XRD spectrum of the PEG-PLGA/SLB@Ag<sub>2</sub>O<sub>3</sub>-PVA nanofibrous membrane. All the XRD features exhibit the characteristic pattern of rhombohedral (hexagonal) structure of  $\alpha$ -Fe<sub>2</sub>O<sub>3</sub> (space group: R-3c), with lattice constants of  $a = 0.5034$  nm and  $c = 1.375$  nm (ICDD card no. 33-0664).

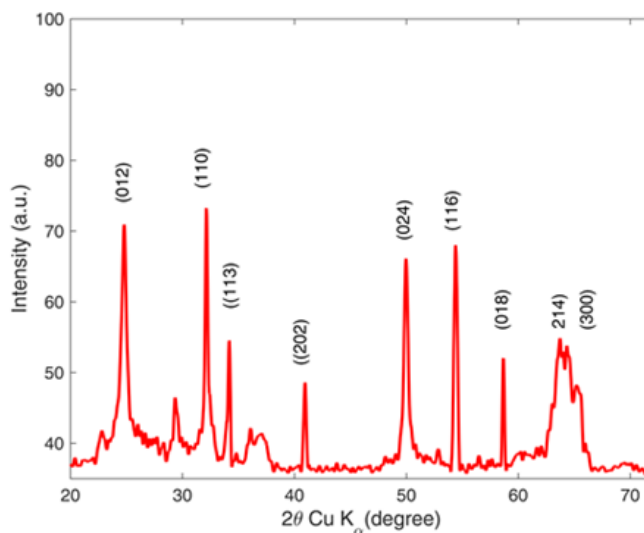


Figure 5.17: XRD spectrum of the PEG-PLGA/SLB@Ag<sub>2</sub>O<sub>3</sub>-PVA nanofibrous membrane. The same iron oxide features was observed for PEG-PLGA/SLB@Au<sub>2</sub>O<sub>3</sub>-PVA nanofibers (not shown).

The nano-SLB drug efficiency release was tested by irradiating the PEG-PLGA/SLB@Ag<sub>2</sub>O<sub>3</sub>-PVA scaffold with the 488 nm (partially transparent to human flesh and tunable with Ag SPR) laser source at the low power density of 21 mW cm<sup>2</sup>, and simultaneously applying an external magnetic field. Fig. 5.18 shows SLB cumulative release as a function of time from the PEG-PLGA/SLB@Ag<sub>2</sub>O<sub>3</sub>-PVA nanofibers irradiated by the 488 nm laser light source and under the external magnetic field. The initial SLB release (within the first 20 h) is due to the diffusion of the drug from the 200 nm sized particles. This mechanism is aided by the Ag-mediated laser irradiation heating effect, making it more effective than the diffusion process, so that a higher percentage of SLB is released upon irradiation within a few hours with respect to the not



irradiated sample and reaching 60% of released drug within 80 h. Furthermore, under the external magnetic field, an initial slow release (within 20 h) followed by a relatively fast release during the time is observed.

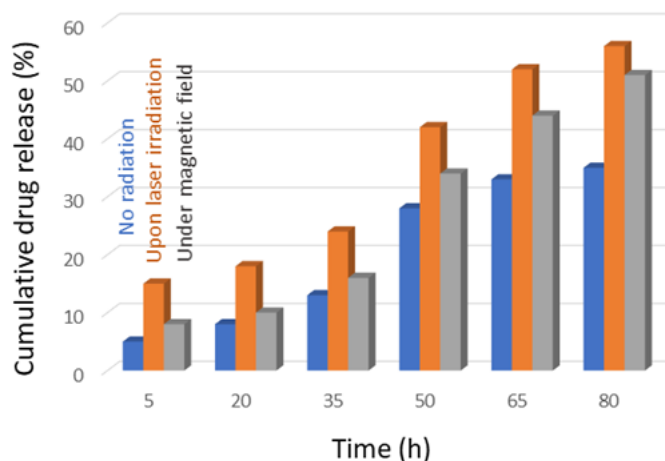


Figure 5.18: SLB cumulative release as a function of time from the PEG-PLGA/SLB@Ag<sub>2</sub>Fe<sub>2</sub>O<sub>3</sub>-PVA nanofibers irradiated by the 488 nm laser light source and under the external magnetic field.

In conclusion, a novel integrated plasmonic-magnetic nanofiber was fabricated and proposed as a remotely triggered nanopatform for the entrapment and delivery of a poorly water-soluble drug. Passive drug diffusion, polymer swelling/degradation, matrix erosion, Ag/Au-mediated laser-irradiation-induced heating effect combined to magnetic one are responsible for the SLB release rate. However, by controlling the mode of encapsulation and the architecture of electrospun fibers, the drug release efficiency of the nanopatform could be further optimized. Thus, the proposed nanovector could be advantageously activated by an external magnetic field, due to the presence of Fe<sub>2</sub>O<sub>3</sub> NPs, and could also be applied for photothermal therapies that make use of visible optical radiation, due to the presence of Au or Ag NPs.

## Chapter 6

# Rhodium oxide nanostructures for hydrogen gas sensors

A sensor is a device that produces a response upon exposure to some stimulus through introducing functionally related output. The response is an alert in one or more of the sensor properties such as mass, electrical conductivity, and capacitance. Specifically, room-temperature (RT) gas sensing is desirable for battery-powered or self-powered instrumentation that can monitor emissions associated with pollution and industrial processes. Among the different topology of sensors, conductometric gas sensors are largely used. A conductometric transducer consists of (i) layer of gas sensitive material, (ii) substrate, (iii) electrodes to measure the electrical signals, and (iv) heater. The contacts could be of Ohmic or Schottky type, and their geometry controls the sensor operational mode. The conductance (or the resistance) of the sensor is dependent on the properties of the sensitive material, the concentration of the target gas and the measurement parameters such as the temperature and applied voltage. The reaction of the target gas with the sensitive material takes place at different sites of the structure, depending on the morphology, and is transduced into electrical signal [162].

In the last years, nanotechnology is enabling the production of efficient sensors with broad range of applications. The unique properties of the nanomaterials make them suitable candidates for sensitive detection of chemical and biological species. In particular, they exhibit great adsorptive capacity due to the large surface-to-volume ratio, produce great modulation of the electrical signal upon exposure to analytes due to the great interaction zone over the cross sectional area (Debye length), enable tuning electrical properties by controlling the composition and the size of the nanomaterial, and ease configuration and integration in low-power microelectronic systems. During the past years, strategies such as metal doping, heterojunction composites, and different morphologies are applied to enhance their sensing characteristics. Particularly, the use of nanoclusters allows the fabrication of an array of sensors in a chip with a good sensitivity towards common target species such as  $H_2$ ,  $O_2$ , and  $CO$ .

The greater surface to-volume ratio, the better stoichiometry, and greater level of crystallinity compared to bulk materials make the newly developed nanocluster gas sensors very promising for better understanding of sensing principles and development of a new generation of sensors. Because of the wide availability of synthesis and processing of nanomaterials, a careful selection of methodology to prepare nanoclusters of sufficiently fine dispersion, porous structure, high crystallinity, and bulk quantity is required. Generally, nanoclusters can be synthesized using different chemical and physical methods with many examples, including (a) physical synthesis such as inert gas condensation, ball milling, laser ablation, and others; (b) chemical synthesis such as sol-gel, chemical reduction, hydrolysis, and others; and (c) biological synthesis that can be established using algae, plant extracts, bacteria and fungi.

Among the synthesized nanomaterials, porous nanostructures, such as oxides of Sn, Ni, Zn, W, In, La, Fe, Co, have shown remarkable potential for RT gas sensing. Due to their low cost, low power consumption and their large surface-to-volume ratio, metal oxide (MO) gas sensors can be utilized for high sensitivity, selective and rapid detection of more than 150 gases [163]. Selectivity, working temperature and long-term stability of course remains a concern for metal and metal-oxide based gas sensor. Despite oxides of noble metals such as Pt, Pd, Rh and Au possess excellent properties, as demonstrated by their large use

in heterogeneous catalysis, only very few applications in gas sensing field have been reported [164, 165, 166]. Further, these applications are almost completely limited to PdO, used for CO and H<sub>2</sub> monitoring [167, 168, 169, 170].

Hence, with the aim to explore the potential of other noble metal oxides as gas-sensing materials, we focused our investigation on rhodium oxides. Generally, Rh forms metastable RhO<sub>2</sub>/Rh<sub>2</sub>O phases and a stable Rh<sub>2</sub>O<sub>3</sub> phase, exhibiting an orthorhombic structure in space group P<sub>bca</sub> [134]. Oxidized rhodium surface species are reported to play a key role in gas sensing mechanism [171]. Rh<sub>2</sub>O<sub>3</sub> nanoparticles have been reported to promote acetone sensing in combination with WO<sub>3</sub> [172], but no report deals with the sensing properties of rhodium oxides toward hydrogen.

Hydrogen sensors are of increasing importance in connection with the development and expanded use of hydrogen gas as an energy carrier in fuel cells, combustion engines and as a chemical reactant [173]. Nowadays, the most promising solid-state technology for hydrogen monitoring is based on palladium-based conductometric sensors. However, several fundamental problems are associated with use of bulk Pd as sensing layer in conductometric platforms. First, the diffusion of the hydrogen into bulk Pd such as a thick Pd film can result in an extraordinary large internal stress, leading to buckling of the films [174]. The consequent deformation leads to an irreversible resistance change. Secondly, the hydrogen atom diffusion in Pd is very slow at room temperature, inevitably leading to a long response time [175]. Progress in nanoresearch has led to the development of H<sub>2</sub> sensors based on Pd nanomaterials, such as nanowires [176]. The utilization of individual Pd nanowires as sensing elements, however, can face challenges in nanofabrication of these small low dimensional nanostructures [177].

On this basis, in this research work, it was tried to explore the potential of preparing nanosized rhodium oxides by a simple method for sensing applications. Actually, the chemical synthetic procedures require toxic reagents and harsh conditions, which limited the control over NPs size and distribution and their applicability only to specific reaction-support combinations [178]. To overcome these drawbacks, an alternative approach is proposed. Rhodium oxide colloids were prepared by pulsed laser ablation in liquid and characterized using

different techniques such as X-Ray photoelectron spectroscopy, X-Ray Diffraction, and micro-Raman spectroscopies. Thus, their gas sensing performances are described and discussed in details, emphasizing the improved characteristics compared with materials produced by conventional synthesis procedures.

### 6.0.1 Rhodium-Rhodium oxide: synthesis and characterization

An aqueous colloidal solution was prepared by using a Nd-YAG laser (wavelength 532 nm, pulse width 5 ns, repetition rate 10 Hz). The laser beam was focused with an incident angle of  $90^\circ$  onto the surface of a high purity (99.9%) rhodium target. All the ablation processes were carried out at the laser fluence of  $2 \text{ J/cm}^2$  and at the irradiation time of 40 min [179].

In Fig. 6.1a, b are shown the STEM image of the nanocolloids and the corresponding size histogram. Nanoparticles having an almost spherical shape and size in the range between 2 and 12 nm, were observed. The composition of the material was determined by SEM-EDX analysis at different points of the deposited film. The results are reported in Fig. 6.1c, d where the EDX map and the corresponding spectrum are shown. By acquiring the micro-EDX map on the surface of the sample, the average surface distribution of Rh and O was estimated to be 45.4 and 54.6%, respectively. No relevant percentage of any other contaminant species was registered. The composition varies slightly from one point of the sample to another point, but is still in good agreement with the XPS data (42% of Rh and 58% of O, respectively).

The morphology of films deposited from the above colloidal aqueous solution, was investigated carrying out SEM measurements. In Fig. 6.2 are shown SEM images, collected on alumina sensor substrate, of the samples before and after the thermal treatment procedure used before sensing tests (annealed in air at  $200^\circ\text{C}$  for 2 h). A porous structure on a nanometric scale can be observed; it is noteworthy that the size and shape of the film constituent are not modified by the annealing process.

As shown in the chapter 4, the metallic rhodium phase is not detected by by micro-Raman and XRD techniques; however, suspecting that it could be present in these samples a XPS analysis has been carried out.

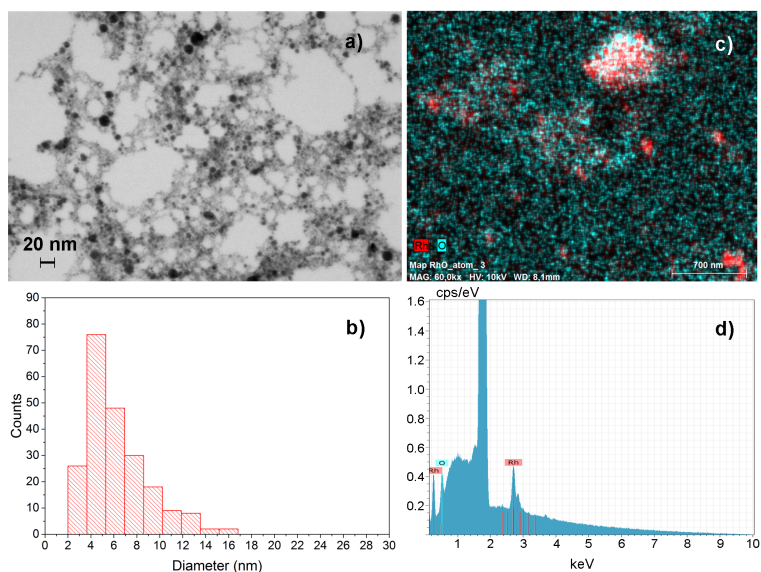


Figure 6.1: (a) and (b) STEM image and size histogram of laser synthesized nanoparticles; (c) and (d) SEM-EDX analysis.

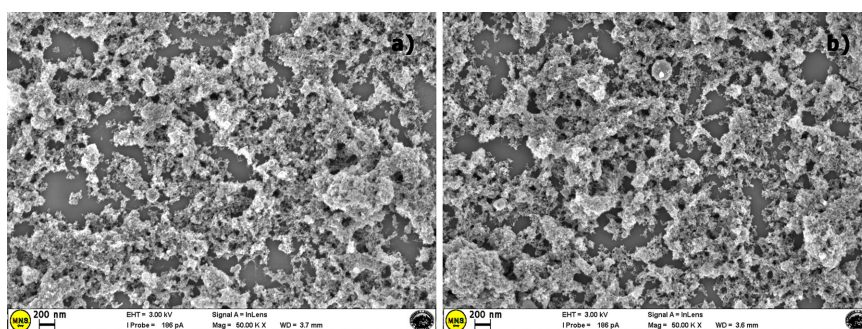


Figure 6.2: SEM images of the samples before (a) and after (b) the annealing process.

Rh 3d XPS high resolution lineshapes are shown in Fig. 6.3. The observed Rh 3d fingerprints on the as prepared colloidal material (Fig. 6.3a) are assigned to the metallic Rh and the oxidized Rh phases centered at about 307.5 eV and 310 eV, respectively [180, 130, 181]. Moreover, to reproduce the data, it was also necessary to add two sub-bands due to metallic and oxide Pt phases, coming presumably from the Pt electrodes of sensor substrates (see Fig. 6.3b, c), and

to normalize the data with respect to Rh and Pt total content, estimated from XPS wide scan spectra. XPS spectrum reported in Fig. 6.3a shows instead that the oxidized Rh phases dominate in the sample annealed in air at 200°C. XPS spectra in Fig. 6.3c indicate clearly that the exposure to pure H<sub>2</sub> atmosphere at 80°C and 100°C alters significantly the XPS Rh 3d profile, being now dominated by the metallic Rh contribution. On the overall, this means that

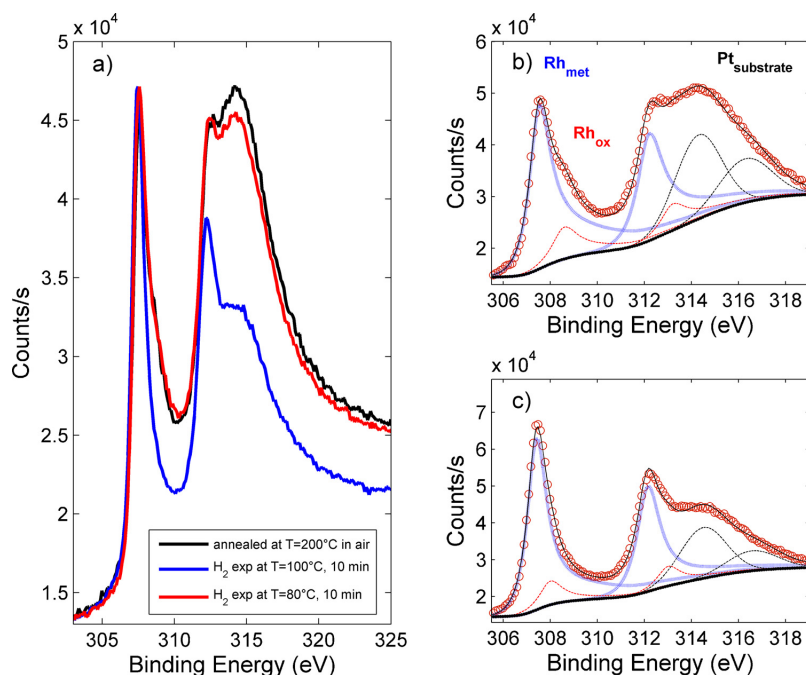


Figure 6.3: XPS Rh 3d lineshapes of the investigated samples (a); Rh 3d fitted profiles of the sample annealed at  $T = 200^{\circ}\text{C}$  in air (b) and that, annealed at  $T = 200^{\circ}\text{C}$  in air, and subsequently exposed at H<sub>2</sub> at  $T = 100^{\circ}\text{C}$  (c).

an easy reduction-oxidation process occurs at mild temperature, likely favored by the nanosized structure of the synthesized particles, in agreement with the well-known characteristics of Rh oxides to undergo reduction at relatively low temperature in reducing atmospheres [182].

## 6.0.2 Electrical and hydrogen sensing properties

The electrical and sensing characteristics of films deposited on conductometric platforms were evaluated as a function of the different annealing temperature

and atmospheres. The as deposited films display a very poor conductivity. Upon increasing the annealing temperature at 200°C in air, the electrical resistance value decreases from hundreds of GΩ to 5 MΩ (see Fig. 6.4). The decrease of resistance can be likely ascribed to the improvement of the crystallinity of the film after the thermal treatment. However, it cannot be excluded that this could be also due to positive charge accumulation at the interface between Rh metal and Rh<sub>ox</sub> phases formed at higher temperature. This latter hypothesis is in agreement with the behavior observed when the oxidized film was treated in pure hydrogen. In fact, as effect of these treatments, a reduction process occurred on the surface of the Rh<sub>ox</sub> film, forming metallic Rh. As a result, the resistance of the film increases significantly. This reversible trend, observed when the Rh/Rh<sub>ox</sub> ratio is modified by changing the treatment temperature and atmosphere, further strengthen the idea that the electrical characteristics of the film deposited are linked to the composition of the film. It seems that an optimal ratio between reduced and oxidized rhodium phases exists, at which the conduction pathway is favored leading to a low resistance.

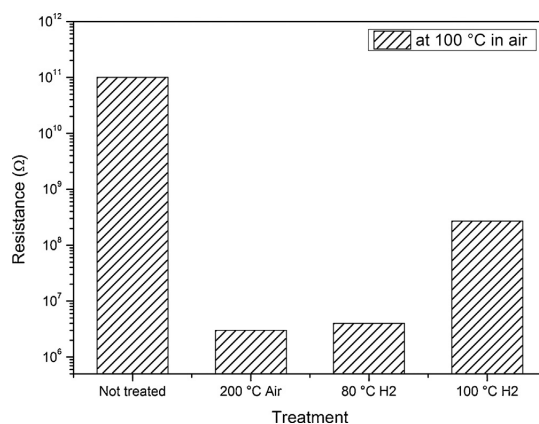


Figure 6.4: Baseline resistance, evaluated at the temperature of 200°C, of the deposited films treated in air/hydrogen at different temperatures.

Hydrogen sensing tests were then carried out with the different treated sensors. Preliminary tests indicated that the device based on the sensing film annealed in air at 200°C is the most responsive. Further, it was noted that a higher sensitivity was obtained working at the temperature of 100°C (see Fig.



6.5a). However, in order to obtain a faster response and signal recovery, we preferred to operate at the working temperature of 200°C. The typical transient response observed at this latter temperature is reported in the inset. The response and recovery times are  $\approx 2$  and  $\approx 5$  min, respectively.

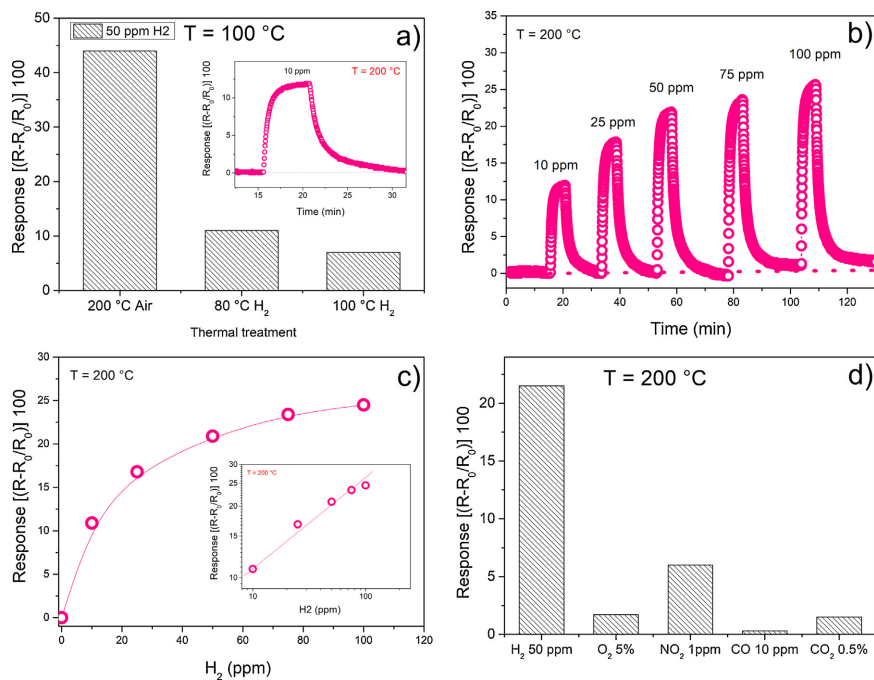


Figure 6.5: a) Response of the sensor to 50 ppm H<sub>2</sub> treated in different conditions at the operating temperature of 100°C; b) Response to H<sub>2</sub> gas pulses, at concentration ranging from 10 ppm to 100 ppm, of the sensing film annealed at 200°C and operated at 200°C; c) Calibration curve; d) Comparison of the sensor response to H<sub>2</sub> and CO, CHO<sub>2</sub>, NO<sub>2</sub> and O<sub>2</sub>.

The long recovery time suggests a strong adsorption of hydrogen on the surface of the sensing layer, so it can be hypothesized that the desorption process of hydrogen from the surface is slower than hydrogen absorption one. The calibration curve, at the operating temperature of 200°C, towards pulses of H<sub>2</sub> at concentration ranging from 10 ppm to 100 ppm, is reported in Fig. 6.5b.

A fully reversible behavior was observed when hydrogen at low concentration was added to a carrier gas passing over the sensor. Additionally it can be seen that the sensor maintains a fairly good stability of the baseline after repeated

cycling. This stability and lack of drift is an important feature that is critical for practical applications. In Fig. 6.5c is reported the calibration curve for this sensor. It can be noted that the sensor is able to detect 10 ppm of hydrogen with a high signal to noise ratio. The linearity in a log-log graph is evidenced in the plot added in the inset.

High selectivity for  $H_2$  gas in the presence of other gaseous species is also very important for practical gas monitoring equipment [183]. As shown in Fig. 6.5d, the sensor response value to  $H_2$  at 50 ppm was much higher than that to other simple gases tested such as CO,  $CO_2$ ,  $NO_2$  and  $HO_2$ . This demonstrates that the interferences from these other gases are negligible, i.e. the sensor has a very good selectivity. In addition, as reported in Fig. 6.6a, the sensor shows a perfect reproducibility of response when exposed to consecutive pulses of the same concentration of hydrogen. This suggests that the annealing treatment at  $200^\circ C$  is enough to stabilize the sensitive film, and such low concentrations of hydrogen are not so critical to induce material modifications. These performances make the sensor comparable to the ones based on PdO and operating in the same conditions [167].

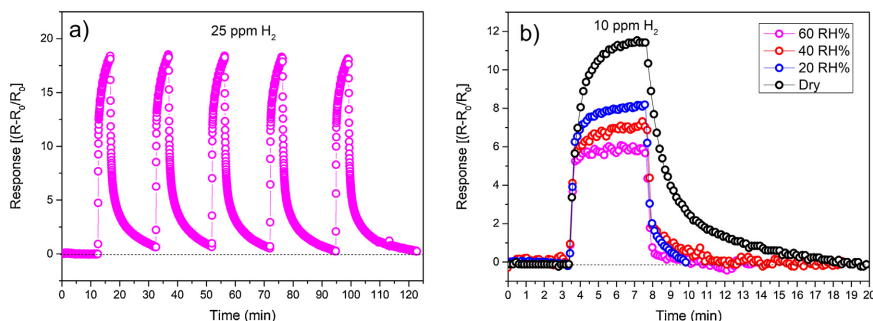


Figure 6.6: a) Response of the sensor to five consecutive pulses of 25 ppm  $H_2$  at operating temperature of  $200^\circ C$ ; b) Effect of different relative humidity (RH) on the response to 10 ppm  $H_2$  at operating temperature of  $200^\circ C$

Despite the above excellent performance, the presence of humidity is a critical factor affecting the response to hydrogen. As observed in Fig. 6.6b, the response to 10 ppm of hydrogen is appreciably reduced from dry to humidity conditions. However, although a continuous decrease of the response was observed upon increasing the relative humidity (RH), the relative variations from 20 to 60 RH% are not as critical as the transition from dry to humid. This effect, which is quite common for gas sensors based on semiconductor metal oxides, is likely due to the dissociative adsorption of water molecules on the surface of material which forming hydroxyl groups, reduces the concentration of active oxygen species mainly involved in the sensing mechanism of hydrogen [184]. Nevertheless, even in the presence of medium-high humidity levels, the sensor is able to show an excellent response to hydrogen concentrations as low as 10 ppm.

Many parameters are known to affect the hydrogen sensing behavior of semiconductor conductometric sensors [185]. Characterization results here reported demonstrated that changing the annealing temperature and atmosphere, no substantial changes in the morphology (shape and size) of the rhodium nanoparticles occurred. Then, these factors cannot be indicated as responsible of the electrical and sensing behavior of our sensors. On the other hand, results reported in this study indicate that the composition of the rhodium nanoparticles influences greatly the electrical characteristics of the deposited sensing film, as well as the sensing properties toward hydrogen. Therefore, we can assume that the change in the chemical composition could be the only factor responsible for the observed sensing behavior toward hydrogen. The commonly accepted hydrogen sensing mechanism with metal oxide-based sensors is based on the variation of the surface electron depletion region due to the reaction between hydrogen and the chemisorbed oxygen on the surface of sensing layer. However, there is not certainty if the main role in the sensing process is played by metal, metal oxide or the metal/metal oxide interface. Pedrero et al. reported that the catalytic dissociation of hydrogen molecules by the PdO particles, which occurs more efficiently than on metallic palladium ones, has been considered to be of primary importance for the response of a palladium film to hydrogen. Chiang and collaborator, suggested that the H<sub>2</sub> sensing behavior of a PdO sen-

sor is strongly affected by PdO reduction at temperatures below 100°C, and is characterized by the kinetic competition between PdO reduction and Pd re-oxidation around 150°C. At temperatures above 200°C, the sensing behavior can be described simply by the oxygen vacancy model [167]. On the basis of these considerations, here is proposed a sensing mechanism operating on Rh/Rh<sub>ox</sub>-based sensors (see Fig. 6.7). Under air atmosphere, the oxygen molecules can get adsorbed on the surface of the sensing film and extracts electrons from the conduction band of Rh oxidized phase to form oxygen ions. This leads to the formation of an electron depletion region near the surface, which can greatly increase the resistance due to the decrease of net carrier density. When the sensor is exposed to H<sub>2</sub>, the target gas molecules will react with the adsorbed oxygen species. The metallic Rh phase is supposed to participate effectively in this step favoring hydrogen dissociation via a spillover mechanism.

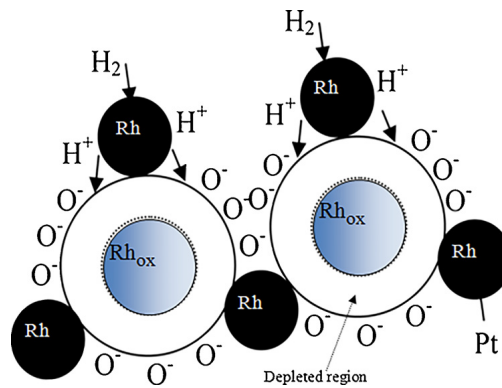


Figure 6.7: Schematic representation of hydrogen sensing mechanisms based on spillover effect over Rh/Rh<sub>ox</sub>-based film

The reaction proceeds with the formation of H<sub>2</sub>O molecules and the release of electrons will reduce the thickness of the depletion region, decreasing the resistance of the sensing layer. When the sensor is again exposed to the air ambient, the depletion region will be rebuilt by adsorbed oxygen species. The resistance will regain the initial level before hydrogen response. It appears that the metal/metal oxide interface plays an important role in this mechanism. On the overall, here a simpler approach providing a general way to prepare new hydrogen sensing materials based on colloidal rhodium oxides nanoparticles is

reported.

By fabricating a simple conductometric platform, the sensing properties of these nanostructures towards low concentration of hydrogen in air is, for the first time, presented and discussed. The sensing properties to hydrogen of the sensor developed can be controlled by an appropriate modulation of the chemical composition of the sensing film, through an annealing procedure carried out at the optimal temperature and atmosphere. Ultimately, the results obtained opens up a promising platform for novel H<sub>2</sub> sensors that can be applied for environmental monitoring, biomedical as well as industrial safety applications. However, further studies are needed for a deeper understanding of the sensing mechanism and a fine control of the compositional and structural properties of these materials in order to optimize the sensing response.

# Appendix A

In this appendix are described the basis of some setup that were used in this thesis work for the synthesis and characterization of nanostructures.

## A.1 Laser Ablation Setup

Pulsed laser ablation of high purity (99.9%) Ag and Au solid targets in deionized water ( $\text{H}_2\text{O}$ ) was carried out using the second harmonic (532 nm) of a laser operating at 100 KHz repetition rate with pulse width of 6-8 ps. The target was irradiated with laser powers of 1.5 W and 4.5 W. The laser beam was focused to a spot of about 80  $\mu\text{m}$  in diameter on the surface of the target with a galvanometric scanner. The target surface was scanned on a  $10 \times 10 \text{ mm}^2$  area with a scan speed of 800 mm/s. In Fig. A.8 is shown the scheme of both ns- and ps-pulsed laser ablation setup and a detail of the raster-scan pattern made during the ablation process.

For ns-PLAL a Nd:YAG laser with 10Hz repetition rate, 5ns pulse length, 6 mm beam radius and 532 nm emission wavelength have been used. The geometry adopted is showed in Fig. A.8. In this case the focus have been done by means of a focussing lens and the target rotate by means of an electric engine.

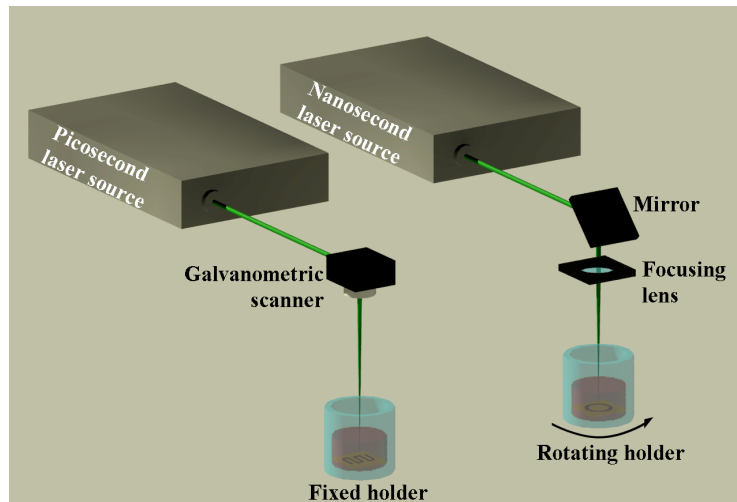


Figure A.8: Scheme of the used PLAL setup with picosecond and nanosecond laser.

## A.2 Aerography setup

The aerography spraying technique is used to transfer the colloidal nanoparticles onto different materials substrates. The system is made up by an ultrasonic atomizer with interchangeable nozzles of different sizes. The spraying is carried out in a deposition chamber equipped with a heated substrate holder and an excess vapors removal system to guarantee standard and reproducible conditions. The substrate holder is positioned onto a xy translation stage which is continuously moved during the spraying to ensure an uniform nanoparticles distribution on the substrate.

## A.3 Electrospinning setup

Electrospinning is a simple and versatile top-down method for generating ultrathin fibers from a wide range of materials, including polymers, composites, and ceramics, by applying electric shear stress. During electrospinning, the polymer solution, which is typically highly viscous, is forced through a spinneret by a syringe pump and then subjected to a strong electric field (Fig. A.9). The resultant liquid jet evaporates under a controlled temperature and humidity, and

the remaining semi-solid polymer fiber is deposited onto a collector. The fluid emission speed from the needle varies in the 2-200 m/s range, depending on the physical properties of solution and processing conditions . This method produces non-woven membranes with individual fiber diameters typically ranging from 50 to 500 nm [155].

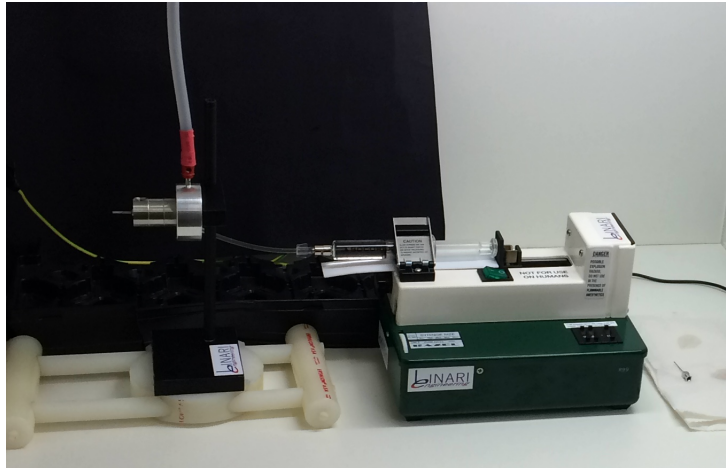


Figure A.9: Picture of the electrospinning setup used for the realization of nanofiber.

## A.4 Raman Spectroscopy

Raman spectroscopy is a technique that, collecting the light diffused from a sample, can give information regarding vibration modes of the molecules that form the sample. The technique consist in the illumination of a sample with monochromatic light of frequency  $\omega_0$  that lead to energetic transitions (vibrational or electronical). After this transition, the system will emit a photon in order to release the energy absorbed. An huge part of this light will have the same frequency  $\omega_0$  of the incident light (Scattering Rayleigh), but there is a small fraction that will have a frequency  $\omega_i$  such that  $\Delta_E = h(\omega_0 - \omega_i)$ .

Raman scattering experiments were performed using three different setup:

- a micro-Raman apparatus with an exciting wavelength of 532 and 785 nm from a 10 mW diode laser focused onto the sample surface by means of an



Olympus BX 40 microscope equipped with a 50 and 100 X objective. The latter was also used to collect the backscattered radiation that was analyzed by an XploRA monochromator and sent to a cooled charge-coupled device detector. Raman spectra were carried out on samples deposited onto glass substrate in order to exclude any contribution of the sensor substrate to the observed rhodium features.

- an FT-Raman measurements were carried out with a Nicolet NXR9650 instrument equipped with a solid-state Nd-YVO<sub>4</sub> laser providing the excitation wavelength of 1064 nm with the laser power at the sample of about 1.4 W, on a spot of 50  $\mu\text{m}$  diameter. To test the SERS activity of Au NPs produced by ps-PLAL, a fraction of the colloids was ultrasonically sprayed on (100) Si supports.
- a micro-Raman Labram HR800 instrument (Horiba-Jobin Yvon) equipped with a 785 nm solid-state laser XTRA T optica Photonics with the laser power at the sample of about 5 mW was used to carry out SERS measurements. The beam was focused by a 50X objective of an Olympus BX41 microscope in a spot of about 1  $\mu\text{m}$  diameter.

## A.5 X-ray Photoelectron Spectroscopy

X-ray Photoelectron Spectroscopy (XPS) allows to have quantitative information about the composition of the film surface.

XPS measure the energy distribution of electron that are emitted from atoms and molecules core levels. In particular, when a material is irradiated with X-Ray photoelectron are emitted with an energy equal to the difference between the one of the incident photon  $h\nu$  and the ionization energy of the atom  $E_{ion}$ :

$$K_E = h\nu - E_{ion} \quad (\text{A.5.1})$$

Moreover, the binding energy measured in this way changes by few eV in relation with the atoms bonds (this effect is known as chemical shift). In this way is possible to evaluate both the elemental atom percentage in the samples and their bond configuration.

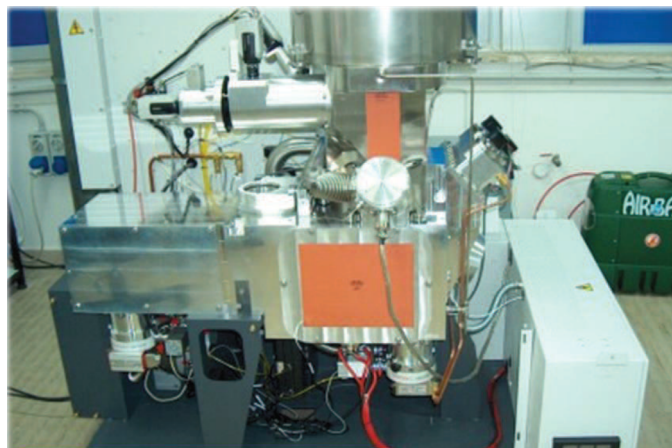


Figure A.10: XPS equipment located in the laboratories of the University of Messina, Italy

XPS was carried out in ultra-high-vacuum condition (about  $1.33 \cdot 10^{-7}$  Pa) using a Thermo Scientific Instrument (see Figure A.10) equipped with a monochromatic Al  $K\alpha$  source ( $h\nu = 1486.6$  eV) and a hemispherical analyzer (spherical sector  $180^\circ$ ). The constant-pass energy was set at 200 eV for survey scans and at 50 eV for the XPS high resolution spectra. Being a surface technique, XPS is able to probe only a few monolayers. Hence, to estimate the composition of the layers in depth, it was necessary to progressively remove the surface layer using a scanning 3 KeV Ar<sup>+</sup> ion gun, with a raster area of about  $4\text{mm} \times 2\text{mm}$

## A.6 SEM/STEM Microscopy

The Scanning Electron Microscopy is a characterization technique based on the interaction between the electron beam and the sample generate other electrons, depending from the surface topography, that are acquired from several detector (see Fig. A.11b) allowing the formation of images.

The morphology, size and particle size distribution were investigated by Scanning Transmission Electron Microscopy (STEM) and Scanning Electron Microscopy (SEM), acquired at an accelerating voltage of 30 kV and 3 kV respectively, and at a working distance of 4 mm. SEM apparatus is coupled with an EDX spectrometer to carry out energy dispersive X-ray (EDX) mapping

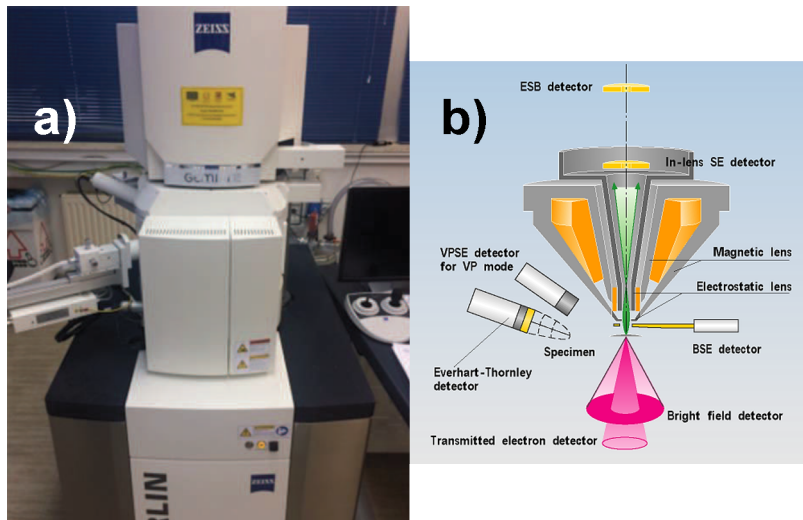


Figure A.11: SEM/STEM equipment used in this thesis work(a) and geometry of detector inside the SEM (b).

analysis. The EDX detected pear-shaped dimension is about  $0.7 \mu\text{m}$ .

# Bibliography

- [1] M.P. Pileni. Reverse micelles as microreactors. *J. Phys. Chem.*, 97 (27):6961–6973, 1993.
- [2] M.P. Pileni. Nanosized particles made in colloidal assemblies. *Langmuir*, 13 (13):3266–3276, 1997.
- [3] AA VV. *Nanoscience and nanotechnologies: opportunities and uncertainties*. The Royal Society, London, 2004.
- [4] N. Chaurasia. Nanotechnology and nanomaterials in everyday life. *International Journal of Science and Research*, 6 (4):1560–1562, 2015.
- [5] Carmen Streich. *Laser-Synthesized Bioconjugated Noble Metal Nanoparticles - Rational Design and Efficacy against Pathological Protein Aggregation*. Ph.d thesis, University of Duisburg-Essen, 2017.
- [6] E. Serrano, G. Rus, and J. García-Martínez. Nanotechnology for sustainable energy. *Renewable and Sustainable Energy Reviews*, 13 (9):2373–2384, 2009.
- [7] W. Lu and C. M. Lieber. Nanoelectronics from the bottom up. *Nat. Mater.*, 6:841–850, 2007.
- [8] P.G. Tratnyek and R.L. Johnson. Nanotechnologies for environmental cleanup. *Nano Today*, 1:44–48, 2006.
- [9] S.K. Sahoo, S. Parveen, and J.J. Panda. The present and future of nanotechnology in human health care. *Nanomedicine : nanotechnology, biology, and medicine*, 3:20–31, 2007.

- [10] I. Khan, K. Saeed, and I. Khan. Nanoparticles: Properties, applications and toxicities. *Arabian Journal of Chemistry*, 2017.
- [11] C. Binns. *Introduction to Nanoscience and Nanotechnology*. John Wiley & Sons, 2010.
- [12] R.L. Johnston. *Atomic and Molecular Clusters*. Taylor and Francis, 2002.
- [13] A.W. Adamson and A.P. Gast. *Physical Chemistry of Surfaces*. John Wiley and Sons, New York, 1997.
- [14] D.A. Walker, B. Kowalczyk, M.O. de la Cruz, and B.A. Grzybowski. Electrostatics at the nanoscale. *Nanoscale*, 3 (4):1316, 2011.
- [15] R. Landauer. Electrical resistance of disordered one dimensional lattices. *Philos. Mag.*, 21 (172):863–867, 1970.
- [16] R. Vajtai. *Springer Handbook of Nanomaterials*. Springer-Verlag Berlin, 2013.
- [17] S.M. Lindsay. *Introduction to Nanoscience*. New York: Oxford University Press, 2009.
- [18] A.P. Alivisatos. Semiconductor clusters, nanocrystals, and quantum dots. *Science*, 271 (5251):933–937, 1996.
- [19] N.J. Halas, S. Lal, W.S. Chang, S. Link, and P. Nordlander. Plasmons in strongly coupled metallic nanostructures. *Chem. Rev.*, 111 (6):3913–3961, 2011.
- [20] S.A. Maier. *Plasmonics: Fundamental and Applications*. New York: Springer, 2007.
- [21] M.A. Garcia. Corrigendum: Surface plasmons in metallic nanoparticles: fundamentals and applications. *Journal of Physics D: Applied Physics*, 45:389501, 2012.
- [22] S. Navalón and H. García. Nanoparticles for catalysis. *Nanomaterials*, 6:123, 2016.

- [23] N. Rajput. Methods of preparation of nanoparticles - a review. *International Journal of Advances in Engineering and Technology*, 7 (4):1806–1811, 2015.
- [24] R. Nagarajan and T.A. Hatton Hatton. *Nanoparticles: synthesis, stabilization, passivation, and functionalization*. ACS Symposium Series 996, American Chemical Society, Washington, DC, 2008.
- [25] Abdel Salam Hamdy Makhlouf and Ahmed Barhoum. *Emerging Applications of Nanoparticles and Architectural Nanostructures: Current Prospects and Future Trends*. Micro and Nano Technologies, 2018.
- [26] Guozhong Cao. *Nanostructures and nanomaterials: Synthesis, Properties and Applications*. Imperial College Press, 2004.
- [27] Maria Chiara Spadaro. *Metal/Oxide Nanoparticles: from assembly and fine structural analysis to magnetic, catalytic and plasmonic properties*. Ph.d thesis, Università degli studi di modena e reggio emilia, 2015/2016.
- [28] F. Neri, P.M. Ossi, and S. Trusso. Cluster synthesis and assembling in laser generated plasmas. *La Rivista del Nuovo Cimento*, 34:104, 2010.
- [29] M.C. Spadaro, E. Fazio, F. Neri, P.M. Ossi, and S. Trusso. On the influence of the mass ablated by a laser pulse on thin film morphology and optical properties. *Applied Physics A*, 1:137–142, 2014.
- [30] M.C. Spadaro, E. Fazio, F. Neri, P.M. Ossi, and S. Trusso. On the role of the ablated mass on the propagation of a laser-generated plasma in an ambient gas. *Europhysics Letters*, 109 (2):25002, 2015.
- [31] Y.B. Zel'dovich and Y.P. Raizer. *Physics of Shock Waves and High Temperature Hydrodynamic Phenomena*. New York: Academic Press, 1966.
- [32] Z. Yan and D.B. Chrisey. Pulsed laser ablation in liquid for micro-/nanostucture generation. *Journal of Photochemistry and Photobiology C: Photochemistry Reviews*, 13:204–223, 2012.
- [33] M. Dell’Aglia, R. Gaudisio, O. De Pascale, and A. De Giacomo. Mechanisms and processes of pulsed laser ablation in liquids during nanoparticle production. *Appl. Surf. Sci.*, 348:4–9, 2015.

- [34] A.M. Morales and C.M. Lieber. A laser ablation method for the synthesis of crystalline semiconductor nanowires. *Science*, 279:208, 1998.
- [35] D. Zhang and B. Gökce. Perspective of laser-prototyping nanoparticle-polymer composites. *Appl. Surf. Sci.*, 392:991–1013, 2017.
- [36] D. Zhang, B. Gökce, and S. Barcikowski. Laser synthesis and processing of colloids: Fundamentals and applications. *Chem. Rev.*, 117:3990–4103, 2017.
- [37] D.B. Chrisey and G.K. Hubler. *Pulsed Laser Deposition of Thin Films*. John Wiley & Sons, New York, 1994.
- [38] V. Amendola and M. Meneghetti. Laser ablation synthesis in solution and size manipulation of noble metal nanoparticles. *Physical Chemistry Chemical Physics*, 11:3805–3821, 2009.
- [39] R. Streubel, G. Bendt, and B. Gökce. Pilot-scale synthesis of metal nanoparticles by high-speed pulsed laser ablation in liquids. *Nanotechnology*, 27:205602, 2016.
- [40] S. Ibrahimkutty, P. Wagener, T. Dos Santos Rolo, D. Karpov, A. Menzel, S. Baumbach, T. and Barcikowski, and A. Plech. hierarchical view on material formation during pulsed-laser synthesis of nanoparticles in liquid. *Scientific Reports*, 5:16313, 2015.
- [41] V. Amendola and M. Meneghetti. What controls the composition and the structure of nanomaterials generated by laser ablation in liquid solution? *Physical Chemistry Chemical Physics*, 15:3027, 2013.
- [42] H. Zeng, X. Wen Du, S.C. Singh, S.A. Kulinich, S. Yang, J. He, and W. Cai. Nanomaterials via laser ablation/irradiation in liquid: A review. *Adv. Funct. Mater.*, 22:1333–1353, 2012.
- [43] M. Hashida, H. Mishima, S. Tokita, and S. Sakabe. Non-thermal ablation of expanded polytetrafluoroethylene with an intense femtosecond-pulse laser. *Opt. Express*, 17:13116, 2009.

- [44] P. Schaaf. *Laser Processing of Materials: Fundamentals, Applications and Developments*. Springer, 2010.
- [45] M. Von Allmen and A. Blatter. *Laser-Beam Interactions with Materials*. Springer, Berlin, 1998.
- [46] N.W. Ashcroft and N.D. Mermin. *Solid State Physics*. Saunders College, Philadelphia, 1976.
- [47] D. Pines and P. Nozières. *The Theory of Quantum Liquids*. Benjamin, New York, 1966.
- [48] P.B. Allen. Theory of thermal relaxation of electrons in metals. *Phys. Rev. Lett.*, 59:1460, 1987.
- [49] P.B. Allen. Empirical electron-phonon  $\lambda$  values from resistivity of cubic metallic elements. *Phys. Rev. Lett. B*, 36:2920, 1987.
- [50] S.I. Anisimov, B.L. Kapeliovich, and T.L. Perel'man. Electron emission from metal surfaces exposed to ultrashort laser pulses. *Sov. Phys. JETP*, 39:375, 1975.
- [51] R. Sprik, R.H.M. Groeneveld, and A. Lagendijk. Femtosecond spectroscopy of electron-electron and electron-phonon energy relaxation in ag and au. *Phys. Rev. B*, 57:11433, 1995.
- [52] M. Vicaneck, B. Rethfeld, A. Kaiser, and G. Simon. Ultrafast dynamics of nonequilibrium electrons in metals under femtosecond laser irradiation. *Phys. Rev. B*, 65:214303, 2002.
- [53] M.N.R. Ashfold, F. Claeysens, G.M. Fuge, and S.J. Henley. Pulsed laser ablation and deposition of thin films. *Chem. Soc. Rev.*, 33:23–31, 2004.
- [54] P.S. Liu, W.P. Cai, and H.B. Zeng. Fabrication and size-dependent optical properties of feo nanoparticles induced by laser ablation in a liquid medium. *J. Phys. Chem. C*, 112:3261, 2008.
- [55] K.Y. Niu, J. Yan, S.A. Kulinich, J. Sun, H. Li, and X.W. Du. Morphology control of nanostructures via surface reaction of metal nanodroplets. *J. Am. Chem. Soc.*, 132:9814, 2010.



- [56] S. Chakraborty, H. Sakata, E. Yokoyama, M. Wakaki, and D. Chakravorty. Laser-induced forward transfer technique for maskless patterning of amorphous  $V_2O_5$  thin film. *Appl. Surf. Sci.*, 254:638, 2007.
- [57] E. Fazio, F. Neri, P.M. Ossi, N. Santo, and S. Trusso. Growth process of nanostructured silver films pulsed laser ablated in high-pressure inert gas. *Applied Surface Science*, 255:9676–9679, 2009.
- [58] R. Messier, A.P. Giri, and R. Roy. Growth process of nanostructured silver films pulsed laser ablated in high-pressure inert gas. *Revised structure zone model for thin film physical structure*, 2:500, 1984.
- [59] S.I. Anisimov, B.S. Luk'yanchuk, and A. Luches. An analytical model for three-dimensional laser plume expansion into vacuum in hydrodynamic regime. *Appl. Surf. Sci.*, 96-98:24–32, 1996.
- [60] P.R. Willmott and J.R. Huber. Pulsed laser vaporization and deposition. *Rev. Mod. Phys.*, 72:315, 2000.
- [61] E. Fazio, F. Neri, P.M. Ossi, N. Santo, and S. Trusso. Ag nanocluster synthesis by laser ablation in ar atmosphere: A plume dynamics analysis. *Laser and Particle Beams*, 27:281–290, 2009.
- [62] D.B. Geohegan. Fast intensified-ccd photography of  $YBa_2Cu_3O_{7-x}$  laser ablation in vacuum and ambient oxygen. *Appl. Phys. Lett.*, 60:2732–2734, 1992.
- [63] A. De Giacomo, M. Dell'Aglio, R. Gaudioso, S. Amoruso, and O. De Pascale. Effects of the background environment on formation, evolution and emission spectra of laser-induced plasmas. *Spectrochimica Acta Part B: Atomic Spectroscopy*, 78:1–19, 2012.
- [64] A. De Giacomo, M. Dell'Aglio, O. De Pascale, R. Gaudioso, V. Palleschi, C. Parigger, and A. Woods. Plasma processes and emission spectra in laser induced plasmas: A point of view. *Spectrochimica Acta Part B: Atomic Spectroscopy*, 100:180–188, 2014.
- [65] P.P. Patil, D.M. Phase, S.A. Kulkarni, S.V. Ghaisas, S.K. Kulkarni, S.M. Kanetkar, S.B. Ogale, and V.G. Bhide. Pulsed-laser-induced reactive

- quenching at liquid-solid interface: Aqueous oxidation of iron. *Phys. Rev. Lett.*, 58:238, 1987.
- [66] H.W. Kang, H. Lee, and A.J. Welch. Laser ablation in a liquid-confined environment using a nanosecond laser pulse. *J. Appl. Phys.*, 103:083101, 2008.
- [67] Z.J. Yan, R.Q. Bao, Y. Huang, A.N. Caruso, S.B. Qadri, C.Z. Dinu, and D.B. Chrisey. Excimer laser production, assembly, sintering, and fragmentation of novel fullerene-like permalloy particles in liquid. *J. Phys. Chem. C*, 114:3869, 2010.
- [68] S. Kohsakowski, B. Gökce, R. Tanabe, P. Wagener, A. Plech, Y. Ito, and S. Barcikowski. Target geometry and rigidity determines laser-induced cavitation bubble transport and nanoparticle productivity - a high-speed videography study. *Phys.Chem.Chem.Phys.*, 18:16585, 2016.
- [69] A. De Giacomo, M. Dell’Aglia, A. Santagata, R. Gaudiuso, O. De Pascale, P. Wagener, G. C. Messina, G. Compagnini, and S. Barcikowski. Cavitation dynamics of laser ablation of bulk and wire-shaped metals in water during nanoparticles production. *Phys.Chem. Chem. Phys.*, 15:3083, 2013.
- [70] M.S. Plesset and A. Prosperetti. Bubble dynamics and cavitation. *Annu. Rev. Fluid. Mech.*, 9:145, 1977.
- [71] R. Petkovšek and P. Gregorčič. A laser probe measurement of cavitation bubble dynamics improved by shock wave detection and compared to shadow photography. *Journal of Applied Physics*, 102:044909, 2007.
- [72] J. Lam, J. Lombard, C. Dujardin, G. Ledoux, S. Merabia, and D. Amans. Dynamical study of bubble expansion following laser ablation in liquids. *Applied Physics Letters*, 108:074104, 2016.
- [73] F. Gilmore. The growth or collapse of a spherical bubble in a viscous compressible liquid. *Technical Report No. 26-4 California Institute of Technology*, 1952.
- [74] K.L. De Graaf, I. Penesis, and P.A. Brandner. Comparison of the rayleigh–plesset and gilmore equations and additional aspects for the

- modelling of seismic airgun bubble dynamics. *18th Australasian Fluid Mechanics Conference*, 2012.
- [75] M. Lau. *Laser Fragmentation and Melting of Particles*. Springer Fachmedien Wiesbaden, 2016.
- [76] D. Zhang, M. Lau, S. Lu, S. Barcikowski, and B. Gökce. Germanium sub-microspheres synthesized by picosecond pulsed laser melting in liquids: Educt size effects. *Scientific Reports*, 7:40355, 2017.
- [77] K. Kawasoe, Y. Ishikawa, N. Koshizaki, T. Yano, O. Odawara, and H. Wada. Preparation of spherical particles by laser melting in liquid using tin as a raw material. *Appl. Phys. B*, 119:475–483, 2015.
- [78] S. Reich, P. Schönfeld, P. Wagener, A. Letzel, S. Ibrahimkuty, B. Gökce, S. Barcikowski, A. Menzel, T. dos Santos Rolo, and A. Plech. Pulsed laser ablation in liquids: Impact of the bubble dynamics on particle formation. *J. Colloid. Interface Sci.*, 489:106–113, 2017.
- [79] A. Letzel, B. Gökce, P. Wagener, S. Ibrahimkuty, A. Menzel, A. Plech, and S. Barcikowski. Size quenching during laser synthesis of colloids happens already in the vapor phase of the cavitation bubble. *J. Phys. Chem. C*, 121:5359–5365, 2017.
- [80] S. Kohsakowski, A. Santagata, M. Dell’Aglio, A. de Giacomo, S. Barcikowski, P. Wagener, and B. Gökce. High productive and continuous nanoparticle fabrication by laser ablation of a wire-target in a liquid jet. *Applied Surface Science*, 403:487–499, 2017.
- [81] S. Scaramuzza, M. Zerbetto, and V. Amendola. Synthesis of gold nanoparticles in liquid environment by laser ablation with geometrically confined configurations: Insights to improve size control and productivity. *J. Phys. Chem. C*, 120:9453–9463, 2016.
- [82] J. Feng, G. Biskos, and A. Schmidt-Ott. Toward industrial scale synthesis of ultrapure singlet nanoparticles with controllable sizes in a continuous gas-phase process. *Sci Rep.*, 5:15788, 2015.

- [83] G.M. Hale and M.R. Query. Optical constants of water in the 200-nm to 200- $\mu\text{m}$  wavelength region. *Applied Optics*, 12:555–563, 1973.
- [84] R. Tanabe, T.T.P. Nguyen, T. Sugiura, and Y. Ito. Bubble dynamics in metal nanoparticle formation by laser ablation in liquid studied through high-speed laser stroboscopic videography. *Appl. Surf. Sci.*, 351:327–331, 2015.
- [85] C.-Y. Shih, R. Streubel, J. Heberle, A. Letzel, M.V. Shugaev, C. Wu, M. Schmidt, B. Gökce, S. Barcikowski, and L.V. Zhigilei. Two mechanisms of nanoparticle generation in picosecond laser ablation in liquids: the origin of the bimodal size distribution. *Nanoscale*, 10:6900–6910, 2018.
- [86] S. Reich, P. Schönfeld, A. Letzel, S. Kohsakowski, M. Olbinado, B. Gökce, S. Barcikowski, and A. Plech. Fluence threshold behaviour on ablation and bubble formation in pulsed laser ablation in liquids. *ChemPhysChem*, 18:1084–1090, 2017.
- [87] S. Reich, P. Schönfeld, P. Wagener, A. Letzel, S. Ibrahimkuty, B. Gökce, S. Barcikowski, A. Menzel, T. dos Santos Rolo, and A. Plech. Pulsed laser ablation in liquids: Impact of the bubble dynamics on particle formation. *Journal of Colloid and Interface Science*, 489:106–113, 2017.
- [88] V. Kononenko, V.I. Konov, S.V. Garnov, S.M. Klimentov, and F. Dausinger. Dynamics of deep short pulse laser drilling: Ablative stages and light propagation. *Laser Phys.*, 11:343–351, 2001.
- [89] C.L. Sajti, R. Sattari, B.N. Chichkov, and S. Barcikowski. Gram scale synthesis of pure ceramic nanoparticles by laser ablation in liquid. *The Journal of Physical Chemistry C*, 114:2421–2427, 2010.
- [90] T.T.P. Nguyen, R. Tanabe, and Y. Ito. Effects of an absorptive coating on the dynamics of underwater laser-induced shock process. *Applied Physics A*, 116:1109–1117, 2014.
- [91] J. Tomko, J.J. Naddeo, R. Jimenez, Y. Tan, M. Steiner, J.M. Fitz-Gerald, D.M. Bubb, and S.M. O’Malley. Size and polydispersity trends found in

- gold nanoparticles synthesized by laser ablation in liquids. *Phys. Chem. Chem. Phys.*, 17:16327–16333, 2015.
- [92] W.C. Hinds. *Aerosol technology : properties, behavior, and measurement of airborne particles*. Wiley, New York, 1999.
- [93] R.P. Carney, J.Y. Kim, H. Qian, R. Jin, H. Mehenni, F. Stellacci, and O.M. Bakr. Determination of nanoparticle size distribution together with density or molecular weight by 2d analytical ultracentrifugation. *Nature Communications*, 2:335, 2011.
- [94] C.-Y. Shih, C. Wu, M.V. Shugaev, and L.V. Zhigilei. Atomistic modeling of nanoparticle generation in short pulse laser ablation of thin metal films in water. *J. Coll. Interf. Sci.*, 489:3–17, 2017.
- [95] M. Dell’Aglia, A. Santagata, G. Valenza, A. De Stradis, and A. De Giacomo. Study of the effect of water pressure on plasma and cavitation bubble induced by pulsed laser ablation in liquid of silver and missed variations of observable nanoparticle features. *ChemPhysChem*, 18:1165–1174, 2017.
- [96] I. Chakraborty and T. Pradeep. Atomically precise clusters of noble metals: Emerging link between atoms and nanoparticles. *Chemical Reviews*, 117:8208–8271, 2017.
- [97] T. Nishi, Y. Akimoto, N. Takahashi, K. Kitazumi, S. Kajiyama, and Y. Watanabe. Novel method for ag colloidal cluster formation by laser ablation at the air-liquid interface. *Jpn. J. Appl. Phys.*, 54:095002, 2015.
- [98] N. Lasemi, U. Pacher, L.V. Zhigilei, O. Bomatiñ-Miguel, R. Lahoz, and W. Kautek. Pulsed laser ablation and incubation of nickel, iron and tungsten in liquids and air. *Applied Surface Science*, 433:772–779, 2018.
- [99] A.G. Berger, S.M. Restaino, and I.M. White. Vertical-flow paper sers system for therapeutic drug monitoring of flucytosine in serum. *Anal Chim Acta*, 1 (949):59–66, 2017.

- [100] C. Zanchi, A. Lucotti, M. Tommasini, S. Trusso, U. de Grazia, E. Ciusani, and P.M. Ossi. Laser tailored nanoparticle arrays to detect molecules at dilute concentration. *Applied Surface Science*, 396:1866–1874, 2017.
- [101] T.K. Sau, A.L. Rogach, F. Jäckel, T.A. Klar, and J. Feldmann. Properties and application of colloidal nonspherical noble metal nanoparticles. *Adv. Mater.*, 22:1805–1825, 2010.
- [102] J.E. Moore, S.M. Morton, and L. Jensen. Importance of correctly describing charge-transfer excitations for understanding the chemical effect in sers. *J. Phys. Chem. Lett.*, 3:2470, 2012.
- [103] S. Petersen and S. Barcikowski. Conjugation efficiency of laser-based bioconjugation of gold nanoparticles with nucleic acids. *J. Phys. Chem. C*, 113:19830, 2009.
- [104] L. Gamrad, C. Rehbock, J. Krawinkel, B. Tumursukh, A. Heisterkamp, and S. Barcikowski. Charge balancing of model gold-nanoparticle-peptide conjugates controlled by the peptide’s net charge and the ligand to nanoparticle ratio. *J. Phys. Chem. C*, 118:10302, 2014.
- [105] E. Fazio and F. Neri. Nonlinear optical effects from au nanoparticles prepared by laser plasma in water. *Applied Surface Science*, 272:88–93, 2013.
- [106] U. Kreibig and M. Vollmer. *Optical Properties of Metal Clusters*. Springer, Berlin, 1996.
- [107] G. Compagnini, E. Messina, O. Puglisi, R.S. Cataliotti, and V. Nicolosi. Spectroscopic evidence of core-shell structure in the earlier formation stages of au-ag nanoparticles by pulsed laser ablation in water. *Chem. Phys. Lett.*, 457:386, 2008.
- [108] A. Hamad, L. Li, and Z. Liu. A comparison of the characteristics of nanosecond, picosecond and femtosecond lasers generated ag, TiO<sub>2</sub> and au nanoparticles in deionised water. *Applied Physics A*, 120:1247–1260, 2015.

- [109] A. Ostendorf, G. Kamlage, U. Klug, F. Korte, and B.N. Chichkov. Femtosecond versus picosecond laser ablation. *Proceedings of SPIE*, 5713:1–8, 2005.
- [110] E. Fazio, M. Santoro, G. Lentini, D. Franco, S.P.P. Guglielmino, and F. Neri. Iron oxide nanoparticles prepared by laser ablation: Synthesis, structural properties and antimicrobial activity. *Colloids and Surfaces A: Physicochem. Eng. Aspects*, 490:98–103, 2016.
- [111] A. Semerok, C. Chaleard, V. Detalle, J.L. Lacour, P. Mauchien, P. Meynadier, C. Nouvellon, B. Salle, P. Palianov, M. Perdrix, and G. Petite. Experimental investigations of laser ablation efficiency of pure metals with femto, pico and nanosecond pulses. *Appl. Surf. Sci.*, 138:311, 1999.
- [112] F.A. Harraz, A.A. Ismail, H. Bouzid, S.A. Al-Sayari, A. Al-Hajry, and M.S. Al-Assiri. Surface-enhanced raman scattering (sers)-active substrates from silver plated-porous silicon for detection of crystal violet. *Appl. Surf. Sci.*, 331:241–247, 2015.
- [113] A. Schwenke, P. Wagener, S. Nolte, and S. Barcikowski. Influence of processing time on nanoparticle generation during picosecond-pulsed fundamental and second harmonic laser ablation of metals in tetrahydrofuran. *Applied Physics A*, 104:77–82, 2011.
- [114] C. Momma, B.N. Chichkov, S. Nolte, F. von Alvensleben, A. Tunnermann, H. Welling, and B. Welleghausen. Short-pulse laser ablation of solid targets. *Optics Communication*, 129:134–142, 1996.
- [115] K. Pathak and A. Povitisky. Plume dynamics and shielding characteristics of nanosecond scale multiple pulse in carbon ablation. *Journal of Applied Physics*, 104:113108, 2008.
- [116] K. Sneha, M. Sathishkumar, S. Kim, and Y.S. Yun. Counter ions and temperature incorporated tailoring of biogenic gold nanoparticles. *Process Biochemistry*, 45:1450–1458, 2010.
- [117] E. Tomaszewska, K. Soliwoda, K. Kadziola, B. Tkacz-Szczesna, G. Celi-chowski, M. Cichomski, W. Szmaja, and J. Grobelny. Detection limits of

- dls and uv-vis spectroscopy in characterization of polydisperse nanoparticles colloids. *Journal of Nanomaterials*, 313081, 2013.
- [118] D.M. Solís, J.M. Taboada, F. Obelleiro, L.M. Liz-Marzán, and F. Javier García de Abajo. Optimization of nanoparticle-based sensors substrates through large-scale realistic simulations. *ACS Photonics*, 4 (2):329–337, 2017.
- [119] J.M. Sanz, D. Ortiz, R. Alcaraz de la Osa, J.M. Saiz, F. González, A.S. Brown, M. Losurdo, H.O. Everitt, and F. Moreno. Uv plasmonic behavior of various metal nanoparticles in the near- and far-field regimes: Geometry and substrate effects. *J. Phys. Chem. C.*, 117:19606–19615, 2013.
- [120] C.J. DeSantis, M.J. McClain, and N.J. Halas. Walking the walk: A giant step toward sustainable plasmonics. *ACS Nano*, 10:9772–9775, 2016.
- [121] Y. Gutierrez, D. Ortiz, J.M. Sanz, J.M. Saiz, F. Gonzalez, H.O. Everitt, and F. Moreno. How an oxide shell affects the ultraviolet plasmonic behavior of ga, mg, and al nanostructures. *Opt. Express.*, 24:20621, 2016.
- [122] F. Sterl, N. Strohfeldt, R. Walter, R. Griessen, A. Tittl, and H. Giessen. Magnesium as novel material for active plasmonics in the visible wavelength range. *Nano Lett.*, 15:7949–7955, 2015.
- [123] M.W. Knight, T. Coenen, Y. Yang, B.J.M. Brenny, M. Losurdo, A.S. Brown, H.O. Everitt, and A. Polman. Gallium plasmonics: Deep subwavelength spectroscopic imaging of single and interacting gallium nanoparticles. *ACS Nano*, 9:2049–2060, 2015.
- [124] V. Fournier, P. Marcus, and I. Olefjord. Oxidation of magnesium. *Surf. Interface Anal.*, 34:494–497, 2002.
- [125] A.M. Watson, X. Zhang, R. Alcaraz de la Osa, J. Marcos Sanz, F. González, F. Moreno, G. Finkelstein, J. Liu, and H.O. Everitt. Rhodium nanoparticles for ultraviolet plasmonics. *Nano Lett.*, 15:1095–1100, 2015.



- [126] X. Zhang, P. Li, Á. Barreda, Y. Gutiérrez, F. González, F. Moreno, H.O. Everitt, and J. Liu. Size-tunable rhodium nanostructures for wavelength-tunable ultraviolet plasmonics. *Nanoscale Horiz.*, 1:75–80, 2016.
- [127] N. Zettsu, J. M. McLellan, B. Wiley, Y. Yin, Z.Y. Li, and Y. Xia. Synthesis, stability, and surface plasmonic properties of rhodium multipods, and their use as substrates for surface-enhanced raman scattering. *Angew. Chem., Int. Ed.*, 45:1288–1292, 2006.
- [128] S.D. Cramer and B.S. Jr. Covino. *ASM Handbook Volume 13B, Corrosion: Materials*. ASM International, 2005.
- [129] Y. Borodko, H. Sook Lee, S.H. Joo, Y. Zhang, and G. Somorjai. Spectroscopic study of the thermal degradation of pvp-capped rh and pt nanoparticles in  $h_2$  and  $o_2$  environments. *J Phys Chem C*, 114 (2):1117–1126, 2010.
- [130] Y. Abe, K. Kato, M. Kawamura, and K. Sasaki. Rhodium and rhodium oxide thin films characterized by xps. *Surf. Sci. Spectra*, 8:117–125, 2001.
- [131] S. Music, A. Saric, S. Popovic, and M. Ivanda. Formation and characterisation of nanosize  $\alpha - rh_2O_3$  particles. *J. Mol. Struct*, 924-926:224–224, 2009.
- [132] W.H. Weber, R.J. Baird, and G.W. Graham. Raman investigation of palladium oxide, rhodium sesquioxide and palladium rhodium dioxide. *Journal of Raman Spectroscopy*, 19 (4):239–244, 1988.
- [133] C.T. Williams, C.G. Takoudis, and M.J. Weaver. Ethanol oxidation on rhodium as probed by surface-enhanced raman and mass spectroscopies: Adsorbate stability, reactivity and catalytic relevance. *J Phys Chem B*, 102 (2):406–416, 1998.
- [134] K. Kato, T. Abe, M. Kawamura, and M. Sasaki. Preparation of  $RhO_2$  thin films by reactive sputtering and their characterizations. *Jpn. J. Appl. Phys*, 40:2399–2402, 2001.
- [135] P. Hildebrandt and M. Stockburger. Surface-enhanced resonance raman spectroscopy of rhodamine 6g adsorbed on colloidal silver. *J. Phys. Chem.*, 88 (24):5935–5944, 1984.

- [136] Y-I.L. Jeong, D.H. Kim, C.W. Chung, J-J Yoo, K.H. Choi, C.H. Kim, S.H. Ha, and D.H. Kang. Doxorubicin-incorporated polymeric micelles composed of dextran-b-poly (dl-lactide-coglycolide) copolymer. *Int. J. Nanomed.*, 6:1415–1427, 2011.
- [137] M.E. Khosroshahi, L. Ghazanfari, and Z. Hassannejad. Effect of laser wavelengths on drug release with and without gold nanoshells and magnetic guidance on uptake by cancer cells. *J. of Nanomedicine Research*, 6 (2):1–10, 2017.
- [138] M. Amoli-Diva, R. Sadighi-Bonabi, and K. Pourghazi. Switchable on/off drug release from gold nanoparticles-grafted dual light- and temperature-responsive hydrogel for controlled drug delivery. *Mater Sci Eng C Mater Biol Appl.*, 76:242–248, 2017.
- [139] H. Tang, L. Yao, J. Yang, W. Li, Z. Teng, and C. Xu. Near-infrared-light-induced fast drug release platform: Mesoporous silica-coated gold nanoframes for thermochemotherapy. *Part Part Syst Charact.*, 33:316–322, 2016.
- [140] G.S. Kwon, M. Yokoyama, T. Okano, Y. Sakurai, and K. Kataoka. Biodistribution of micelle-forming polymer-drug conjugates. *Pharm. Res.*, 10:970, 1993.
- [141] R.Z. Xiao, Z.W. Zeng, G. Lin Zhou, J.J. Wang, F. Zhu Li, and A. Ming Wang. Recent advances in peg-pla block copolymer nanoparticles. *Int. J. Nanomed.*, 5:1057–1065, 2010.
- [142] F. Zheng, S. Wang, M. Shen, M. Zhu, and X. Shi. Antitumor efficacy of doxorubicin-loaded electrospun nanohydroxyapatite-poly(lactic-co-glycolic acid) composite nanofibers. *Polym. Chem.*, 4 (4):933, 2013.
- [143] Z.M. Huang, Y.Z. Zhang, M. Kotaki, and S. Ramakrishna. A review on polymer nanofibers by electrospinning and their applications in nanocomposites. *Compos. Sci. Technol.*, 63 (15):2223, 2013.
- [144] E. Fazio, A. Scala, S. Grimato, A. Ridolfo, G. Grassi, and F. Neri. Laser light triggered smart release of silibinin from a pegylated-plga gold nanocomposite. *J. Mater. Chem. B*, 3:9023–9032, 2015.

- [145] R.S. Leena, M. Vairamani, and N. Selvamurugan. Alginate/gelatin scaffolds incorporated with silibinin-loaded chitosan nanoparticles for bone formation in vitro. *Colloids and Surfaces B: Biointerfaces*, 158:308–318, 2017.
- [146] M. Vinod and K.G. Gopchandran. Au, ag and au:ag colloidal nanoparticles synthesized by pulsed laser ablation as sers substrates. *Prog. Nat. Sci. Mater. Int.*, 24:569–578, 2014.
- [147] T.E. Itina. On nanoparticle formation by laser ablation in liquids. *J. Phys. Chem. C*, 115 (12):5044–5048, 2011.
- [148] K.C. Lee and S.J. Lin. Size effect of ag nanoparticles on surface plasmon resonance. *Surface Coating technology*, 202:5339–5342, 2008.
- [149] A.M. Manjón, P. Wagener, and S. Barcikowski. Transfer-matrix method for efficient ablation by pulsed laser ablation and nanoparticle generation in liquids. *J. Phys. Chem. C*, 115:5108–5114, 2011.
- [150] R. Singh and R.K. Soni. Laser synthesis of aluminium nanoparticles in biocompatible polymer solutions. *Applied Physics A*, 116:689–701, 2014.
- [151] F. Neri, A. Scala, S. Grimato, M. Santoro, S. Spadaro, F. Barreca, F. Cimino, A. Speciale, A. Saija, G. Grassi, and E. Fazio. Biocompatible silver nanoparticles embedded in a peg-pla polymeric matrix for stimulated laser light drug release. *J. Nanopart. Res.*, 18(6):153, 2016.
- [152] R.H. Prabhu, V.B. Patravale, and M.D. Joshi. Polymeric nanoparticles for targeted treatment in oncology: current insights. *Int. J. Nanomed.*, 10:1, 2015.
- [153] D.H. Kim, M.D. Kim, C.W. Choi, C.W. Chung, S.H. Ha, C.H. Kim, Y.H. Shim, Y.I. Jeong, and D.H. Kang. Antitumor activity of sorafenib-incorporated nanoparticles of dextran/poly(dl-lactide-coglycolide) block copolymer. *Nanoscale Research Letter*, 7:91, 2012.
- [154] S. Link and M.A. El-Sayed. Spectral properties and relaxation dynamics of surface plasmon electronic oscillations in gold and silver nanodots and nanorods. *J. Phys. Chem. B*, 103:8410–8426, 1999.

- [155] P. Raghavan, D.H. Lim, J.H. Ahn, C. Nah, D.C. Sherrington, H.S. Ryu, and H.J. Ahn. Electrospun polymer nanofibers: The booming cutting edge technology. *React. Funct. Polym*, 72 (12):915, 2012.
- [156] S.H. Shim and T.S. Duffy. Raman spectroscopy of Fe<sub>2</sub>O<sub>3</sub> to 62 gpa. *Am. Mineral.*, 87(2-3):318, 2002.
- [157] V. Rebuttni, E. Fazio, S. Santangelo, F. Neri, G. Caputo, C. Martin, T. Brousse, F. Favier, and N. Pinna. Chemical modification of graphene oxide through diazonium chemistry and its influence on the structure-property relationships of graphene oxide-iron oxide nanocomposites. *Chemistry*, 21(35):1, 2015.
- [158] H. Wang, H. Cheng, F. Wang, D. Wei, and X. Wang. An improved 3-(4,5-dimethylthiazol-2-yl)-2,5-diphenyl tetrazolium bromide (mtt) reduction assay for evaluating the viability of e. coli cells. *J. Microbiol. Methods*, 82:330–333, 2010.
- [159] J.A.S. Salman, M.F.H. Kadhemy, M. SamiJaleel, and A.K. Abdal. Effect of pva,pva/biosurfactant on some pathogenic bacteria in glass and plastic plates. *Int. J. Curr. Microbiol. Appl. Sci.*, 3 (10):301–309, 2014.
- [160] M. Valodkar, P.S. Rathore, R.N. Jadeja, M. Thounaojam, R.V. Deokar, and S. Thakore. Cytotoxicity evaluation and antimicrobial studies of starch capped watersoluble copper nanoparticles. *J. Hazard. Mater.*, 201-202:244–249, 2012.
- [161] C.S.S.R. Kumar and F. Mohammad. Magnetic nanomaterials for hyperthermia-based therapy and controlled drug delivery. *Adv. Drug Deliv. Rev.*, 63(9):789, 2011.
- [162] K. Choi, S. Hwang, Z. Dai, Y.C. Kang, and J. Lee. Rh-catalyzed WO<sub>3</sub> with anomalous humidity dependence of gas sensing characteristics. *RSC Adv.*, 4:53130–53136, 2014.
- [163] G. Neri. Metal oxide nanostructures for solid state gas sensors: A recent patent survey. *Recent Patents on Materials Science*, 4 (2):146–158, 2011.

- [164] B.H. Jang, O. Landau, S.J. Choi, J. Shin, A. Rothschild, and I.D. Kim. Selectivity enhancement of SnO<sub>2</sub> nanofiber gas sensors by functionalization with Pt nanocatalysts and manipulation of the operation temperature. *Sens. Actuators B Chem.*, 188:156–168, 2013.
- [165] I.S. Hwang, J.K. Choi, H.S. Woo, S.J. Kim, S.Y. Jung, and T.Y. Seong. Facile control of C<sub>2</sub>H<sub>5</sub>OH sensing characteristics by decorating discrete Ag nanoclusters on SnO<sub>2</sub> nanowire networks. *ACS Appl. Mater. Interfaces*, 3:3140–3145, 2011.
- [166] O.V. Safonova, G. Delabouglise, B. Chenevier, A.M. Gaskov, and M. Labeau. Co NO<sub>2</sub> gas sensitivity of nanocrystalline tin dioxide thin films doped with Pd, Ru and Rh. *Mater. Sci. Eng. C*, 21:105–111, 2002.
- [167] Y.J. Chiang, K.C. Li, Y.C. Lin, and F.M. Pan. A mechanistic study of hydrogen gas sensing by PdO nanoflake thin films at temperatures below 250°C. *Phys. Chem. Chem. Phys.*, 17:3039–3049, 2015.
- [168] Y.J. Chiang and F.M. Pan. PdO nanoflake thin films for CO gas sensing at low temperatures. *J. Phys. Chem. C*, 117 (30):15593–15601, 2013.
- [169] Y. Zheng, Q. Qiao, J. Wang, X. Li, and J. Jian. Gas sensing behavior of palladium oxide for carbon monoxide at low working temperature. *Sens. Actuators B*, 212:256–263, 2015.
- [170] P.K. Basu, S. Kallatt, E.A. Anumol, and N. Bhat. Suspended core-shell Pt-PtOx nanostructure for ultrasensitive hydrogen gas sensor. *J. Appl. Phys.*, 117:224501, 2015.
- [171] S.J. Kim, I.S. Hwang, C.W. Na, I.D. Kim, Y.C. Kang, and J.H. Lee. Ultrasensitive and selective C<sub>2</sub>H<sub>5</sub>OH sensors using Rh-loaded In<sub>2</sub>O<sub>3</sub> hollow spheres. *J. Mater. Chem.*, 21:18560, 2011.
- [172] N.H. Kim, S.J. Choi, S.J. Kim, H.J. Cho, J.S. Jang, W.T. Koo, M. Kim, and I.D. Kim. Highly sensitive and selective acetone sensing performance of WO<sub>3</sub> nanofibers functionalized by Rh<sub>2</sub>O<sub>3</sub> nanoparticles. *Sens. Actuators B*, 224:185–192, 2016.

- [173] T. Hubert, L. Boon Brett, G. Black, and U. Banach. Hydrogen sensors - a review. *Sens. Actuators B: Chem*, 157:329, 2011.
- [174] E. Lee, J.M. Lee, J.H. Koo, W. Lee, and T. Lee. Hysteresis behavior of electrical resistance in pd thin films during the process of absorption and desorption of hydrogen gas. *Int. J. Hydrogen Energy*, 35:6984, 2010.
- [175] F. Yang, D.K. Taggart, and R.M. Penner. Fast sensitive hydrogen gas detection using single palladium nanowires that resist fracture. *Nano Lett.*, 9:2177, 2009.
- [176] M. Khanuja, S. Kala, B.R. Mehta, and F.E. Kruis. Concentration-specific hydrogen sensing behavior in monosized pd nanoparticle layers. *Nanotechnology*, 20:015502, 2009.
- [177] K.J. Jeon, J.M. Lee, E. Lee, and W. Lee. Individual pd nanowire hydrogen sensor fabricated by electron-beam lithography. *Nanotechnology*, 20:135502, 2009.
- [178] S.M. McClure, M.J. Lundwall, and D.W. Goodman. Planar oxide supported rhodium nanoparticles as model catalysts. *PNAS*, 108 (3):931–936, 2011.
- [179] E. Fazio, S.G. Leonardi, M. Santoro, N. Donato, G. Neri, and F. Neri. Synthesis, characterization and hydrogen sensing properties of nanosized colloidal rhodium oxides prepared by pulsed laser ablation in water. *Sensors and Actuators B: Chemical*, 262:79–85, 2018.
- [180] S. Suhonen, M. Valden, M. Hietikko, R. Laitinen, A. Savimäki, and M. Härkönen. Effect of ce-zr mixed oxides on the chemical state of rh in alumina supported automotive exhaust catalysts studied by xps and xrd. *Catalysis A: General*, 218 (1-2):151–160, 2001.
- [181] L.S. Kibis, A.I. Stadnichenko, S.V. Koscheev, V.I. Zaikovskii, and A.I. Boronin. Xps study of nanostructured rhodium oxide film comprising rh<sub>4+</sub> species. *J. Phys. Chem. C*, 120 (34):19142–19150, 2016.
- [182] T. Christopher Williams, E.K.Y. Chen, C.G. Takoudis, and M.J. Weaver. Reduction kinetics of surface rhodium oxide by hydrogen and carbon

- monoxide at ambient gas pressure as probed by transient surface enhanced raman spectroscopy. *J. Phys. Chem. B*, 102:4785–4794, 1998.
- [183] N. Lavanya, C. Sekar, E. Fazio, F. Neri, S.G. Leonardi, and G. Neri. Development of aselective hydrogen leak sensor based on chemically doped SnO<sub>2</sub> for automotive applications. *Int. J. Hydrogen Energy*, 42:10645–10655, 2017.
- [184] I. Gaman Vasiliy, K. Maksimova Nadezda, V. Almaev Aleksey, and V. Sergeychenko Nadezda. Effect of humidity on characteristics of hydrogen sensors based onnanocrystalline SnO<sub>2</sub> thin films with various catalysts. *Key Eng. Mater.*, 683:353–357, 2016.
- [185] C. Wang, L. Yin, L. Zhang, D. Xiang, and R. Gao. Metal oxide gas sensors: sensitivityand influencing factors. *Sensors*, 10:2088–2106, 2010.
- [186] S. Jendrzzej, B. Gökce, M. Epple, and S. Barcikowski. How size determines the value of gold: Economic aspects of wet chemical and laser-based metal colloid synthesis. *ChemPhysChem*, 18:1012–1019, 2017.
- [187] T. Sakka, S. Iwanaga, Y.M. Ogata, A. Matsunawa, and T. Takemoto. Laser ablation at solidâĀŚliquid interfaces: an approach from optical emission spectra. *J. Chem. Phys.*, 112:8645–8653, 2000.
- [188] G. Lentini, E. Fazio, F. Calabrese, L.M. De Plano, M. Puliafico, D. Franco, M.S. Nicoló, S. Carnazza, S. Trusso, A. Allegra, F. Neri, C. Musolino, and S.P.P. Guglielmino. Phage-agnps complex as sers probe for u937 cell identification. *Biosensors and Bioelectronics*, 74:398, 2015.
- [189] F.D. Jochum and P. Theato. Temperature- and light-responsive smart polymer materials. *Chem. Soc. Rev.*, 42 (17):7468–7483, 2013.
- [190] K. Rahme, M.T. Nolan, T. Doody, G.P. McGlacken, M.A. Morris, C. O’Driscolle, and J.D. Holmes. Highly stable pegylated gold nanoparticles in water: applications in biology and catalysis. *RSC Adv.*, 3:21016, 2013.

- [191] K. Niikura, N. Iyo, Y. Matsuo, H. Mitomo, and K. Ijiro. Sub-100 nm gold nanoparticle vesicles as a drug delivery carrier enabling rapid drug release upon light irradiation. *ACS Appl. Mater. Interfaces*, 5:3900–3907, 2015.
- [192] J. Geng, K. Li, K.Y. Pu, D. Ding, and B. Liu. Conjugated polymer and gold nanoparticle co-loaded plga nanocomposites with eccentric internal nanostructure for dual-modal targeted cellular imaging. *Small*, 8:2421–2430, 2012.
- [193] L. Paasonen, T. Laaksonen, C. Johans, M. Yliperttula, K. Kontturi, and A. Urtti. Gold nanoparticles enable selective light-induced contents release from liposomes. *J. Controlled Release*, 122:86–93, 2007.
- [194] A.S. Angelatos, B. Radt, and F. Caruso. Light-responsive polyelectrolyte/gold nanoparticle microcapsules. *J. Phys. Chem. B*, 109:3071–3076, 2005.
- [195] G. Tan, L. Zhang, H. Ren, S. Wei, J. Huang, and A. Xia. Effects of ph on the hierarchical structures and photocatalytic performance of bivo4 powders prepared via the microwave hydrothermal method. *ACS Appl. Mater. Interfaces*, 5 (11):5186–5193, 2013.
- [196] J. Manson, D. Kumar, B.J. Meenan, and D. Dixon. Polyethylene glycol functionalized gold nanoparticles: the influence of capping density on stability in various media. *Gold Bull.*, 44:99, 2011.
- [197] S. Chen and K. Kimura. Synthesis and characterization of carboxylate-modified gold nanoparticle powders dispersible in water. *Langmuir*, 15:1075, 1999.
- [198] L. Lascialfari, P. Marsili, S. Caporali, M. Muniz-Miranda, G. Margheri, A. Serafini, A. Brandi, E. Giorgetti, and S. Cicchi. Carbon nanotubes/laser ablation gold nanoparticles composites. *Thin Solid Films*, 569:93, 2014.
- [199] W. Qian, M. Murakami, Y. Ichikawa, and Y. Che. Highly efficient and controllable pegylation of gold nanoparticles prepared by femtosecond laser ablation in water. *J. Phys. Chem. C*, 115:23293, 2011.



- [200] R. Gref, Y. Minamitake, M.T. Peracchia, V. Trubetsky, V. Torchilin, and R. Langer. Biodegradable long-circulating polymeric nanospheres. *Science*, 263:1600, 1994.
- [201] Q. Yao, Z.H. Lu, K. Yang, X. Chen, and M. Zhu. Ruthenium nanoparticles confined in sba-15 as highly efficient catalyst for hydrolytic dehydrogenation of ammonia borane and hydrazine borane. *Scientific Reports*, 5 (15186):1–11, 2015.
- [202] A. Gniewek and A.M. Trzeciak. Rh(0) nanoparticles: Synthesis, structure and catalytic application in suzuki-miyaura reaction and hydrogenation of benzene. *Top Catal*, 56 (13):1239–1245, 2013.
- [203] C.T. Williams, E. K-Y Chen, C.G. Takoudis, and M.J. Weaver. Reduction kinetics of surface rhodium oxide by hydrogen and carbon monoxide at ambient gas pressures as probed by transient surface-enhanced raman spectroscopy. *J Phys Chem B*, 63:4785–4794, 1998.
- [204] E. Fazio, A. Cacciola, A.M. Mezzasalma, G. Mondio, F. Neri, and R. Saija. Modelling of the optical absorption spectra. *J Quant Spectrosc Radiat Transfer*, 124:86–93, 2013.
- [205] S. Zafeiratos, V. Nehasil, and S. Ladas. X-ray photoelectron spectroscopy study of rhodium particle growth on different alumina surfaces. *Surf Sci*, 15:433–435, 1999.
- [206] M. Lau, I. Haxhiaj, P. Wagener, R. Intartaglia, F. Brandi, J. Nakamura, and S. Barcikowski. Ligandfree gold atom clusters adsorbed on graphene nano sheets generated by oxidative laser fragmentation in water. *Chemical Physics Letters*, 610-611:256–260, 2014.
- [207] Z.M. Xiu, Z.H. Jin, T.L. Li, S. Mahendra, G.V. Lowry, and P.J.J. Alvarez. Effects of nano-scale zero-valent iron particles on a mixed culture dechlorinating trichloroethylene. *Bioresour. Technol.*, 101:1141–1146, 2010.
- [208] S.A. Mahdy, Q.J. Raheed, and P.T. Kalaichelvan. Antimicrobial activity of zero-valent iron nanoparticles. *Int. J. Mod. Eng. Res.*, 2:578–581, 2012.

- [209] S.H. Shime and T.S. Duffy. Raman spettroscopy of  $\text{Fe}_2\text{O}_3$  to 62gpa. *Am. Miner.*, 87:318–326, 2001.
- [210] E. Fazio, F. Barreca, S. Spadaro, G. Curró, and F. Neri. Preparation of luminescentand optical limiting silicon nanostructures by nanosecond-pulsed laserablation in liquids. *Mater. Chem. Phys.*, 130:418–424, 2011.
- [211] S.H. Chen and M. Kotlarchyk. *Interaction of Photon and Neutron with Matter*. Singapore: World Scientific, 1998.



# Acknowledgement

During these three years of Ph.D many people gave contribute to my professional and personal development, and I would like to express my sincere gratitude to each one, even if it is not possible to write down here a complete list of them.

Firstly my gratitude goes to Prof. Enza Fazio and Prof. Fortunato Neri, for being a continuous source of inspiration and for their scientific advices. A deeper thanks goes to Enza, for all the discussions we had and, above all, for her friendship. This thesis work would not have been possible without the unconditional support she provided to me. My thank go to Dr. Francesco Barreca and Dr. Salvatore Spadaro for their dedicated support, and for sharing with me their experience. I would like to thank the group from Milano, Prof. Paolo Ossi, Prof. Matteo Tommasini and Prof. Andrea Lucotti.

My gratitude goes to Prof. Stephan Barcikowski and to Prof. Bilal Gökce who gave me the great opportunity to spend five months in their laboratory in Essen. Thanks to their group team that have been a source of good advice and collaboration. My time in Essen was also made enjoyable thanks to many friends, and I am especially grateful to Alex Letzel and Friedrich Waag for the pleasure of their companionship and support.

I would like to thank my colleagues and friends Giovanni, Giuseppe and Valentino for the funny moments we had together.

Lastly, I would like to thank my family for all their love and encouragement. For my parents and my brothers, who raised me with a love of science and supported me in all my pursuits. And most of all for my loving, supportive, encouraging, and patient girlfriend Cristina whose faithful support is so appreciated. Thank you.

# Europass Curriculum Vitae



## Personal information

Surname(s) / First name(s)

Address(es)

Telephone(s)

Email(s)

Nationality(-ies)

Date of birth

Gender

## Santoro Marco

3, Via Belvedere, 98121, Messina, Italy

mobile: 00393408284072

Personal: [santoro.marco92@gmail.com](mailto:santoro.marco92@gmail.com)

Professional: [masantoro@unime.it](mailto:masantoro@unime.it)

Italian

11 January 1992

Male

## Work experience

May 2018 up to now

Device Engineer at [ST Microelectronic](#) in Catania

## Research Interest

I'm interested in exploring the field of laser processing of materials. Among this branch, my interest is focussed on Laser Melting (LML), Laser Ablation (LAL) and Laser Fragmentation in Liquid (LFL).

I'm working on the synthesis of micro- and nano-systems prepared by Pulsed Laser Ablation and on the Laser irradiation of educt particles in liquid environment in order to enable chemical conversion and modification of particle sizes. Then is important the study of their optical, chemical and morphological properties in order to use laser synthesized particles for technological applications (biology, energetics, sensor devices, etc.).

## Education and training

2015 up to (expected) 2018

[University of Messina](#), Italy

PhD, Physics

2013 up to 2015

[University of Messina](#), Italy

M.Sc., Physics

- 110/110 cum laude (maximum grade in Italy)
- Thesis Title: *Nanodispositivi polimerici funzionalizzati con nanoparticelle a base metallica prodotte per ablazione laser*

*Polymeric nanodevices functionalized with metal based nanoparticles made by laser ablation*

This work is focused on the synthesis of metal based nanoparticles by laser ablation. Picosecond pulsed laser deposition in liquids (PLAL) technique is used to produce silver and iron oxide nanocolloids, by ablating metallic targets in different environments. The nanocolloids characterization has been carried out in the laboratory of the physics department of Messina using some spectroscopic techniques (UV-vis and IR optical absorption, dynamic light scattering, micro-Raman spectroscopy, X-ray photoelectron spectroscopy) and scanning electron microscopy (SEM/EDX and STEM). Solid state devices (like gas sensor) are obtained by spin coating, electrospinning or air spraying the nanocolloids compounds onto appropriate substrates.

In the case of sensing devices, electrical conductivity measurements have been carried out to verify the sensor efficiency towards gaseous ethanol exposition.

In order to check for potential biomedical applications, some of the nanocomposite systems have been tested to verify their degree of biocompatibility and cytotoxicity. Finally, a nanodevice for setting up a drug delivery system has been tested by inserting drugs into appropriately shaped nanocomposites. The release tests show an enhancement of the rate of drug release when light absorption, due to plasmonic effects, takes place and increase the thermally activated release process, due to the presence of silver metal nanoparticles.

Advisor: [Professor Fortunato Neri](#)

2010 up to 2013

**University of Messina**, Italy

B.Sc., Physics

- 110/110 cum laude (maximum grade in Italy)
- Thesis Title: *Deposizione di materiali nanostrutturati mediante laser impulsati e di potenza*

*Pulsed power laser deposition of nanostructured materials.*

Advisor: [Professor Fortunato Neri](#)

2005 to 2010

**Liceo Scientifico Statale "Archimede"**, Messina, Italy

High School Diploma in Maths and Science

Mark: 95/100

## Relevant Experience

**University of Duisburg-Essen**, Germany

From 1<sup>st</sup> March to 31<sup>st</sup> July 2017

Visiting scientist in the group of [Prof. Stephan Barcikowski](#), in the section of Laser Technology and Nanocomposite directed by [Dr. Bilal Goekce](#)

Local organizing committee of **PPLA2017**

From 5<sup>th</sup> to 7<sup>th</sup> July 2017

Organization of **Workshop on: Nanoparticles Engineering by Pulsed Laser Ablation: Concepts and Applications**

16<sup>th</sup> July 2018

**SLIMS 2014, School on Laser in Material Science**

July 13-20 2014, Venice, Italy

I've been part of OSA students chapter and the EPS Young Mind group of Messina since 2013 and with them I contribute to organize some local seminars: [Water](#) and [Ottava Giornata con la Fisica Teorica a Messina](#) in 2014, [Dieci anni con Appunti di Fisica](#) in 2015, [Nanofabrication](#) and [Nona Giornata con la Fisica Teorica a Messina](#) in 2016.

## Personal skills and competences

Mother tongue(s)

Other language(s)

Social skills and competences

Computer skills and competences

### Italian

### English

**French** : Beginner

**German** : Beginner

Good team-work attitudes

Strongly motivated student and an hard worker

### Computer Programming:

- Good knowledge: Fortran
- Discrete knowledge : C, C++ (basic knowledge)

### Relevant Software:

- $\LaTeX$ , Mathematica, Matlab, Origin, Octave, Gnuplot, Microsoft Office, Adobe Package (Photoshop, Illustrator), ImageJ and Image Pro Plus (for STEM image analysis), Wien2k (for ab initio simulation)

### Operating Systems:

- Microsoft Windows, Linux (Mint, Ubuntu)

## Relevant skills and competences

- Good knowledge about electronic devices (Diodes and MOSFET) and on their fabrication processes
- Good knowledge in materials characterization technique (optical, morphological and chemical)

## Publications

### **How a re-irradiated ablation target affects cavitation bubble dynamics and nanoparticles properties in laser ablation in liquids**

A. Letzel, M. Santoro, J. Frohleiks, A.R. Ziefuß, S. Reich, A. Plech, E. Fazio, F. Neri, S. Barcikowski, B. Gökce

*Submitted on Applied Surface Science*

August 2018

### **SERS Sensing of Perampanel with Nanostructured Arrays of Gold Particles Produced by Pulsed Laser Ablation in Water**

M. Santoro, E. Fazio, S. Trusso, M. Tommasini, A. Lucotti, R. Saija, M. Casazza, F. Neri, P.M. Ossi

*Accepted by Medical Devices and Sensors*

### **Chapter 12: Laser Synthesized Nanoparticles for Therapeutic Drug Monitoring**

M. Tommasini, C. Zanchi, A. Lucotti, E. Fazio, M. Santoro, S. Spadaro, F. Neri, S. Trusso, E. Ciusani, U. de Grazia, M. Casazza, P.M. Ossi

Advances in the Application of Lasers in Materials Science, 2018, Springer Nature Switzerland AG

### **Synthesis, characterization and hydrogen sensing properties of nanosized colloidal rhodium oxides prepared by Pulsed Laser Ablation in water**

E. Fazio, S. G. Leonardi, M. Santoro, N. Donato, G. Neri, F. Neri

*Sensors and Actuators B: Chemical, (2018), 262, 79-85*

### **Synthesis by picosecond laser ablation of ligand-free Ag and Au nanoparticles for SERS applications**

E. Fazio, S. Spadaro, M. Santoro, S. Trusso, A. Lucotti, M. Tommasini, F. Neri, P.M. Ossi

*EPJ Web of Conferences, (2018), 167, 05002*

### **PEG-PLGA electrospun nanofibrous membranes loaded with Au@Fe<sub>2</sub>O<sub>3</sub> nanoparticles for drug delivery applications**

S. Spadaro, M. Santoro, F. Barreca, A. Scala, S. Grinato, F. Neri, E. Fazio

*Frontiers of Physics, (2018), 13, 136201*

### **Biocompatible silver nanoparticles embedded in a PEG-PLA polymeric matrix for stimulated laser light drug release**

F. Neri, A. Scala, S. Grinato, M. Santoro, S. Spadaro, F. Barreca, F. Cimino, A. Speciale, A. Saija, G. Grassi and E. Fazio

*J. Nanopart. Res. (2016), 18:153*



## Conferences and Posters

### **Iron oxide nanoparticles prepared by laser ablation: Synthesis, structural properties and antimicrobial activity**

E. Fazio, M. Santoro, G. Lentini, D. Franco, S. P. P. Guglielmino and F. Neri

*Colloids and Surfaces A: Physicochemical and Engineering Aspects*, (2016), 490, 98-103

### – **SERS Activity of Nanostructured Rhodium Oxide Thin Films Deposited by Pulsed Laser Deposition.**

M. Santoro, A. Bertoncini, E. Fazio, M. Tommasini, F. Neri, P.M. Ossi, S. Trusso

**CNS2018** 4<sup>o</sup> *National Sensor Conference*

21-23 February 2018

### – **Elemental and alloyed noble metal particles by picosecond and nanosecond ablation in water. Nanostructure, optical and spectroscopic properties.**

E. Fazio, S. Spadaro, M. Santoro, S. Trusso, F. Neri, A. Lucotti, M. Tommasini, P.M. Ossi

**COLA2017** *International Conference on Laser Ablation*

3-8 September 2017

### – **Surface nanostructuring, optical and SERS properties of Ag and Au particles prepared by nanosecond and picosecond ablation in water.**

P.M. Ossi, M. Santoro, E. Fazio, S. Trusso, A. Lucotti, M. Tommasini, C. Zanchi, R. Saija, F. Neri

**PPLA2017** *Plasma Physics by Laser and Applications*

5-7 July 2017

### – **Sensing properties of rhodium oxide nanoparticles prepared by pulsed laser ablation in liquids.**

E. Fazio, M. Santoro, F. Neri, S.G. Leonardi, G. Neri

**Materials2016** *Conference on Materials Science and Technology*

12-16 December 2016

### – **Rhodium oxide nanoparticles synthesis by pulsed laser ablation in liquid**

M. Santoro, E. Fazio, P. M. Ossi, S. Trusso, M. Tommasini, A. Lucotti, F. Neri

**GISR2016** *Italian Meeting on Raman Spectroscopies and Non Linear Optical Effects*

14-16 September 2016

– **Nanostructure and optical properties of noble metal particles prepared by nanosecond and picosecond laser ablation**

P.M. Ossi, M. Santoro, E. Fazio, S. Trusso, P. Calandra, M. Tommasini, C. Zanchi, R. Saija and F. Neri

**ICPEPA-10** *10th International Conference on Photoexcited Processes and Applications*

29 August-2 September 2016

– **New remotely-triggered drug delivery system based on a PEG-PLA Ag nanocomposites**

M. Santoro, A. Scala, S. Grimato, F. Barreca, S. Spadaro, G. Grassi, F. Neri and E. Fazio

**IONS** *The International OSA Network of Students*

6-8 July 2016

## References

### **Professor Fortunato Neri** ([fneri@unime.it](mailto:fneri@unime.it))

- Full Professor, Department of Mathematics and Computational Science, Physics Science and Earth Science  
University of Messina
- △ Dipartimento di Matematica, Informatica, Scienze Fisiche e Scienze della Terra,  
Viale Ferdinando Stagno D'Alcontres 31, 98166 Messina (Italy)

### **Professor Paolo Maria Ossi** ([paolo.ossi@polimi.it](mailto:paolo.ossi@polimi.it))

- Associate Professor, Department of Energy & NEMAS  
Polytecnic of Milan
- △ Dipartimento di Energia & NEMAS, Via Ponzio 34/3 20133 Milano (Italy)

### **Professor Enza Fazio** ([enfazio@unime.it](mailto:enfazio@unime.it))

- Associate Professor, Department of Mathematics and Computational Science, Physics Science and Earth Science  
University of Messina
- △ Dipartimento di Matematica, Informatica, Scienze Fisiche e Scienze della Terra,  
Viale Ferdinando Stagno D'Alcontres 31, 98166 Messina (Italy)

## About me

Hobbies

Technology, singing, skywatching, reading, cooking and football